Report of Investigations 2017-9

TSUNAMI INUNDATION MAPS FOR JUNEAU, ALASKA

D.J. Nicolsky, E.N. Suleimani, R.D. Koehler, and J.B. Salisbury

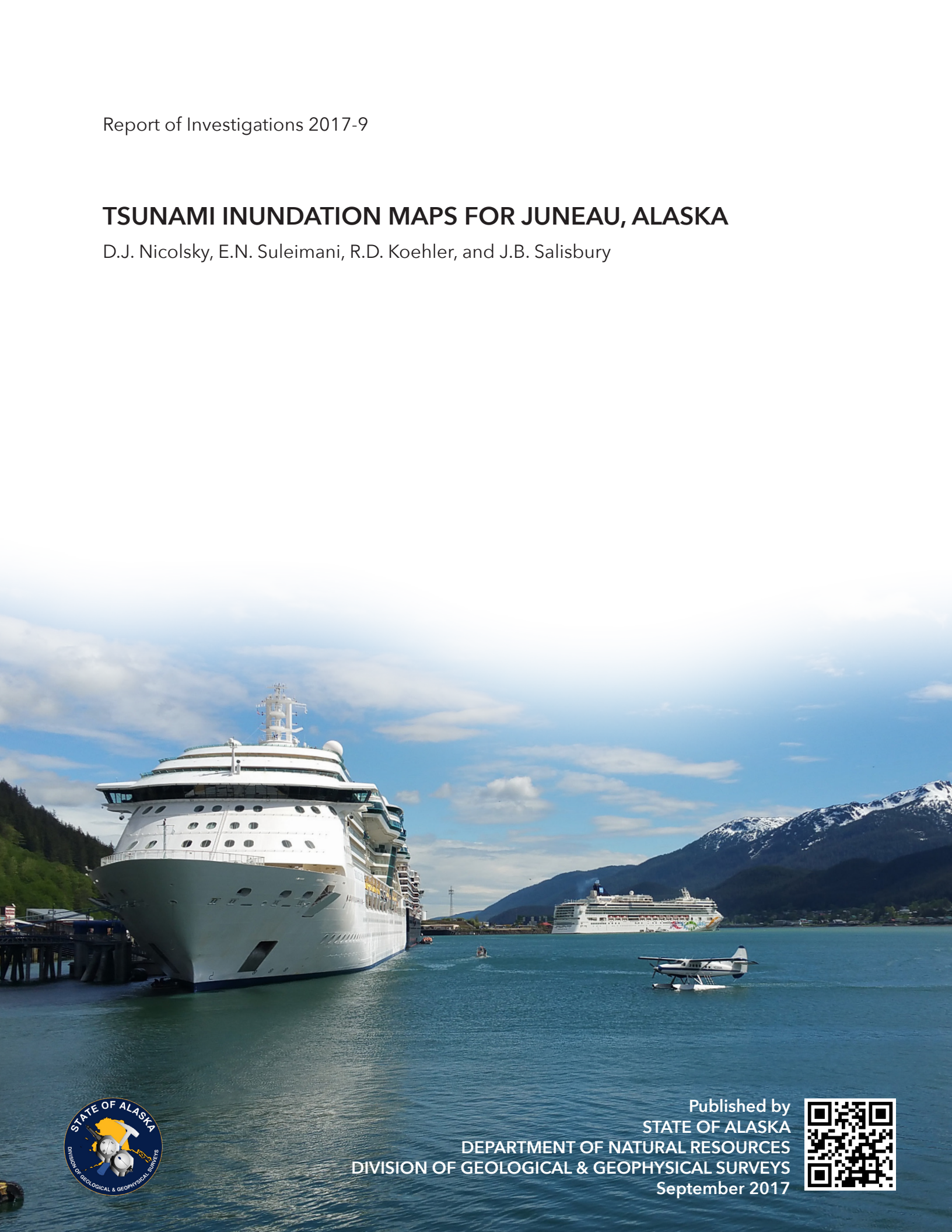

Published by
STATE OF ALASKA
DEPARTMENT OF NATURAL RESOURCES
DIVISION OF GEOLOGICAL & GEOPHYSICAL SURVEYS
September 2017

Cover. Cruise ships in Juneau Harbor.

TSUNAMI INUNDATION MAPS FOR JUNEAU, ALASKA

D.J. Nicolsky, E.N. Suleimani, R.D. Koehler, and J.B. Salisbury

Report of Investigations 2017-9

State of Alaska
Department of Natural Resources
Division of Geological & Geophysical Surveys

STATE OF ALASKA
Bill Walker, Governor

DEPARTMENT OF NATURAL RESOURCES
Andrew T. Mack, Commissioner

DIVISION OF GEOLOGICAL & GEOPHYSICAL SURVEYS
Steve Masterman, State Geologist and Director

Publications produced by the Division of Geological & Geophysical Surveys (DGGS) are available for free download from the DGGS website (dggs.alaska.gov). Publications on hard-copy or digital media can be examined or purchased in the Fairbanks office:

Alaska Division of Geological & Geophysical Surveys
3354 College Rd., Fairbanks, Alaska 99709-3707
Phone: (907) 451-5010 Fax (907) 451-5050
dggspubs@alaska.gov | dggs.alaska.gov

DGGS publications are also available at:
Alaska State Library,
Historical Collections & Talking Book Center
395 Whittier Street
Juneau, Alaska 99811

Alaska Resource Library and Information Services (ARLIS)
3150 C Street, Suite 100
Anchorage, Alaska 99503

Suggested citation:
Nicolsky, D.J., Suleimani, E.N., Koehler, R.D., and Salisbury, J.B., 2017, Tsunami inundation maps for Juneau, Alaska: Alaska Division of Geological & Geophysical Surveys Report of Investigation 2017-9, 66 p., 5 sheets.
http://doi.org/10.14509/29741

Contents

Figures

Tables

Appendix

Map Sheets

Sheet 1. Maximum estimated tsunami inundation, Juneau, Alaska

Sheet 2. Maximum estimated tsunami inundation, Juneau, Alaska: Echo Cove, Bridget Cove, and Eagle Creek delta

Sheet 3. Maximum estimated tsunami inundation, Juneau, Alaska: Lena Cove, Tee Harbor, and Pearl Harbor

Sheet 4. Maximum estimated tsunami inundation, Juneau, Alaska: Juneau Airport area

Sheet 5. Maximum estimated tsunami inundation, Juneau, Alaska: Gastineau Channel

TSUNAMI INUNDATION MAPS FOR JUNEAU, ALASKA

D.J. Nicolsky[1], E.N. Suleimani[1], R.D. Koehler[2], and J.B. Salisbury[2]

Abstract

In this report we evaluate potential tsunami hazards for the southeastern Alaska community of Juneau and numerically model the extent of inundation from tsunami waves generated by tectonic and submarine landslide sources. We calibrate our tsunami model by numerically simulating the 2011 Tohoku tsunami at Juneau and comparing our results to instrument records. Analysis of calculated and observed water level dynamics for the 2011 event in Juneau reveals that the model underestimates the observed wave heights in the city by a factor of two, likely due to complex tsunami-tide interactions. We compensate for this numerical underestimation by doubling the coseismic slip of the hypothetical tsunami sources in our models. Potential hypothetical maximum credible tsunami sources include variations of the extended 1964 rupture and megathrust earthquakes in the Prince William Sound and Alaska Peninsula regions. Local underwater landslide events in Lynn Canal, in Favorite, Saginaw, and Gastineau channels, and in Taku Inlet are also considered as possible tsunamigenic scenarios. The results show that the maximum predicted wave height in the Juneau area resulting from a tectonic tsunami is 2–3 m (6–10 ft), while a landslide-generated tsunami may cause a run-up of 15–16 m (49–52 ft) along the Fritz Cove shoreline and potentially flood portions of the airport. Results presented here are intended to provide guidance to local emergency management agencies in tsunami inundation assessment, evacuation planning, and public education to mitigate future tsunami hazards.

INTRODUCTION

Subduction of the Pacific plate under the North American plate has resulted in numerous great earthquakes and is the source of locally-generated tsunamis in Alaska (Dunbar and Weaver, 2008). Several historical earthquakes along the Alaska–Aleutian subduction zone (fig. 1) have generated tsunamis resulting in widespread damage and loss of life in exposed coastal communities in Alaska and throughout the Pacific Ocean (Lander, 1996). However, tsunamis originating in the vicinity of the Aleutian Islands, Alaska Peninsula, and the Gulf of Alaska are of particular concern to Alaskans because, as local hazards, waves can reach coastal communities within minutes of the earthquake that caused them.

The vulnerability of Alaska's coast to tsunami waves was demonstrated by the March 27, 1964, Great Alaska earthquake. This M_w 9.2 megathrust earthquake (fig. 1) was the largest recorded earthquake in North America and generated the most destructive tsunami in Alaska history (Plafker and others, 1969; Kanamori, 1970; Johnson and others, 1996; Lander, 1996). In addition to the major tectonic tsunami triggered by ocean-floor displacement, multiple local tsunamis were generated by landslides. The landslide-generated tsunamis arrived almost immediately after shaking

[1]Alaska Earthquake Center, Geophysical Institute, University of Alaska, P.O. Box 757320, Fairbanks, Alaska 99775-7320; djnicolsky@alaska.edu

[2]Alaska Division of Geological & Geophysical Surveys, 3354 College Rd., Fairbanks, Alaska 99709-3707. R.D. Koehler now at Nevada Bureau of Mines and Geology, Mackay School of Earth Science and Engineering, University of Nevada, Reno, 1664 North Virginia Street, MS 178, Reno, NV 89557

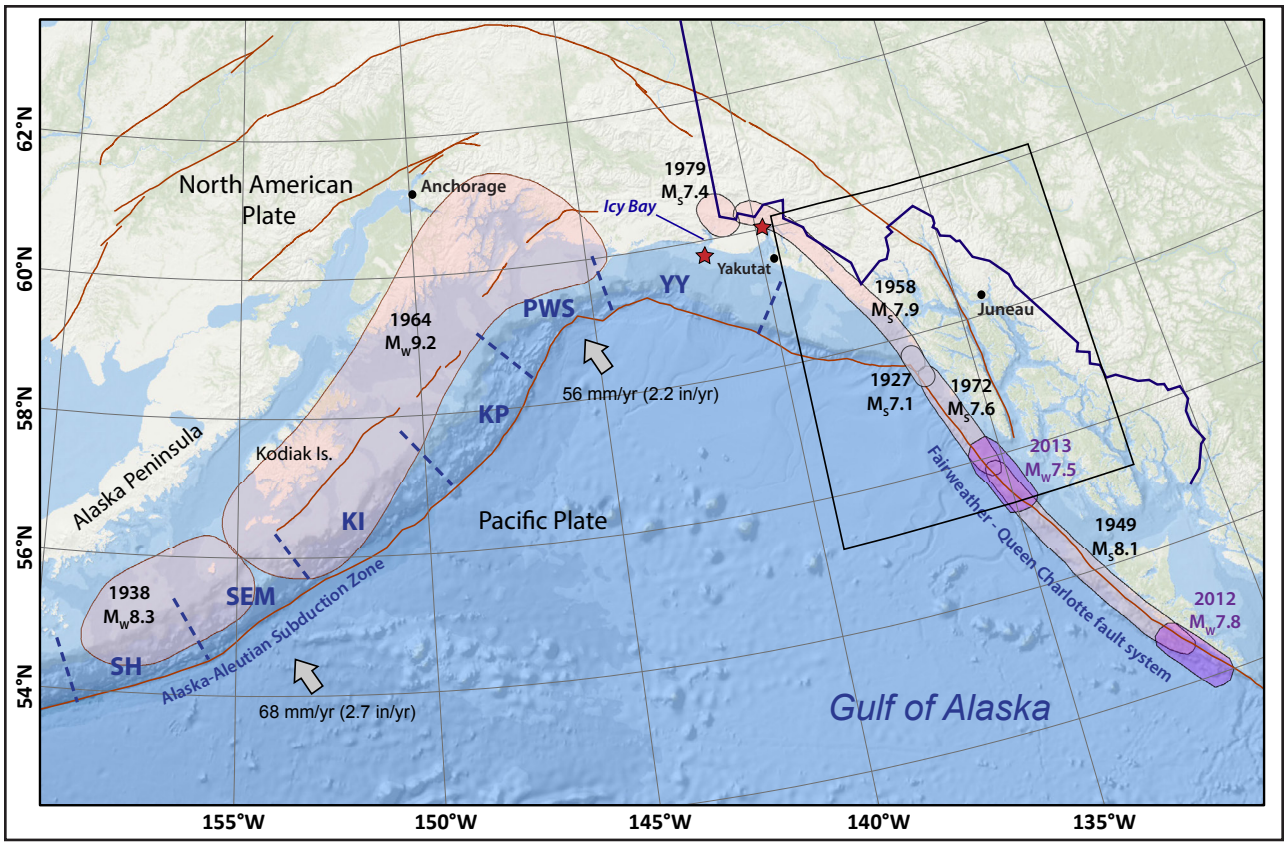

Figure 1. Map of south-central and southeastern Alaska, showing rupture areas of major historical earthquakes (light pink shading). Red stars mark epicenters of two September 1899 earthquakes. The segment notations of the Alaska-Aleutian megathrust are from Nishenko and Jacob (1990): Yakataga–Yakutat (YY), Prince William Sound (PWS), Kenai Peninsula (KP), Kodiak Island (KI), Semidi Islands (SEM), and Shumagin Islands (SH) segments. The area inside the black rectangle is shown in detail in figure 2A.

was felt, leaving virtually no time for warning or evacuation. Of the 131 fatalities associated with this earthquake, 122 were caused by the tectonic and landslide-generated tsunamis (Lander, 1996). The local tsunamis in the Gulf of Alaska region caused most of the damage and accounted for 76 percent of the aforementioned 122 tsunami deaths (Lander, 1996).

The 1964 tsunami did not uniformly impact the vast Alaska coastline. Waves did not cause significant damage to Juneau; the 1964 tsunami arrived approximately three hours after the earthquake on a rising tide and its estimated height was ~1.2 m (~3.9 ft) (Lander, 1996). Despite the relatively small size of the 1964 tsunami at Juneau, wave action persisted for at least 10 hours (Lander, 1996, figure 77). During future tsunamis, it is possible that the highest wave in the tsunami wave train could arrive during high tide and cause more damage than what occurred in 1964. Potential future earthquakes and tsunamis in the Gulf of Alaska and around the Pacific Ocean necessitate the development of inundation and tsunami evacuation maps for use in tsunami risk mitigation.

We approach this problem—modeling the outcome of different tsunami-generating scenarios—deterministically. This means we are not focused on calculating the relative likelihood and frequency of various magnitude earthquakes, as is done for land-use planning or insurance estimates (Geist and Parsons, 2006; Geist and Lynett, 2014). Because the known earthquake and tsunami history of Alaska is short, we instead model the results of many hypothetical earthquakes and landslides to explore potential "worst case scenarios," as determined by the geologic characteristics and earthquake history of the region. Producing a tsunami inundation map for a community there-

fore consists of several steps. First, we develop credible scenarios for maximum plausible tsunamigenic earthquakes based on historic records and known fault segmentation. We then model tsunami dynamics resulting from each of the scenarios, without assigning probabilities to the earthquake occurrences. The results are then compared with historical tsunami observations if such data exist. Finally, we develop a "worst-case" inundation line that encompasses the maximum extent of flooding from all model simulations of all source scenarios and historical observations. The worst-case inundation line becomes a basis for local tsunami hazard planning.

The intended audience for this report consists of scientists, engineers, and planners interested in applying this approach to develop tsunami inundation and evacuation maps. Digital data and documentation provided with the report enable technical users to explore the range of tsunami inundation expected for future events.

PROJECT BACKGROUND: REGIONAL AND HISTORICAL CONTEXT

Setting

Juneau (58°18' N, 134°25' W) is the capital city of Alaska and had a population of 33,277 in 2016 (Alaska Department of Labor and Workforce Development, 2016). Juneau is on the mainland of southeastern Alaska east of Douglas Island (fig. 2A). It lies ~1,450 km (900 mi) northwest of Seattle and ~930 km (577 mi) southeast of Anchorage. Juneau is rather unusual among U.S. capitals in that there are no roads connecting the city to the rest of Alaska or to the rest of North America (although ferry service is available for cars). The absence of a road network is due to the extremely rugged terrain surrounding the city. All resources coming in and going out must be transported by plane or boat.

Earthquake and tsunami history

Juneau is in southeastern Alaska, where the primary tectonic elements of the Pacific–North American plate boundary are the Alaska–Aleutian subduction zone and the >1,000-km-long (>620-mi-long) Fairweather–Queen Charlotte (FW–QC) fault system (fig. 1). Plate motion is accommodated along the Fairweather fault, a transform fault that extends primarily offshore along the entire southeastern Alaska coastline, becoming the Queen Charlotte fault to the south in British Columbia (figs. 1 and 2A). The entire Fairweather–Queen Charlotte fault system ruptured in large strike-slip earthquakes over the last century: 1927 (M_s 7.1), 1949 (M_s 8.1), 1958 (M_s 7.9), and 1972 (M_s 7.6) (Sykes, 1971; Page, 1973; Tocher, 1960). See Suleimani and others (2013, figure 4) for additional rupture location details of these earthquakes and further information on the seismotectonics of the region. An analysis of the above-mentioned events indicates that seismic slip along the FW–QC fault system is parallel to the direction of motion between the North American and Pacific plates (Doser and Lomas, 2000). Recently, an unusual thrust event on the southern part of the FW–QC fault system—the 2012 Haida Gwaii earthquake—generated a large tsunami along the outer coast of British Columbia. The local run-up was observed to reach 7.5 m (25 ft) in some inlets in the rupture area. Although large-magnitude earthquakes can occur on the FW–QC fault system, the predominantly strike-slip mechanism of these earthquakes lacks large vertical perturbations to the seafloor and is therefore unlikely to generate tsunamis in Juneau.

Most of the hazard related to the strike-slip earthquakes, besides the strong ground shaking, is due to ground failures. The 1958 event triggered a large landslide into Lituya Bay (fig. 2B) that generated a 530 m-high (1,740 ft-high) wave (Miller, 1960). Other smaller landslides and ground failures during the 1958 event occurred in Disenchantment Bay, Dry Harbor, Haines/Skagway area, and near Wrangell (Lander, 1996). Underwater cables were broken by submarine landslides in Lynn Canal between Juneau and Skagway (figure 2B). No tsunami damage was reported for Juneau during the 1958 event.

Because Juneau is located in a network of

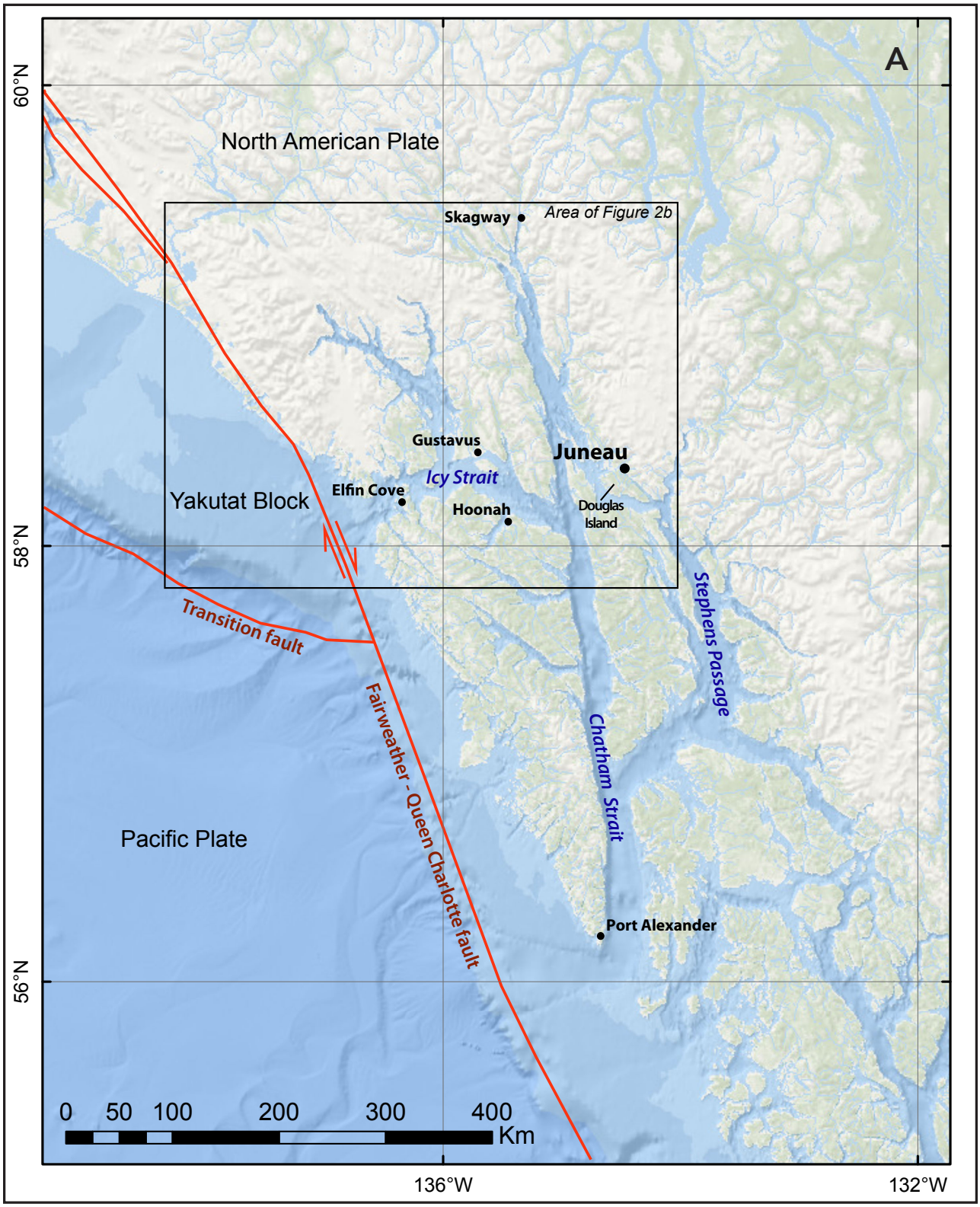

Figure 2. (A) Map of southeastern Alaska, showing the location of Juneau with respect to other communities. The area inside the black rectangle is shown in figure 2B.

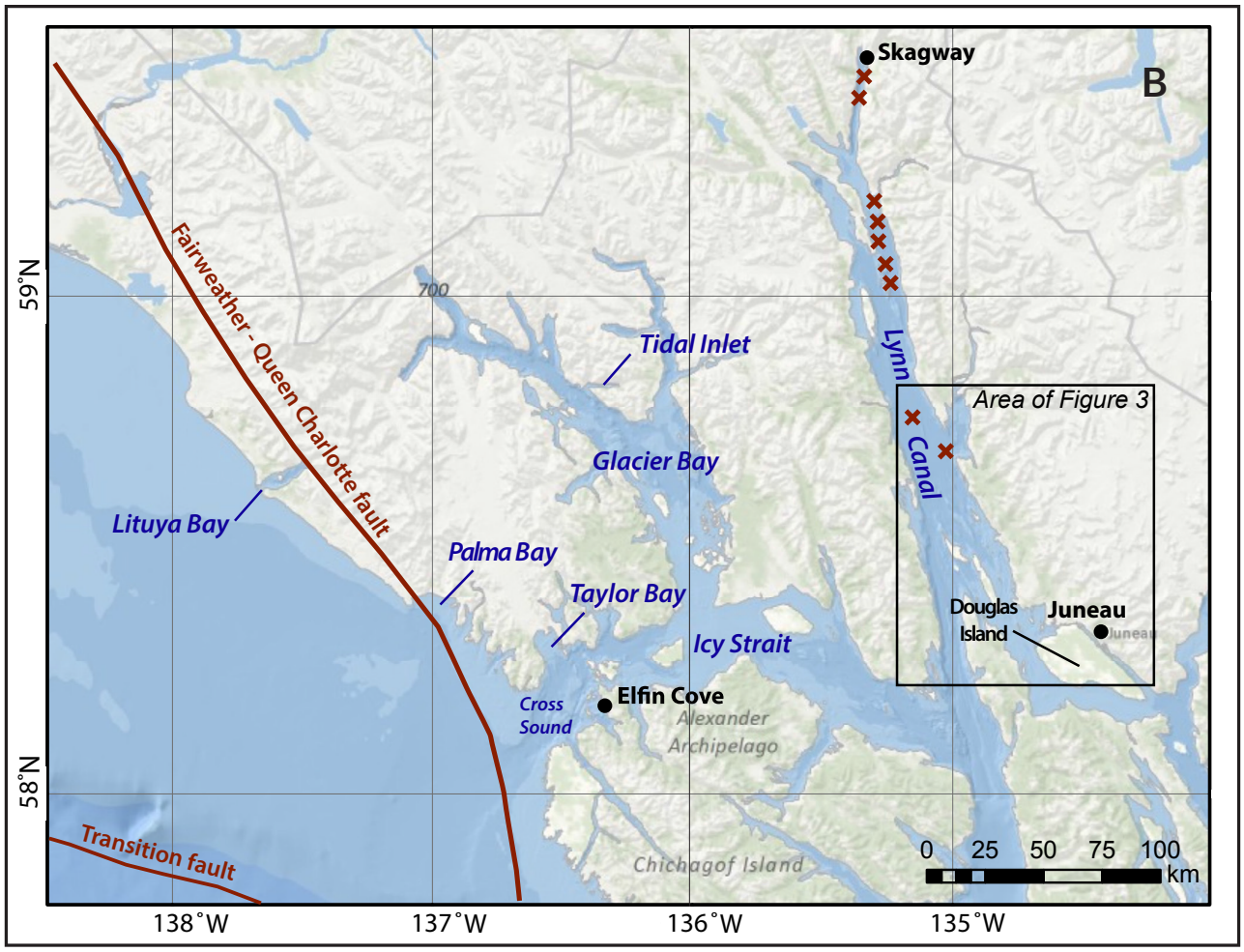

Figure 2, continued. (B) Detailed map of the areas adjacent to Icy Strait and Lynn Canal. Red crosses indicate locations of underwater cable breaks associated with the M_s 7.9 earthquake of June 9, 1958. The area inside the black rectangle is shown in detail in figure 3.

marine passages that weave through the islands of southeastern Alaska and British Columbia (fig. 2), it is commonly thought to be protected from tectonic waves coming from the Pacific Ocean (for example, Lander, 1996, p. 17). Only nine tsunamis are reported to have reached the town, and none have resulted in any damage or loss of life. Table 1 provides a summary of tsunami effects at Juneau caused by earthquakes of the last century, as summarized from Lander (1996) and recent trans-Pacific and local tsunami records extracted from the tsunami database of the National Centers for Environmental Information/World Data Centers (NCEI/WDS) (in progress). The largest observed tsunami in Juneau happened after the 1964 earthquake; however no significant damage was reported. Because future earthquakes in the area might have different patterns of energy release, relying solely on historical events may significantly underestimate potential inundation in the community.

Landslide tsunami hazard potential

Tsunamis caused by underwater slope failures constitute a significant hazard in the fjords of coastal Alaska and other high-latitude fjord coastlines (Lee and others, 2006). Kulikov and others (1998) analyzed tsunami catalog data for Southeast Alaska and British Columbia and showed that this region has a long record of tsunami waves generated by submarine and subaerial landslides, avalanches, and rockfalls. In the majority of cases tectonic tsunamis arriving in bays and fjords from

Table 1. Tsunami effects at Juneau; data from the National Geophysical Data Center Global Historical Tsunami Database (in progress) and comments from Lander (1996).

Date	Magnitude (M_w)	Origin	Maximum water height (m)	Comments
10/24/1927	7.1	Southeast Alaska	Observed	Heavy seas broke towline, water muddy and churned. The Juneau-Skagway-Haines cable broke in two places. Cable breaks were ascribed to a submarine slide.
11/4/1952	8.2	Kamchatka Peninsula	0.13	
3/9/1957	8.3	Central Aleutian Islands	0.20	
7/10/1958	7.9	Southeast Alaska	Observed	Six underwater cables broke.
5/22/1960	8.6	Chile	0.05	Trace recorded.
3/28/1964	8.5	Gulf of Alaska	1.10	The tide was 4 to 6 feet higher than normal.
07/30/1972	7.6	Southeast Alaska	0.10	Coast Guard reported "confused whitecap throughout Alaskan waters."
2/27/2010	8.5	Chile	0.11	
3/11/2011	8.3	Japan: Honshu	0.21	

the open ocean had wave heights smaller than those of local landslide-generated tsunamis. For example, the 1964 landslide-generated tsunami in Port Valdez devastated the waterfront and caused a ~52 m (~170 ft) run-up near Shoup Bay, while the tectonic tsunami was not even noticed until a high tide late in the evening (Coulter and Migliaccio, 1966; Wilson and Tørum, 1968). On July 25, 2014, a M_w 6.1 strike-slip earthquake on the Fairweather fault occurred underwater near Palma Bay (fig. 2B). This event did not generate a devastating tsunami, due to mostly horizontal displacements of the ocean floor. However, after the earthquake the Alaska Communications Company reported a broken fiber optic cable caused by a submarine landslide in Cross Sound (Suleimani and others, 2015).

One of the largest historical tsunamis generated by a subaerial rock-slope failure occurred in Lituya Bay in 1958 (Miller, 1960). Another massive subaerial landslide occurred near Tyndall Glacier in Taan Fjord—an arm of Icy Bay—in October, 2015 (Rozell, 2016). A mountainside with an estimated volume of 55 million m^3 (72 million yd^3) collapsed into the fjord and caused 190 m (620 ft) run-up on the opposite side (P. Lynett, University of Southern California, oral commun., 2017). According to Geist and others (2003) and Wieczorek and others (2007), another potential massive subaerial landslide can occur in Tidal Inlet—a fjord in Glacier Bay (fig 2B). The tsunami hazard due to this landslide in nearby Alaska communities is assessed by Suleimani and others (2015).

Modeling of waves generated by rockfalls presents a major difficulty. Subaerial landslides, unlike submarine ones, impact water bodies at high speeds and can cause larger tsunamis, given

all other assumptions are the same. The impact of a rockfall on the water surface results in a turbulent splash and consequent mixing of the granular materials with water. Findings by Swanston (1972) and City and Borough of Juneau (2009) mention that several subaerial landslides have occurred within the city limits during the last century. Unfortunately, due to insufficient data on the locations and volumes of potential subaerial landslides, we do not model tsunamis generated by this type of landslide in this report[1].

Presently there is little known about the potential for submarine landslides in the vicinity of Juneau. However, the combination of high sedimentation rates, seismic activity, artificial fill, and history of submarine landslides in Alaska coastal communities with similar geologic settings (such as Seward, Valdez, and Whittier), led us to consider several potential landslides as sources of tsunami waves that could impact Juneau. Figure 3 identifies six potential slide areas, five of which are glacial river deltas deposited on underwater slopes and one of which is an artificial fill location. Later in the report we describe these submarine landslide-generated tsunami scenarios in detail and analyze results of numerical modeling of slide-generated waves.

METHODOLOGY AND DATA

Grid development and data sources

Numerical modeling of the governing equations for water dynamics requires a discrete approximation of the motion of a continuous medium (i.e., the water). In this work we discretize the shallow-water equations in spherical coordinates using a finite difference method. To compute a detailed map of potential tsunami inundation triggered by local and distant earthquakes, we use a series of nested computational grids. A nested grid allows for higher resolution in areas where it is needed without expending computer resources in areas where it is not. The bathymetric and topographic relief in each nested grid is based on digital elevation models (DEMs) developed at the National Center for Environmental Information (NCEI) of the National Oceanic & Atmospheric Administration (NOAA) in Boulder, Colorado (Caldwell and others, 2012). The extent of each grid used for inundation mapping of Juneau is listed in table 2. The coarsest grid (level 0) spans the central and northern Pacific Ocean and has a resolution of 2 arc-minutes (~2 km), while the two highest-resolution grids (level 4 Juneau high-resolution grid and level 4 Tongass Forest high-resolution grid) cover the community (fig. 4). We use three intermediate grids between the coarsest- and highest-resolution grids (table 2). Other grids are employed in testing sensitivity of the tsunami modeling to the grid resolution.

The bathymetry data for the 2-arc-minute-resolution grid is extracted from the ETOPO2 dataset (National Centers for Environmental Information [NCEI], 2006, http://www.ngdc.noaa.gov/mgg/bathymetry/relief.html). The data sources and methodology used to create the 24-, 8-, and 3-arc-second and high-resolution DEMs are described in greater detail in Caldwell and others (2012), Love and others (2012), and Macpherson and others (2014). The horizontal datum for these grids is WGS84, and the vertical datum is MHHW. The spatial resolution of the high-resolution grids satisfies NOAA minimum recommended requirements for computation of tsunami inundation (National Tsunami Hazard Mitigation Program [NTHMP], 2010).

Accuracy of the high-resolution DEM is determined by NASA's Space Shuttle Radar Topography Mission (SRTM) dataset with vertical accuracy of 16 m (52.5 ft) (Caldwell and others, 2012). Because the SRTM data can have large vertical errors near the shoreline, prediction of the potential tsunami inundation using those data can be invalid. Hence this topographic dataset is augmented with the recently developed USGS National Elevation Dataset (NED) that is based on Light Detection and Ranging (lidar) surveys collected in 2013 and a real-time kinematic (RTK) GPS survey in the harbor and airport areas.

The RTK GPS survey in Juneau was conducted October 25, 2013. Locations of the GPS measurements in Juneau are shown in figure 5.

[1]Guidelines and best practices for tsunami inundation modeling for evacuation planning state that the modeling should add value to mapping products (National Tsunami Hazard Mapping Program [NTHMP], 2010).

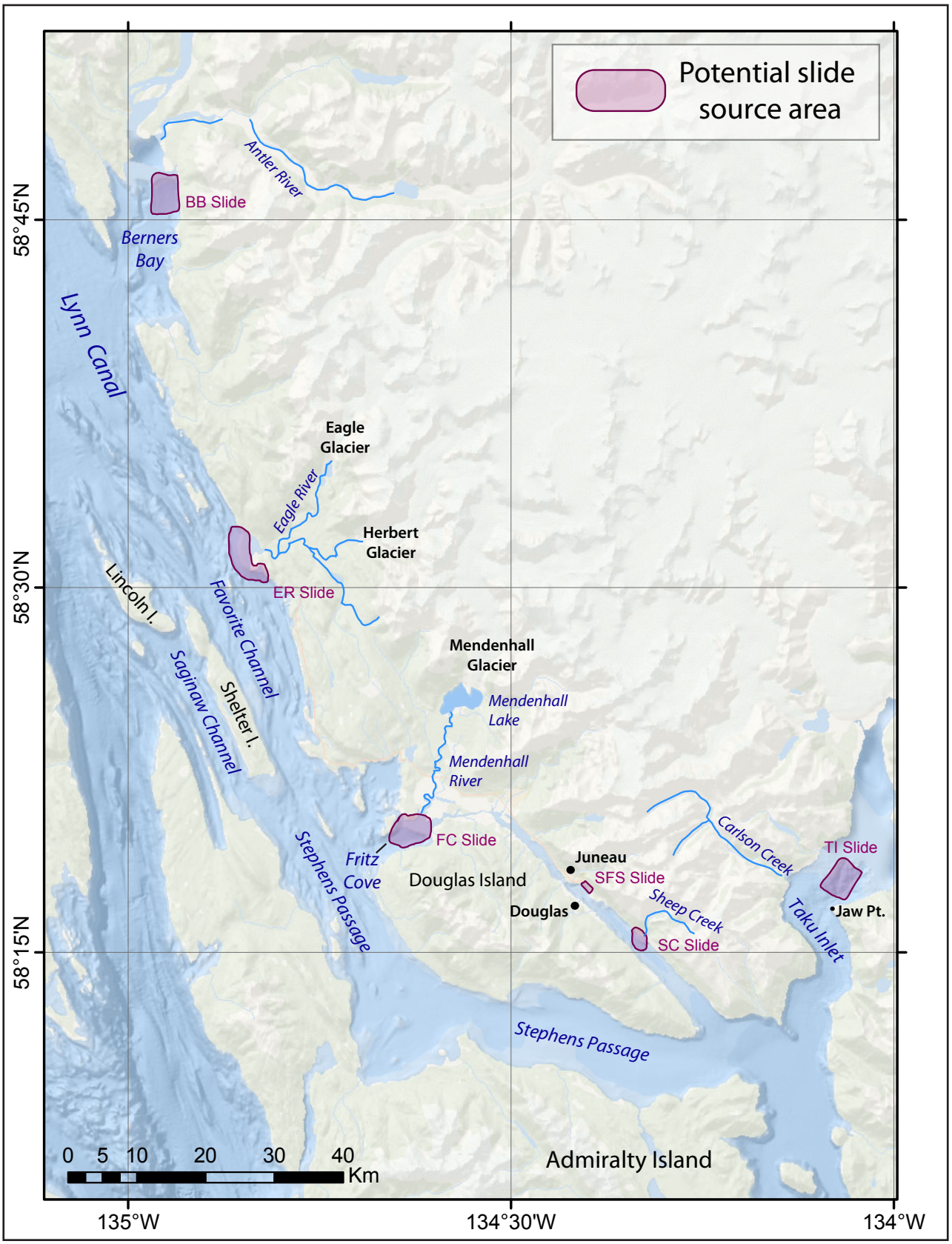

Figure 3. Locations of potential underwater slides in the vicinity of Juneau.

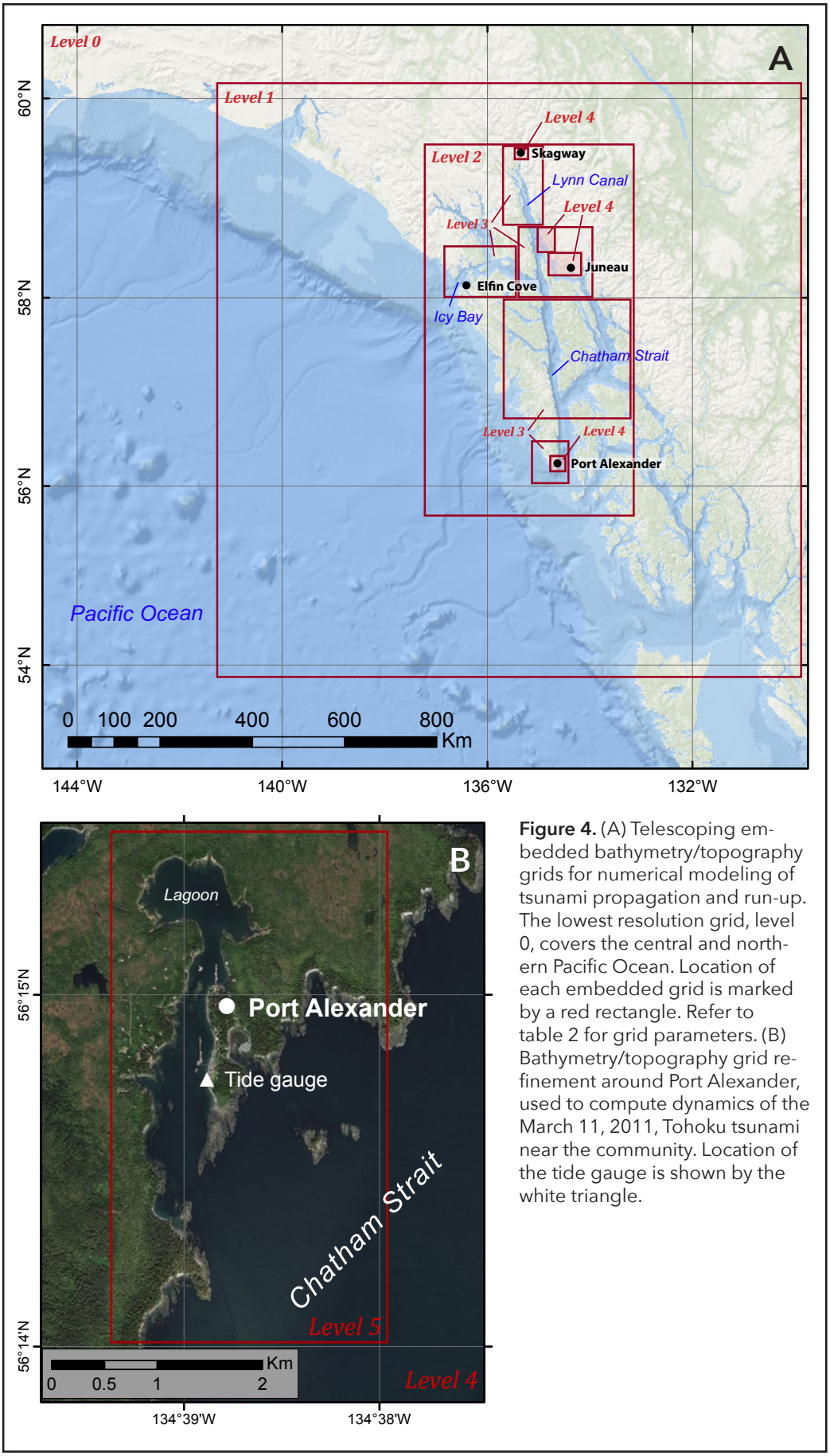

Figure 4. (A) Telescoping embedded bathymetry/topography grids for numerical modeling of tsunami propagation and run-up. The lowest resolution grid, level 0, covers the central and northern Pacific Ocean. Location of each embedded grid is marked by a red rectangle. Refer to table 2 for grid parameters. (B) Bathymetry/topography grid refinement around Port Alexander, used to compute dynamics of the March 11, 2011, Tohoku tsunami near the community. Location of the tide gauge is shown by the white triangle.

Table 2. Nested grids used to compute propagation of tsunami waves generated in the Pacific Ocean to the community of Juneau. High-resolution grids are used to compute the inundation. Grids marked by asterisk (*) are employed in the sensitivity study. Note that the grid resolution in meters is not uniform and is used to illustrate grid fineness near the community. The first dimension is the longitudinal grid resolution, while the second is the latitudinal resolution.

Grid name	Resolution		Longitudinal boundaries	Latitudinal boundaries
	arc-seconds	meters (near Juneau)		
Level 0, Northern Pacific	120" × 120"	1,850 × 3,700	120°00′E – 100°00′W	10°00′N – 65°00′N
Level 1, Southeastern Alaska	24" × 24"	402 × 740	130°00′W – 141°00′W	54°00′N – 60°00′N
Level 2, Juneau West	8" × 8"	132 × 246	133°15′W – 137°17′W	55°44′N – 59°33′N
Level 3, Juneau 3-sec grid	2.7" × 2.7"	44 × 82	133°55′04″W – 135°18′27″W	58°02′21″N – 58°41′40″N
Level 3, Chatham Strait*	2.7" × 2.7"	44 × 82	133°17′W – 135°41′W	56°45′N – 58°00′N
Level 3, Icy Bay*	2.7" × 2.7"	44 × 82	135°20′51″W – 136°53′57″W	58°02′22″N – 58°33′05″N
Level 3, Lynn Canal*	2.7" × 2.7"	44 × 82	134°54′01″W – 135°41′58″W	58°43′45″N – 59°29′58″N
Level 3, Port Alexander*	2.7" × 2.7"	45 × 82	134°24′38″W – 135°07′34″W	56°00′34″N – 56°28′39″N
Level 4, Juneau high-resolution grid	0.9" × 0.53"	14.4 × 16.4	134°18′04″W – 134°47′28″W	58°14′58″N – 58°25′22″N
Level 4, Tongass Forest high-resolution grid	0.9" × 0.53"	14.4 × 16.4	134°45'00''W – 135°00'42''W	58°25′31″N – 58°41′25″N
Level 4, Port Alexander*	0.9" × 0.53"	15.2 × 16.4	134°33'55''W – 134°41'17''W	56°12′56″N – 56°16′42″N
Level 4, Skagway high-resolution grid*	0.9" × 0.53"	13.9 × 16.4	135°17'00''W – 135°22'26''W	59°26′13″N – 59°29′44″N
Level 5, Port Alexander high-resolution grid*	0.3" × 0.18"	5.1 × 5.5	134°37'58''W – 134°39'22''W	56°14′02″N – 56°15′29″N

The collected GPS measurements had 3–5 cm (1.2–2.0 in) lateral and vertical accuracy relative to the base station (Leica Geosystems AG, 2002). Therefore, to achieve sub-meter accuracy for all GPS measurements related to the MHHW datum, the base station datum must relate to the MHHW datum with sub-meter accuracy. Such base station accuracy can be achieved if the base station is set up at a well-known benchmark or monument. We could not find a conveniently located benchmark to allow a sustained radio signal between the base station and a rover for the entire city and chose to set up the base station at the head of Auke Bay. As in previous investigations (Nicolsky and others, 2013, 2015, 2016), we used NOAA tide gauge measurements and GPS-measured water level to convert the collected GPS elevations into the MHHW datum. Figure 6 shows the relation of the GPS-measured water level to the NOAA tide measurements in Juneau.

The extent of the high-resolution USGS NED data is shown in figure 7. The NED dataset is in the North American Vertical Datum of 1988 and

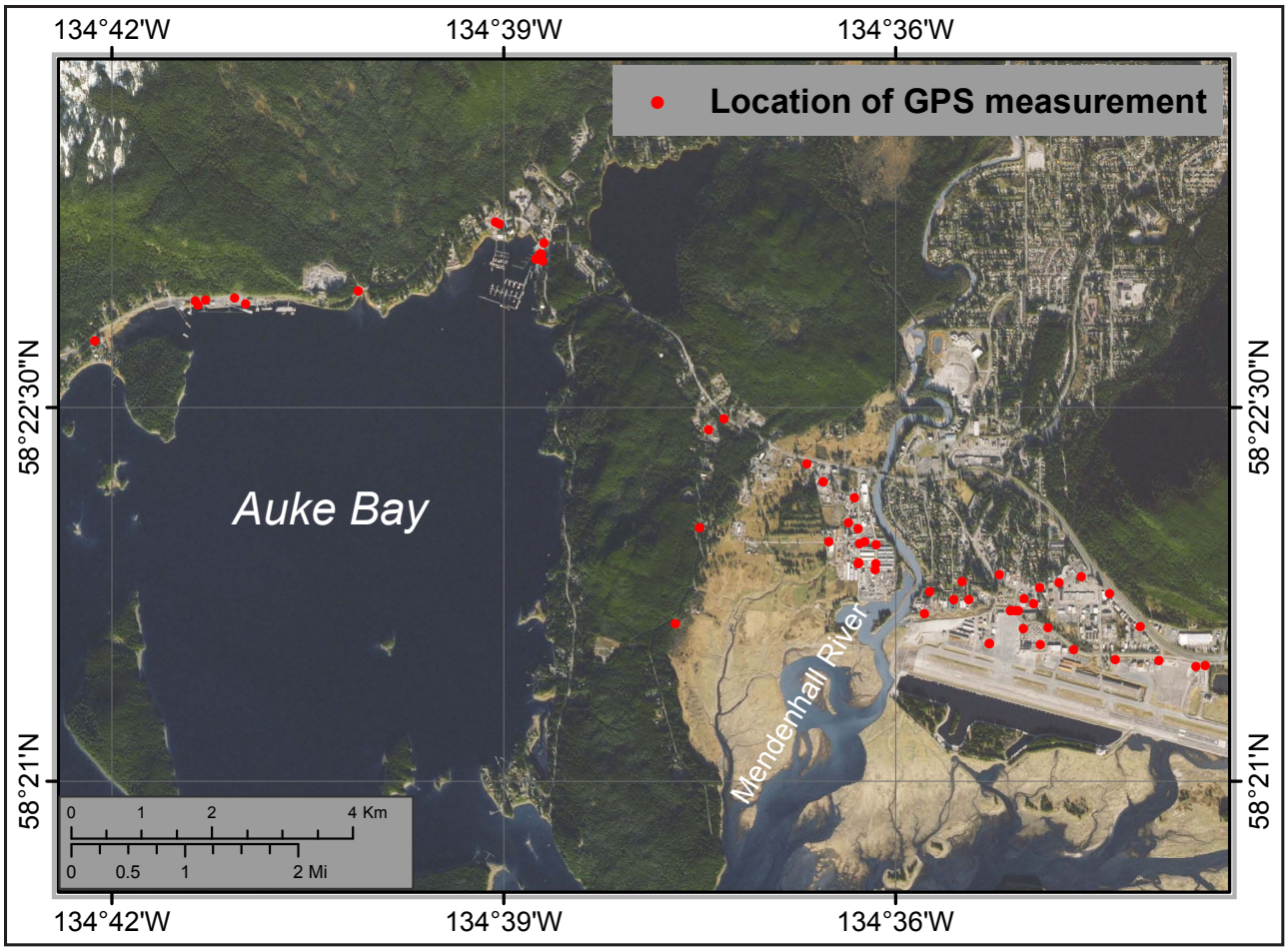

Figure 5. Locations of RTK (real-time kinematic) GPS measurements in Juneau.

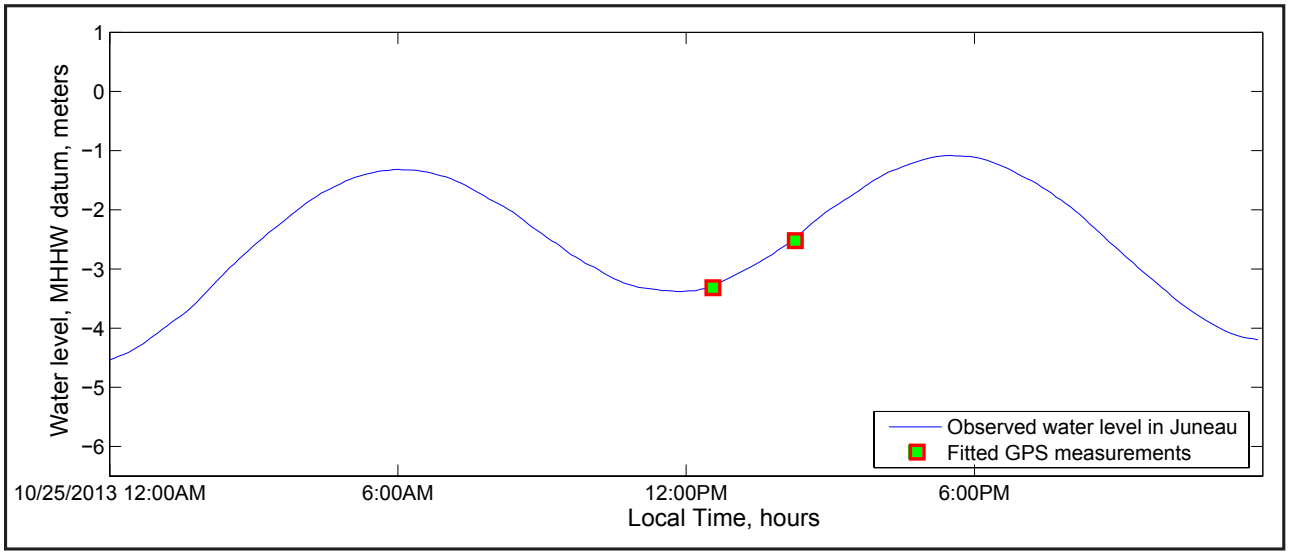

Figure 6. Observed water-level dynamics in Juneau and fitted GPS measurements of water level in the MHHW datum.

requires conversion to the MHHW vertical datum to incorporate with the high-resolution grids. To accomplish this, we sample the NED dataset at locations where the RTK GPS measurements are available and plot the GPS elevations (converted to the MHHW datum) against the NED elevations in figure 8A. We find that dataset elevations are closely correlated, but the NED dataset is vertically offset by 5.0 m (16.4 ft). To adjust the NED to the MHHW datum we subtract 5 m (16.4 ft) from the NED elevations, as shown in figure 8B. We emphasize that the 5 m (16.4 ft) elevation discrepancy corresponds to the vertical difference between the Mean Lower Low Water (MLLW) and MHHW datums. Further investigation regarding the vertical datum of the NED dataset revealed that the lidar dataset, on which the NED dataset is based, was converted to the MLLW vertical datum. The latter supports our correction, which was obtained independently. The values for land areas from the vertically shifted USGS NED dataset were then merged into the existing high-resolution DEM, replacing the original values with the newly interpreted elevations.

Numerical modeling of tsunami wave propagation and run-up

To model propagation of tectonic tsunamis from the the Pacific Ocean to the community of Juneau, we apply the numerical model developed

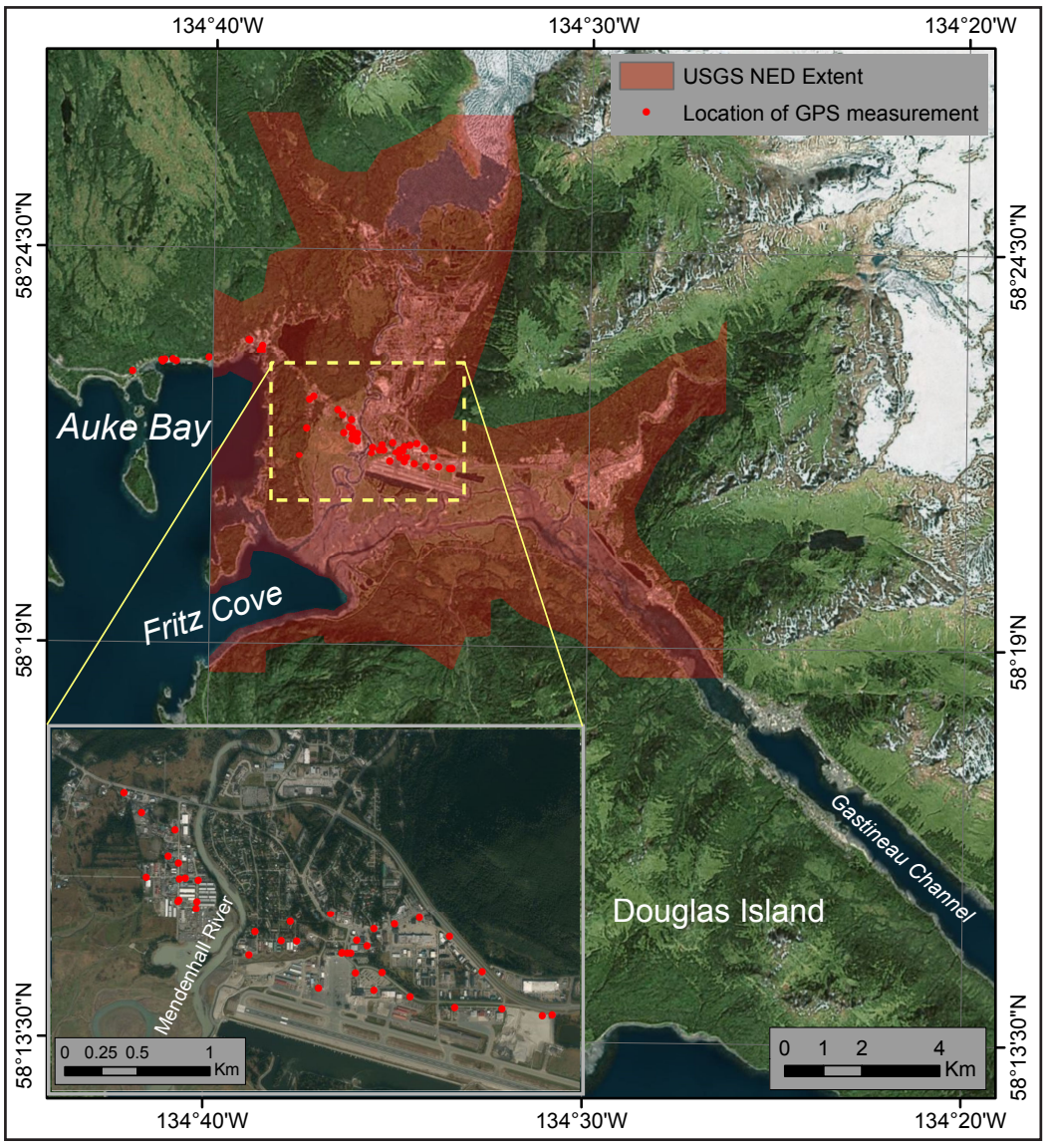

Figure 7. Extent of USGS NED dataset and locations of GPS measurements.

by Nicolsky and others (2011b) and Nicolsky (2012) and used in previous Alaska tsunami inundation studies (for example, Suleimani and others, 2010, 2013, 2015; Nicolsky and others, 2011a, 2013, 2014a, 2014b, 2015). All hypothetical tsunami simulations are conducted using the bathymetric/topographic data corresponding to the MHHW tide level in Juneau. We assume that the initial displacement of the ocean surface is equal to the vertical displacement of the ocean floor induced by the earthquake rupture process. We do not account for the finite speed of the rupture propagation along the fault, and we consider the ocean-bottom displacement to be instantaneous.

Modeling of the March 11, 2011, Tohoku Tsunami

Prior to proceeding with hypothetical scenarios, we verify our model against the observed tsunami generated by the March 11, 2011, M_w 9.0 Tohoku earthquake in Japan. Among many reasons for model verification listed in Synolakis and others (2007), the one that has particular importance for distant tsunami events is ensuring the consistency of the DEM nesting.

The March 11, 2011, Tohoku tsunami resulted in the 21 cm (8.3 in) water wave recorded by the NOAA tide gauge in Juneau (National Geophysical Data Center/World Data Service [NGDC/WDS], in progress). The tsunami was also recorded at tide gauges in Elfin Cove, Port Alexander, and Skagway (fig. 4). The Tohoku tsunami did not result in significant waves in Southeast Alaska because the tsunami traveled a great distance from its source and waves were directed primarily to the northwest, toward the coast of Japan, and to the southeastern region of the Pacific Ocean (Tang and others, 2012). There are no eyewitness accounts of this tsunami at Juneau, probably because of its small size and early arrival time (5:35 am local time). The 2011 Tohoku tsunami arrived on the falling tide and the highest wave arrived when the tide was at its low; the tidal range was 3.7 m (12 ft) on March 11, 2011 (National Oceanic and Atmospheric Administration/National Ocean Service [NOAA/NOS], in progress; https://tidesandcurrents.noaa.gov/waterlevels.html?id=9452210).

There are several deformation models representing the slip distribution of the March 11, 2011, Tohoku earthquake. Here, we apply the finite fault model III by Shao and others (2011). The resulting vertical seafloor deformation is illus-

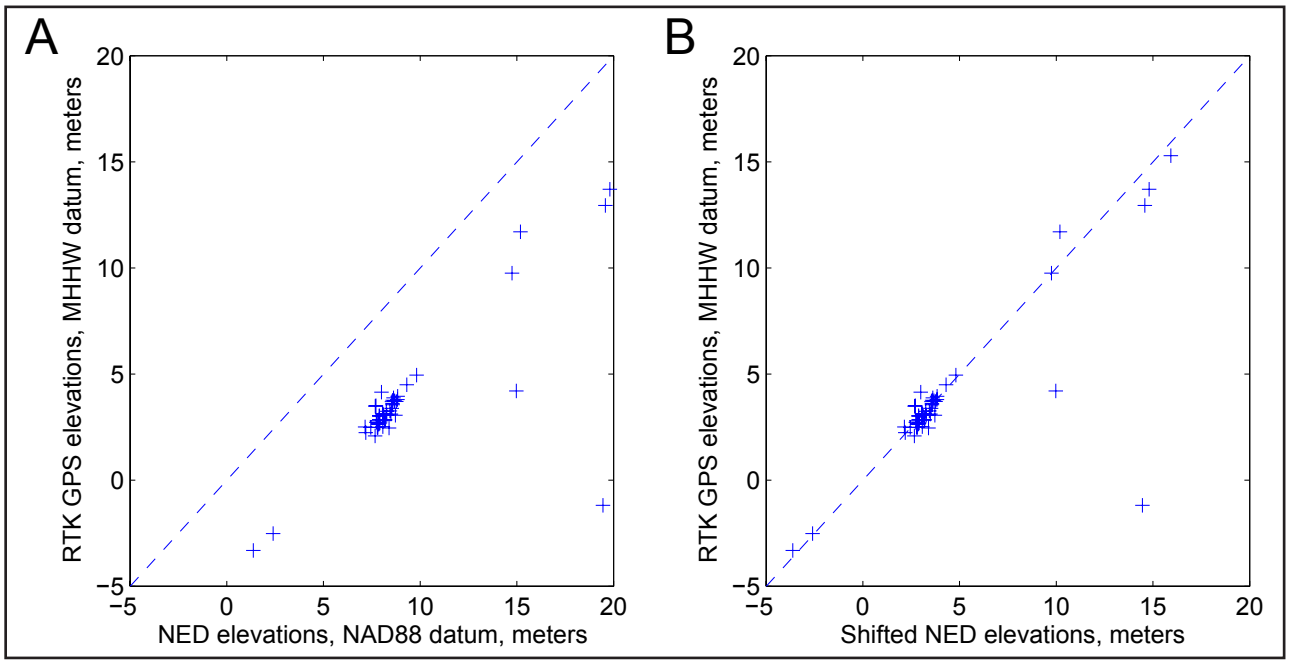

Figure 8. (A) Comparison of the GPS-measured elevations to the NED elevations at the survey locations. (B) Comparison of the GPS-measured elevations to the shifted NED elevations at the survey locations.

trated in figure 9. Similar to Suleimani and others (2013) and Nicolsky and others (2015), we model the 2011 Tohoku tsunami dynamics without considering tidal sea level change; all model runs are conducted using bathymetric data that correspond to the MHHW tide level, if not otherwise noted.

Analysis of the modeling data reveals that the simulated tsunami arrives sooner than the observed one. We apply the time correction of δT = 12 min to the Elfin Cove and Port Alexander time series and δT = 15 min to the Juneau and Skagway time series. Figure 10 shows a comparison between the observed wave histories and the calculated time series at the Elfin Cove, Port Alexander, Juneau, and Skagway tidal stations. The water level observations were processed to remove the tidal component. As reported by Tang and others (2012), a similar time shift was observed between the computed and observed waves in their study. They did not use the tidal stations of Elfin Cove, Juneau, and Skagway in their analysis, but for the Yakutat station they applied the time correction of δT = 12 min. Systematic tsunami traveltime delays (due to elasticity of the solid earth, seawater compressibility, and variations of gravitational potential) occur in many numerical experiments (Watada and others, 2014).

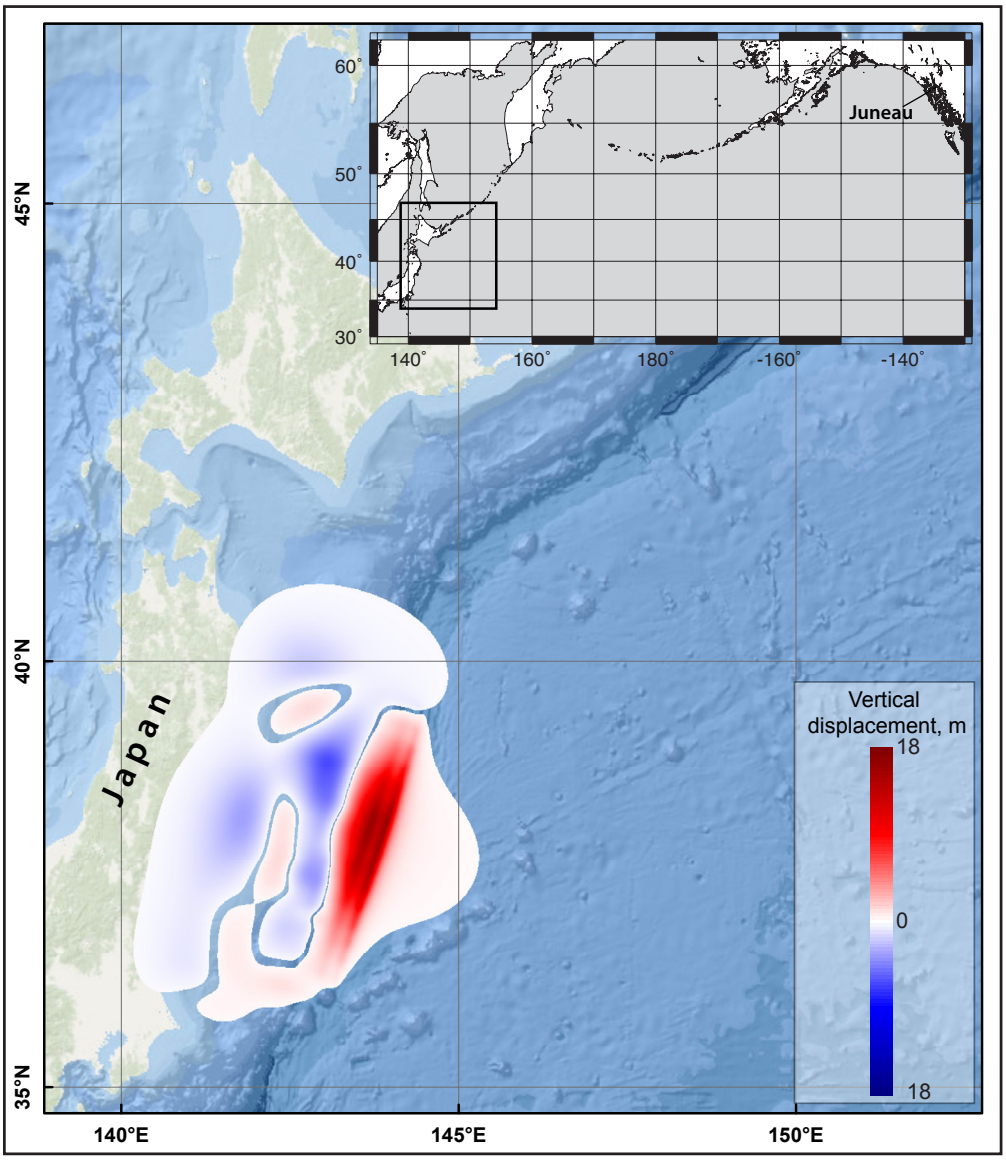

Figure 9. Vertical deformations of the ocean floor and adjacent coastal region corresponding to the March 11, 2011, Tohoku earthquake, based on a finite fault model by Shao and others (2011). Red indicates uplift; blue indicates subsidence. Inset map shows the location of the Tohoku earthquake source with respect to the Juneau tide gauge.

The visual comparison between the computed and measured water-level dynamics at Elfin Cove (fig. 10A) shows that the model provides a good approximation to the recorded tsunami amplitudes for the first ten hours after the wave arrival, i.e., the modeled and observed waves arrive mostly in phase with each other and have similar amplitudes. After ten hours, phases of the modeled and observed waves start to differ and the comparison eventually degrades, as can be seen in the plot at time equal to 20–24 hours after the earthquake. The comparison between the first modeled and observed wave in Port Alexander (fig. 10B) is quite good except that the first wave is slightly underestimated. Close examination of the Elfin Cove results shows that the first observed wave is also slightly underestimated. The underestimation at both tide gauges could be attributed to errors in the 2011 tsunami source model, discrepancies in the bathymetry, and to simplifications of the numerical model.

We also note that tsunami dynamics in Port Alexander are dominated by 9-minute oscillations, and the modeled range of water level variability (black line) is smaller than the observed range. The tide gauge at Port Alexander is at the mouth of the narrow and shallow channel connecting the Chatham Strait to an inland lagoon (fig. 4b). We recall than the tsunami arrived to Southeast Alaska on the falling tide with the tidal range being about 3 m (10 ft). The maximum waves in Port Alexander occurred when the tide was 2.0–2.5 m (6.6–7.1 ft) below the MHHW (National Oceanic and Atmospheric Administration/National Ocean Service [NOAA/NOS], in progress; https://tidesandcurrents.noaa.gov/waterlevels.html?id=9451054). Because our numerical model cannot simulate tidal dynamics, we simulate the 2011 tsunami on the water level corresponding to 2 m (6.6 ft) below the MHHW datum (blue line, fig. 10B). The channel connecting the lagoon to Chatham Strait is much shallower at this water level, if even existent, and thus less water can flow into the inland lagoon. We notice that the range of modeled oscillation is significantly increased and the results are now comparable to the observations. Hence, we conclude that it is important to consider tides at Port Alexander because dynamic opening and closing of narrow, shallow channels has a significant impact on tsunami model accuracy.

For the inside locations, namely, Juneau and Skagway, the numerical model reproduces the first two (fig. 10C) and four waves (fig. 10D), respectively. For the subsequent waves, the reproduction is not as good. The calculated highest wave at Juneau (fig. 10C) underestimates its recorded counterpart by ca. 50 percent. The discrepancy could be due to: a) effects of bottom friction; b) coarse resolution of intermediate grids describing the complex network of channels and passages that lead to Juneau from the Pacific coast; c) positive interference between various oscillation patterns in the fjord system; or d) tsunami-tide interactions. In the rest of this section, we conduct a series of tests to analyze which of the above mechanisms is likely to be responsible for underestimation of the maximum tsunami wave height in Juneau.

First, we compare the modeled tsunami in Juneau with results of two numerical experiments, in which bathymetry is refined in a) Icy Bay only and b) in both Icy Bay and Chatham Strait (see table 2 for DEM list). The numerical results are plotted in figure 11A. The grid refinement in only Icy Bay does not result in any visibly distinguishable changes to the water dynamics in Juneau. However, the grid refinement of both Icy Bay and Chatham Strait produces slightly decreased maximum wave heights in Juneau. The numerical experiment with a smaller bottom friction (the surface roughness coefficient n in the Manning formula is decreased four times to n=0.005 $s/m^{1/3}$ [0.007 $s/ft^{1/3}$]) results in decreased maximum wave height in Juneau (fig. 11B). We emphasize that in all experiments the first wave crest and trough are almost the same and the difference between the numerical results is seen in the second wave crest.

Finally, similar to the tsunami dynamics in Port Alexander, the maximum tsunami wave in Juneau occurred when the tide was near its minimum,

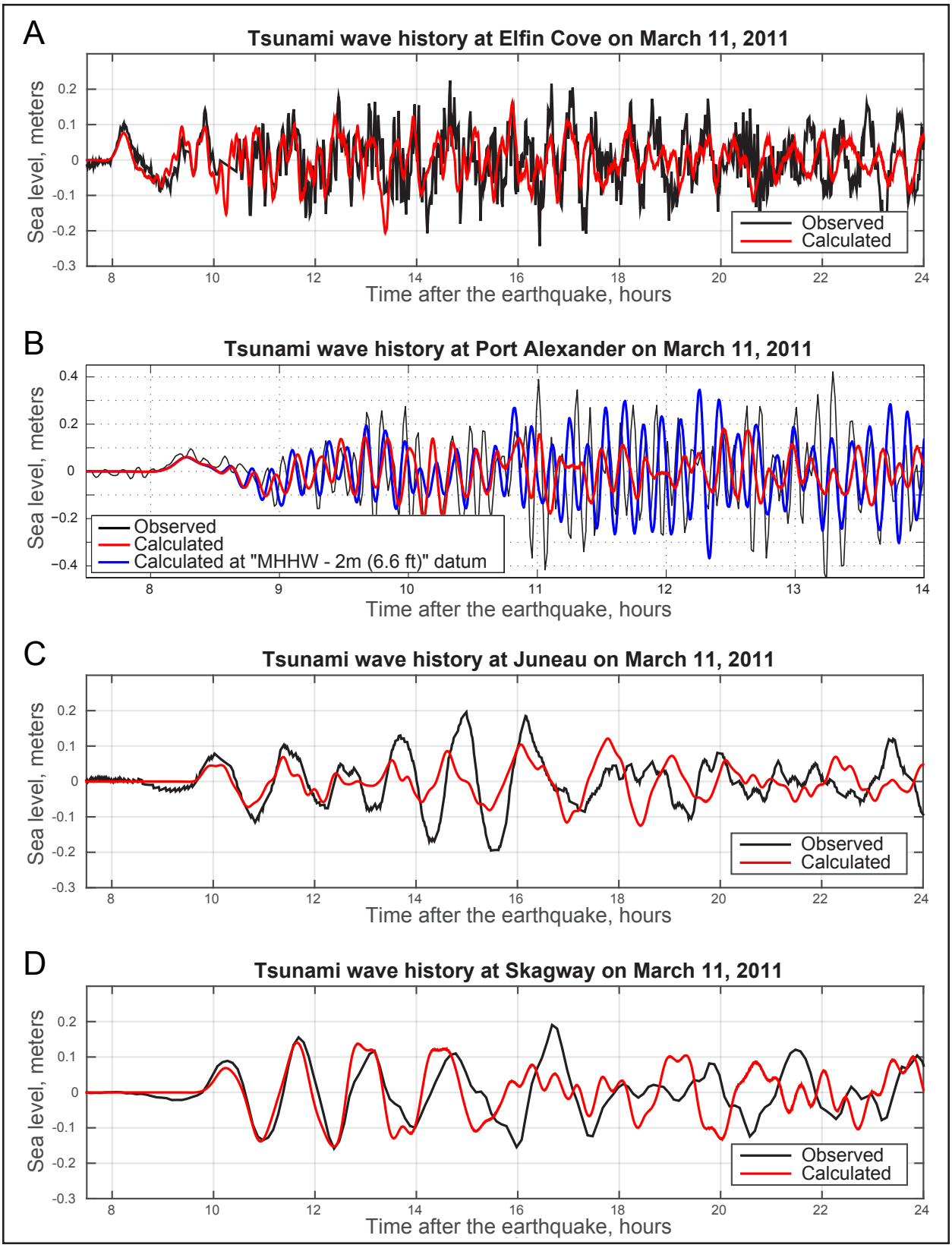

Figure 10. Observed and simulated water-level dynamics for the March 11, 2011, Tohoku tsunami at (A) Elfin Cove, (B) Port Alexander, (C) Juneau, and (D) Skagway tide stations. All simulations are carried out with the assumption that the still water level is at the MHHW level (no ocean tides in the model), except for the Port Alexander simulation. One of the simulations for Port Alexander was completed with the still water depth at 2 m (6.6 ft) below the MHHW level (blue line).

in this case 4 m (13 ft) below the MHHW level. Therefore, we conduct a numerical experiment in which the undisturbed water level corresponds to the tide level when the second tsunami wave crest arrives, i.e., 3 m (10 ft) below the MHHW datum. The modeled water level in Juneau is shown by the green line in figure 11B. Despite the fact that Juneau is connected to the ocean by deep channels (100–300 m [300–1,000 ft]), the 3 m (10 ft) reduction in the undisturbed water depth produces significant changes to the water level dynamics in Juneau, helping to better match modeled maximum wave heights with those that were observed.

We hypothesize that changes in various model parameters (i.e., water depth, bathymetric resolution, and bottom friction) cause slight perturbations in natural oscillations in the fjord system. For example, modeling tsunamis on the reduced water level (the still water depth in the fjords is shallower) results in decreased periods of water level oscillations. Because Juneau is surrounded by a complex system of fjords, and if the fjord system oscillates on similar frequencies, the overall oscil-

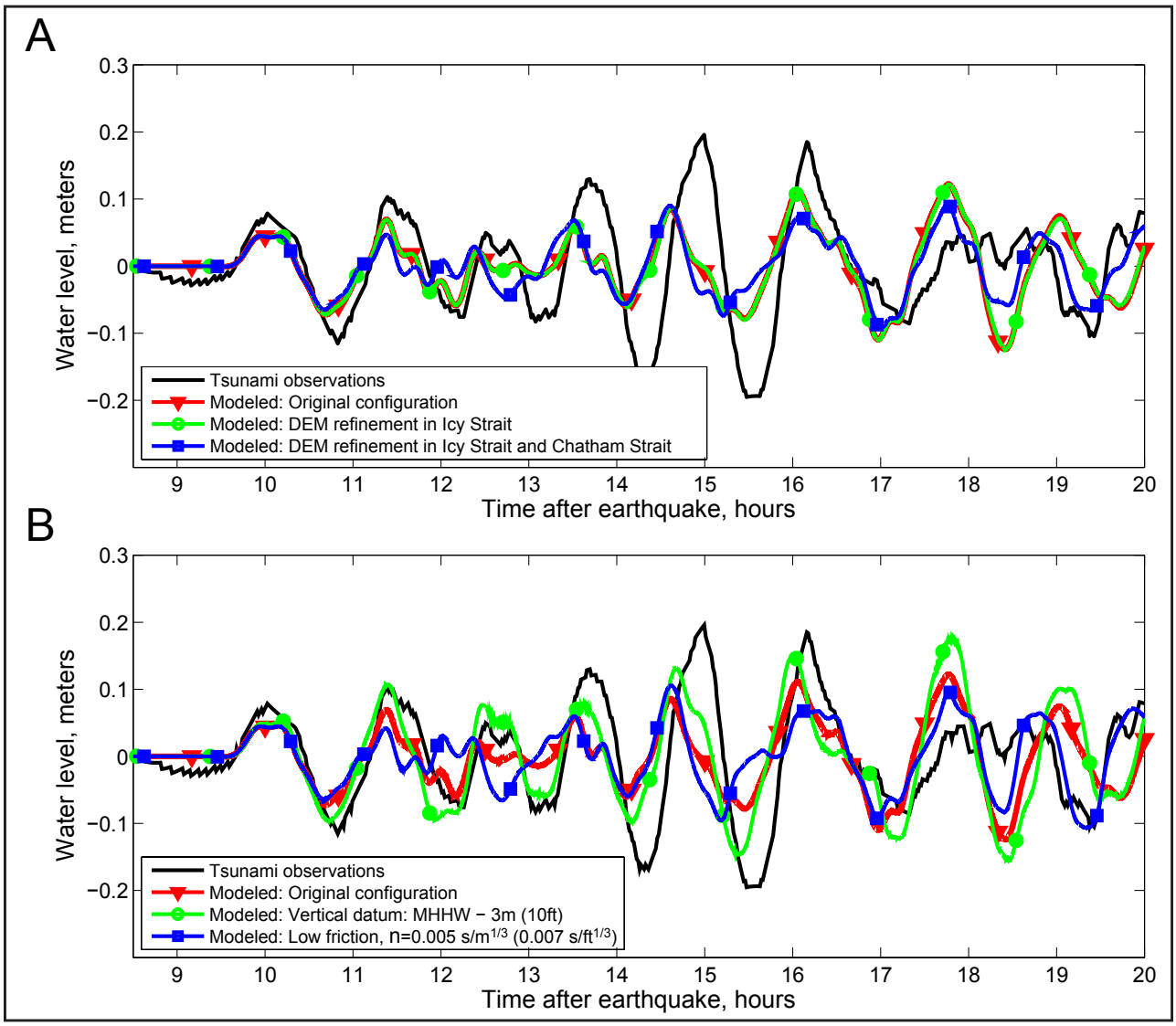

Figure 11. Comparison of the observed March 11, 2011, Tohoku tsunami in Juneau to its modeled counterpart. The latter was computed for various perturbations of parameters: (A) refinement of the topography/bathymetry grids near Juneau, (B) changes in the bottom friction and still water depth.

lation looks like a single oscillation with a slowly varying amplitude. Depending on the difference between the individual frequencies, the overall oscillation pattern can experience positive and negative interference among its constituents. As a result, oscillations with nearly the same periods can lead to gradual amplification of the water waves. After the initial amplification, the individual oscillations can destructively interfere with each other and decrease the wave height. We notice that for both the observed and modeled tsunamis, wave crests increase in height for the first few hours (<12 hrs after earthquake) then decrease in height after another ~6 hours (~18 hours after the earthquake).

Among the considered parameters, tide level variations and tidal dynamics, in general, seem to have the greatest effect on the natural oscillation patterns of the waves in Juneau. A similar physical mechanism is likely amplifying the wave in Skagway. Unfortunately, tide-tsunami coupling is a rather complicated problem (Kowalik and others, 2006; Kowalik and Proshutinsky, 2010) and its solution needs extensive exploration and validation before application in the tsunami hazard assessments. Therefore, to account for the model's underestimation of the potential tsunami impact for Juneau, we correspondingly adjust the tsunami sources as discussed later in the report.

Numerical model of landslide-generated tsunamis

Tsunamis generated by submarine landslides are complex physical phenomena, the study of which accelerated following the 1998 Papua New Guinea (PNG) earthquake (e.g., Tappin and others, 2001, 2008). In this particular event, the M_w 7.1 earthquake triggered an underwater slump that produced a tsunami with a 15 m local inundation, killing almost 2,200 people (Tappin and others, 2008). After the PNG tragedy, in order to minimize future losses, a number of models to simulate water dynamics due to submarine landslides have been developed (e.g., Fine and others, 1998; Grilli and Watts, 1999; Watts and others, 2003; Lynett and Liu, 2002; Skvortsov and Bornhold, 2007; Løvholt and others, 2008; Weiss and Wünnermann, 2009; Horrillo and others, 2013; Ma and others, 2013; George and Iverson, 2014).

Modeling landslide-generated tsunamis involves simulation of not only the water and landslide, but also the coupling between them. The water dynamics are computed by potential flow theory, Navier-Stokes equations, or a variety of depth-averaged equations. The landslide dynamics are either prescribed according to some simple formulae or modeled according to the assumed rheology. In general, the slide rheology could be described by a dense Newtonian (viscous) fluid, Bingham (viscoplastic) fluid, granular flow, or simply by a non-deformable solid body (Harbitz 1992; Jiang and LeBlond 1992, 1993; Iverson and Denlinger, 2001). See Løvholt and others (2015), Grilli and others (2016), and Yavari-Ramshe and Ataie-Ashtiani (2016) and references therein for a list of developed numerical models and their classifications.

In a recent study to simulate the 1975 Kitimat, British Columbia, submarine landslide, Kirby and others, (2016) investigated landslide models with viscous, viscoplastic, and solid body rheologies. The viscous deformable slide model was found to predict somewhat lower wave heights than the solid slide model. The solid slide also produced results comparable to the viscoplastic slide model developed by Skvortsov and Bornhold (2007). Similarly, Ataie-Ashtiani and Najafi-Jilani (2008) and Najafi-Jilani and Ataie-Ashtiani (2008) experimentally showed that granular slides had a maximum amplitude up to 15 percent smaller than that of the equivalent rigid slide. Therefore, the solid body landslides are likely to produce the most extensive inundation; however, most of the errors/uncertainty in the computed inundation originates from the landslide source characterization. For instance, according to Kirby and others (2016), model results indicate that the strongest influence on the amplitude of generated waves

is the slide volume, with changes in slide shape (with the volume held constant) playing a lesser role. The initial acceleration, and hence the slide density and slope of the ocean bottom, also significantly affects the wave height. Furthermore, an initial shallow submergence—which enhances tsunami generation—as well as proximity to the shore also significantly influence the run-up of landslide-generated tsunamis.

In this report, to simulate tsunamis produced by hypothetical underwater slope failures in channels and canals near Juneau, we use a numerical model by Kirby and others (2016) with two fully coupled components: a depth-integrated layer of Newtonian viscous fluid for the landslide model (Jiang and LeBlond 1992; Fine and others, 1998) and a shock-capturing Non-Hydrostatic Wave (NHWAVE) model by Ma and others (2012). The depth-integrated model for the slide was successfully applied to simulate landslides in Alaska (Fine and others, 1998; Suleimani and others, 2011) and was later used to assess tsunami hazards in Seward, Whittier, and Valdez (Suleimani and others, 2010; Nicolsky and others, 2011a, 2013). The NHWAVE model was designed to model fully dispersive surface wave processes by solving the non-hydrostatic Navier–Stokes equations in a domain over a surface and terrain in the sigma coordinate system. Performance of NHWAVE has been verified and validated in Tehranirad and others (2012) for a series of benchmarks provided by Synolakis and others (2007), and a landslide benchmark developed from results in Enet and Grilli (2007). The coupling of the NHWAVE model to the viscous landslide model was recently tested using measurements from laboratory experiments by Grilli and others (2016). Unfortunately, a comprehensive set of numerical benchmarking procedures for models describing a deformable slide and its coupling with water waves has yet to be developed.

Because NHWAVE discretizes the water column into several layers, run-up modeling is a computationally expensive task due to the strict Courant–Friedrichs–Lewy (CFL) condition on the vertical water velocity (Courant and others, 1928). Therefore, we selected a vertical threshold of 0.1 m (0.3 ft) instead of 0.01 m (0.4 in) to model inundation in NHWAVE. The latter value is commonly used to simulate inundation by depth-averaged shallow water equations. To increase confidence in predicting the extent of inundation from landslide-generated waves we employ FUNWAVE-TVD—a phase-resolving, time-stepping Boussinesq model for nearshore ocean surface-wave propagation (Shi and others, 2012), described below.

First, we simulate wave generation caused by the motion of a viscous landslide down the fjord slope using the fully coupled model (Kirby and others, 2016). At the beginning of each numerical experiment, when the submarine slide initially propagates down the fjord wall, it pushes water and creates a positive wave propagating away from the slide. Behind, at the original slide location, an initial water surface depression occurs and it is consequently filled with water under the restoring force of gravity. The wave radiation patterns created by slide dynamics are complex and usually include a series of crests and troughs radiating away from the slide area. Løvholt and others (2015) provide an in-depth description of landslide tsunami generation. When the slide reaches a fjord bottom, most of its energy has already been transferred to the water. At this moment, execution of the fully coupled model is terminated. The resultant water level and the water velocities (depth-averaged across all layers in NHWAVE) are used as initial conditions for the FUNWAVE model. FUNWAVE then models a potential inundation of dry land with a 0.01 m (0.4 in) threshold between dry and wet cells. We stress that the threshold for the FUNWAVE model is smaller than the one used in NHWAVE and this allows for more accurate calculations of potential inundation. A similar two-stage approach is implemented to simulate inundation along the U.S. East Coast (Grilli and others, 2013) and the Gulf of Mexico (López-Ven-

egas and others, 2014), where the sliding area and the coast are not adjacent to each other.

In many fjords, potential underwater slides exist along the city waterfront, often in areas of unknown inundation susceptibility (Nicolsky and others, 2011a; 2013). Thus the initial water-level depression could be directly adjacent to a community, as was the case in Valdez during the 1964 earthquake (Coulter and Migliaccio, 1966). In these scenarios, we transfer the water level and velocities from the fully coupled model to FUNWAVE when the initial depression is refilled, and the "rebound" crest starts to propagate onshore. We also check that by this time most of the slide mass has reached the fjord bottom. Because there is uncertainty in choosing the specific moment of time when the rebound crest has developed, we transfer the water level and velocities for two distinct occasions, i.e., separated by 30 seconds in time. The uncertainty is later assessed by comparing water dynamics predicted by the fully coupled model and the FUNWAVE model at certain locations around the bay. The extent of potential inundation from the landslide scenario encompasses the inundation extent of the NHWAVE model and of both realizations of the FUNWAVE model.

Hypothetical tectonic tsunami sources

In this section, we consider several tectonic tsunami sources to develop tsunami hazard maps for the community of Juneau. We follow the notations of Nishenko and Jacob (1990) for megathrust segmentation: Yakataga–Yakutat (YY), Prince William Sound (PWS), Kenai Peninsula (KP), Kodiak Island (KI), Semidi Islands (SEM), and Shumagin Islands (SH) (fig. 1).

The many islands, channels, and passages that characterize the landscape near Juneau may provide protection to the city by dissipating tsunamis that hit the outer coast of southeastern Alaska; conversely, the passages also serve as wave guides to channel the tsunami energy to Juneau. Analysis of available bathymetry charts shows that waves can reach Juneau primarily by two routes: from the west through Icy Strait, and from the south through Chatham Strait and Stephens Passage (fig. 2A). In a recently completed study by Suleimani and others (2015), tsunamis generated by earthquakes along the KI, KP, PWS, and YY segments are thought to be worst-case scenarios for the Icy Strait communities: Elfin Cove, Gustavus, and Hoonah. Because Juneau is located farther inland along the same tsunami propagation route, we consider the same tsunami scenarios considered in the Icy Strait study for the Juneau study. We also consider tsunamis propagating north through Chatham Strait and Stephens Passage, and model a tsunami generated by an earthquake in the Cascadia subduction zone along the Washington–Oregon coast.

To parameterize co-seismic slip distributions for tectonic scenarios, we employ a discretization of the Alaska–Aleutian plate interface (Hayes and others, 2012) between the subducting and overriding plates. The interface is discretized into a set of 10–15 km-long rectangles with the upper and lower edge of each rectangle being coincident with a 1-km depth contour of the interface. The value of slip is prescribed to each patch (subfault) and its contribution to the overall coseismic deformation is consequently computed by Okada (1985) formulae. The value of rake—the direction a hanging wall block moves during rupture—is assumed to be 90° in order to maximize coseismic deformation for the given slip. All contributions from subfaults are added together to derive the co-seismic deformation associated with the considered scenario. The rigidity modulus is assumed to be a constant $3.6*10^{10}$ N/m^2 and independent of depth. Therefore, all listed values of M_w for the hypothetical scenarios provide a qualitative assessment for the moment magnitudes.

Table 3 provides a summary of all tectonic scenarios considered in this report. Scenarios marked by an asterisk (*) indicate scenarios described in previously published modeling studies by Suleimani and others (2015, 2016). As in previous investigations (Nicolsky and others, 2011; Suleimani and others, 2015, 2016), we consider models of the 1964 earthquake.

Table 3. Hypothetical tectonic scenarios used to model tsunami run-up in Juneau. Scenarios marked by an asterisk (*) indicate scenarios described in the previously published modeling studies by Suleimani and others (2015, 2016).

#	M_w	Description	Maximum slip, m (ft)	Average slip, m (ft)	Maximum subsidence, m (ft)	Maximum uplift, m (ft)
1	9.2	Repeat of the 1964 M_w 9.2 Alaska Earthquake	23 (75)	10 (33)	5.5 (18)	9 (30)
2	9.3	Earthquake modeling extension of the 1964 rupture to the YY segment	23 (75)	15 (49)	5.5 (18)	9 (30)
3*	9.2	Tohoku-type earthquake in the area of the 1964 rupture	37 (120)	9 (30)	4 (13)	14 (48)
4*	9.2	Tohoku-type earthquake in the area of the 1964 rupture and YY segment	37 (120)	11 (34)	4.5 (15)	10 (33)
5*	9.0	Tohoku-type earthquake across Prince William Sound and Kenai Peninsula	44 (144)	22 (72)	8 (26)	14 (44)
6*	9.0	Earthquake according to the SAFRR project	75 (245)	16 (52)	3 (9)	15 (49)
7*	9.1	Earthquake in the Cascadia subduction zone along the British Columbia, Washington, Oregon and northern California shore	45 (148)	36 (118)	8 (25)	11 (35)

Scenario 1. Repeat of the 1964 M_w 9.2 Alaska Earthquake (fig. 12A).

Over the last two decades, several models of coseismic deformation for the M_w 9.2 Great Alaska Earthquake were developed by Johnson and others (1996), Ichinose and others (2007), Suito and Freymueller (2009), and Suleimani (2011). Most of the difference between them is in distribution of slip and extent of the splay faults along the Kenai Peninsula. Maximum slip across all sources is 23 m (75 ft); average slip is 10 m (33 ft).

We conduct numerical simulations for each of the above-mentioned coseismic deformation models. An envelope of the maximum inundation extents among all of these models is used to define the hypothetical inundation according to this scenario.

In a paleoseismic study, Hamilton and Shennan (2005) estimated coseismic subsidence during the 1964 earthquake and two earlier events. It was shown that the earthquake dated to 1,500–1,400 years B.P. produced more than twice the subsidence caused by the 1964 earthquake. By comparing Kenai Peninsula sites with other sites around Cook Inlet, the authors find that each of the three great earthquakes in the study had a different pattern of coseismic subsidence. Recent work by Shennan and others (2008) tests the hypothesis that in some seismic cycles PWS, KK, KP, and YY megathrust segments can rupture simultaneously to produce earthquakes of greater magnitude than historical events. They present geologic evidence of six prehistoric major tsunamigenic earthquakes in the Kenai Peninsula area of south-central Alaska in the past 4,000 years based on radiocarbon ages of tidal marsh deposits in Girdwood. They find paleoseismic evidence that earthquakes approximately 900 and 1,500 years B.P. simultaneously ruptured three adjacent segments of the Aleutian megathrust: the PWS, KI, and YY segments. The rupture area of these earthquakes was estimated to be 23,000 km^2 (8,880 mi^2) greater than that of the M_w 9.2 Great Alaska Earthquake of 1964, and with a 15 percent larger seismic moment. Therefore, we constructed a hypothetical tsunami scenario based on the extended 1964 source.

Scenario 2. M_w 9.3 earthquake modeling extension of the 1964 rupture to the YY segment (fig. 12B).

We develop extensions of the four above-mentioned coseismic deformation models for the 1964 event by adding to each of them a coseismic deformation in the YY segment. The latter deformation is based on scenario 5 in Nikolsky and others (2013). We note that extensions of Johnson's and Suleimani's models were used as scenarios 1 and 2 in Suleimani and others (2013) to assess potential inundation in Sitka. Maximum slip across all sources is 22–23 m (72–75 ft); average slip is 13–15 m (43–49 ft).

We conduct numerical simulations for each of the considered coseismic deformation models. An envelope of maximum potential inundation extents among all of these models is used to define the hypothetical inundation according to this scenario.

Following lessons learned from the March, 11, 2011, M_w 9.0 Tohoku earthquake and tsunami (Ito and others, 2011), and given similarities between the Alaska and Tohoku subduction margins (Ryan and others, 2012; Kirby and others, 2013), we propose that a hypothetical rupture might propagate to shallow depths and produce a large amount of slip close to the trench. Therefore, we also consider tsunami scenarios (scenarios 3–5) in the Gulf of Alaska—the most sensitive location for Southeast communities due to the directivity of the tsunami propagation pattern.

Scenario 3*. M_w 9.2 Tohoku-type earthquake in the area of the 1964 rupture (fig. 12C).

This scenario is the same as scenario 2 in Suleimani and others' (2015) tsunami modeling study for Elfin Cove, Gustavus, and Hoonah. Maximum slip is 37 m (120 ft); average slip is 9 m (30 ft).

Scenario 4*. M_w 9.2 Tohoku-type earthquake in the area of the 1964 rupture and YY segment (fig. 12D).

This scenario is the same as scenario 4 in Suleimani and others' (2016) tsunami modeling study for Yakutat. Maximum slip is 37 m (120 ft); average slip is 11 m (34 ft).

Scenario 5*. M_w 9.0 Tohoku-type earthquake across Prince William Sound and Kenai Peninsula (fig. 12E).

This scenario is the same as scenario 3 in Suleimani and others' (2015) tsunami modeling study for Elfin Cove, Gustavus, and Hoonah. Maximum slip is 44 m (144 ft); average slip is 22 m (72 ft).

We supplement the above scenarios with two additional scenarios. First, we consider a scenario developed by the USGS Science Application for Risk Reduction (SAFRR) project to describe the impacts of a tsunami generated by an earthquake in the Alaska Peninsula region to the coastline of Southern California (Ross and others, 2013). We also consider a scenario along the Oregon-Washington coast. Although a rupture of the Cascadia subduction zone is not a worst-case scenario for the Juneau area, for the sake of community preparedness we simulate a large hypothetical earthquake along the western seaboard of the U.S.

Scenario 6*. M_w 9.0 earthquake according to the SAFRR project (fig. 12F).	This scenario is the same as scenario 5 in Suleimani and others' (2015) tsunami modeling study for Elfin Cove, Gustavus, and Hoonah. Maximum slip is 75 m (245 ft); average slip is 16 m (52 ft).
Scenario 7*. M_w 9.1 earthquake in the Cascadia subduction zone along the British Columbia, Washington, Oregon, and northern California shore (fig. 12G).	This scenario is the same as scenario 7 in Suleimani and others' (2015) tsunami modeling study for Elfin Cove, Gustavus, and Hoonah. Maximum slip is 45 m (148 ft); average slip is 36 m (118 ft).

The regions of the Aleutian megathrust that correspond to the aforementioned scenarios are ~1,000 km (~620 mi) from Juneau, while the northern part of the Cascadia subduction zone source is about 1,200 km (750 mi) from town. Therefore, all scenarios result in zero coseismic land change in Juneau.

Hypothetical landslide tsunami sources

In addition to the hypothetical tectonic scenarios, we consider several submarine landslide scenarios that could generate hazardous waves along the Juneau waterfront. Swanston (1972) conducted an overview of subaerial landslide hazards in Juneau, but subaerial landslides are not considered in this report because of the significant uncertainty associated with specifying their potential location and volume.

Overviews of submarine landslides in waters close to Alaska are presented by Schwab and others (1993), Kulikov and others (1998), and Lee and others (2006). Additionally, Lemke (1967), Wilson and Tørum (1968), Plafker and others (1969), and Shannon and Hilts (1973) conducted geologic investigations after the 1964 earthquake in numerous locations around south-central and southeastern Alaska. One of the resounding conclusions from these studies is that accumulation of loose deltaic sediment on underwater slopes causes over-steepening of fjord walls and contributes directly to underwater slope instability. During an earthquake, dynamic forces imposed by seismic acceleration add to the gravitational force and triggers sliding of the unconsolidated sediments (Hampton and others, 2002). The major factors contributing to total slide volume and extent are thought to be the duration of ground motion, configuration of underwater slopes, and type of sediment forming these slopes (e.g., unconsolidated or fine-grained materials are more prone to failure). Therefore, artificial fill areas and glacial creek deltas are especially susceptible to sliding and are considered as locations for potential landslides (Nicolsky and others, 2011a, 2013; Suleimani and others, 2010, 2015, 2016).

Because there is practically no geotechnical data for submarine sediments along the Juneau waterfront, we employ a heuristic approach to develop a set of hypothetical landslide scenarios. First, we identify creek deltas and artificial fill areas near the community. Next, we assume generic, bowl-shaped failure surfaces in the ground material at the identified locations based on the generic parameters of landslides investigated after the 1964 earthquake (Nicolsky and others, 2013; Suleimani and others, 2015, 2016). Without geotechnical information we lack data to support alternative, more complicated slide plane geometries. After the failure surfaces are defined, we interpolate between the failure surfaces and compute a thickness of the potential slide mass and estimate its volume. The slide volume and thickness are compared to well-studied historical submarine landslides in Alaska as follows.

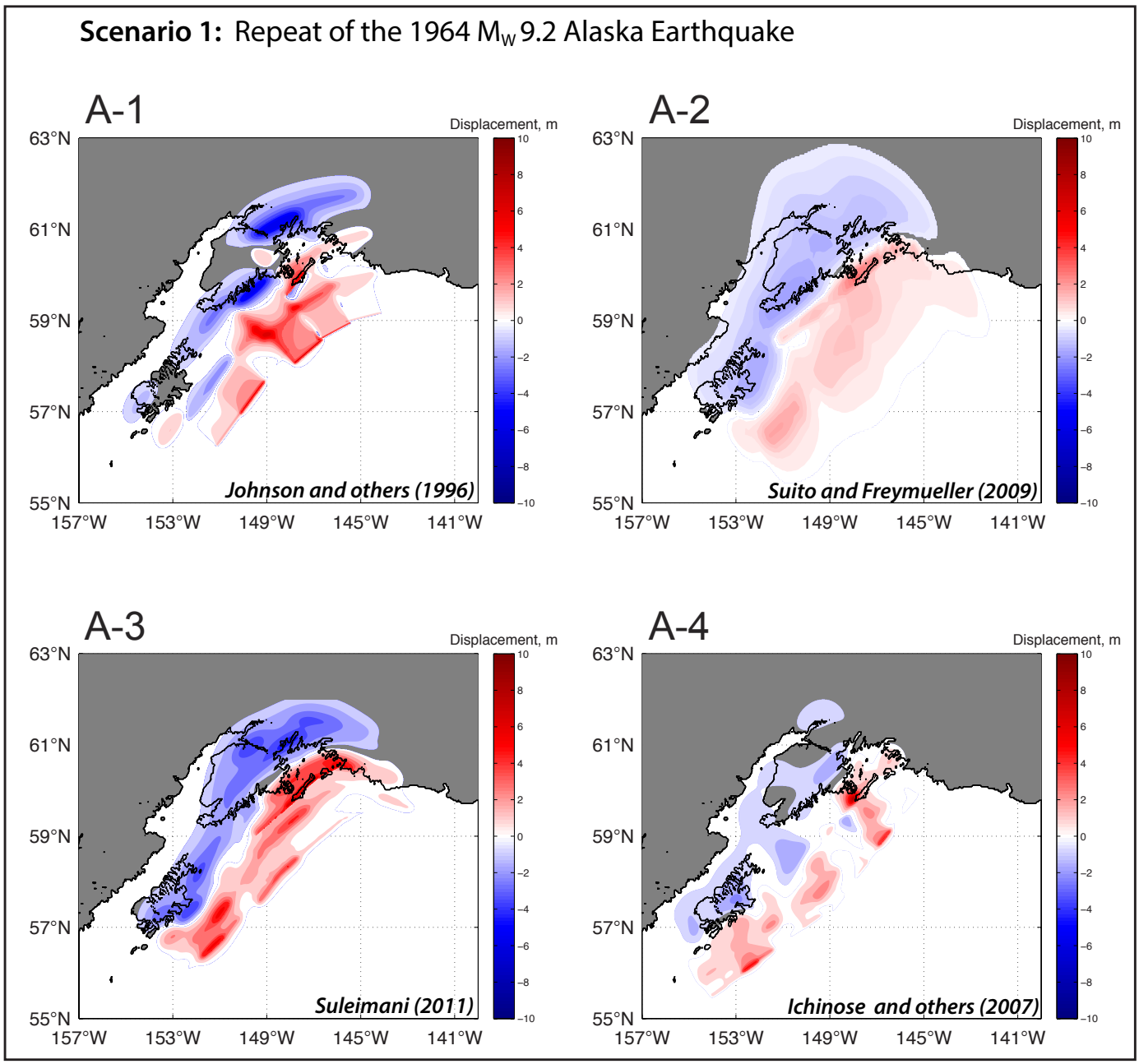

Figure 12. (A) Computed vertical ground-surface deformation related to scenario 1: Earthquake modeling of the 1964 rupture. Ground-surface deformation for all other tectonic scenarios (2-7) are shown in figures 12B-G. Blue shaded areas are associated with coseismic ground subsidence; areas of uplift are shown in red.

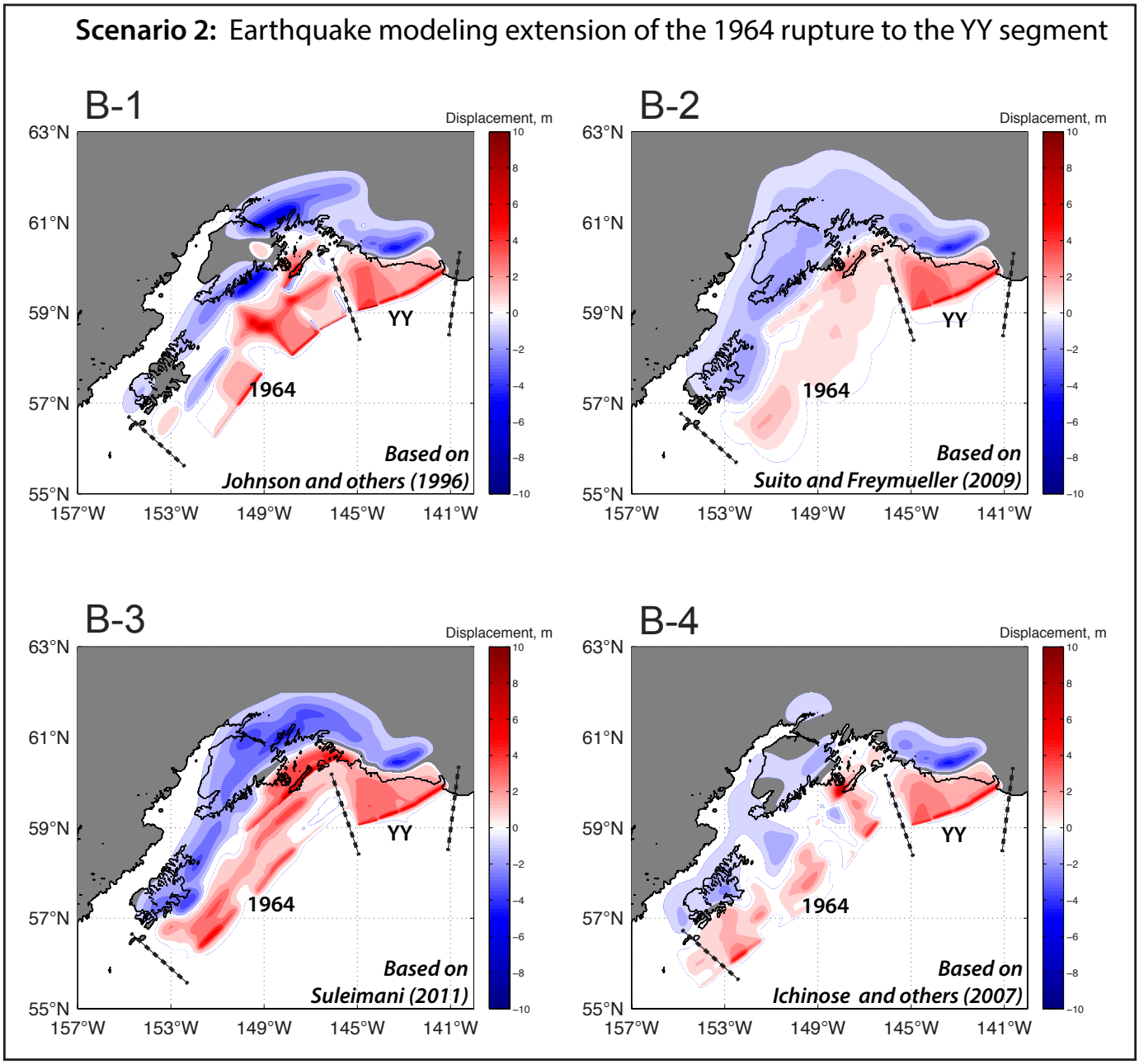

Figure 12, continued. (B) Ground-surface deformation for scenario 2. Blue shaded areas are associated with coseismic ground subsidence; areas of uplift are shown in red.

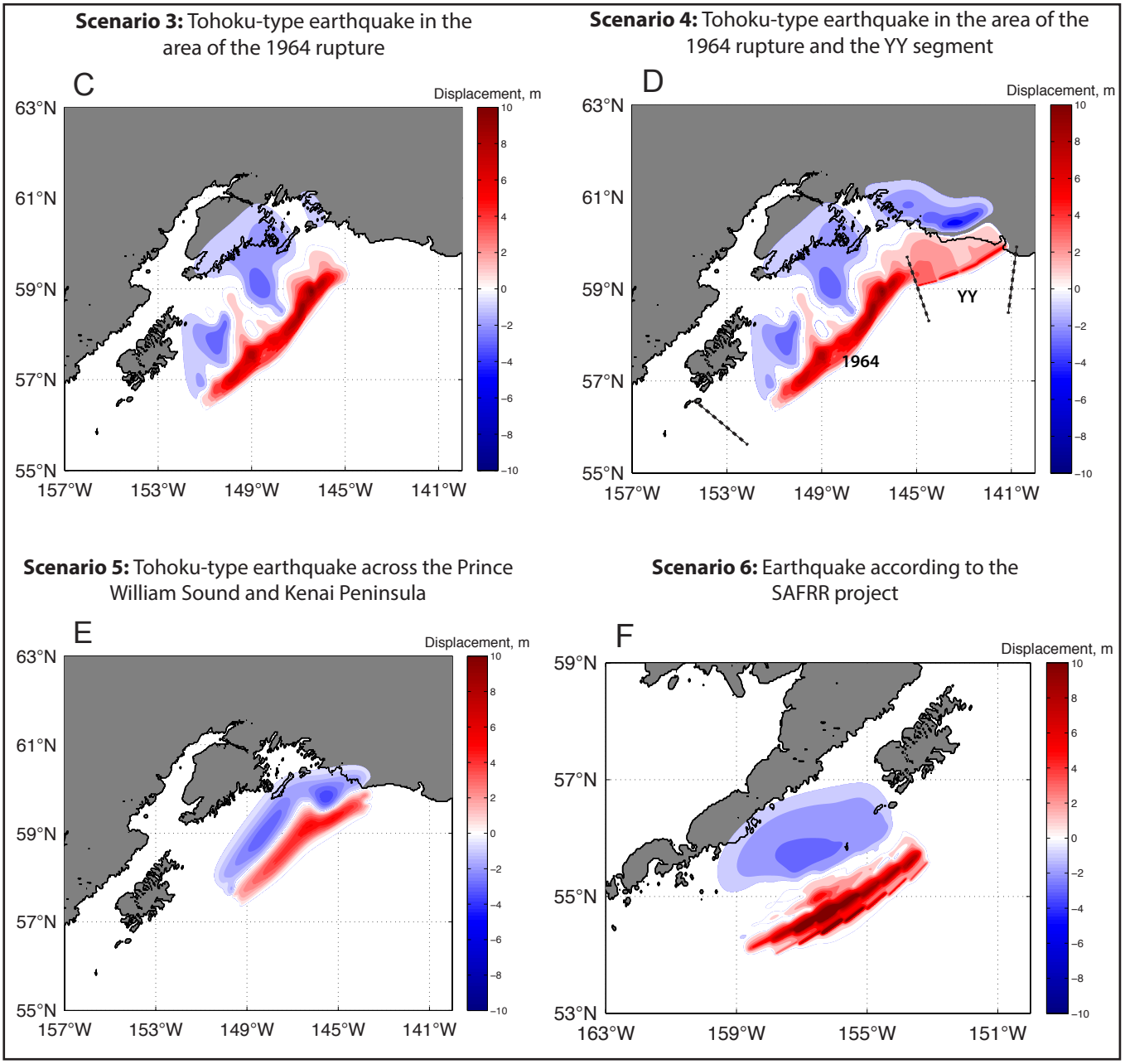

Figure 12, continued. (C, D, E, F) Ground-surface deformation for scenarios 3, 4, 5, and 6. Blue shaded areas are associated with coseismic ground subsidence; areas of uplift are shown in red.

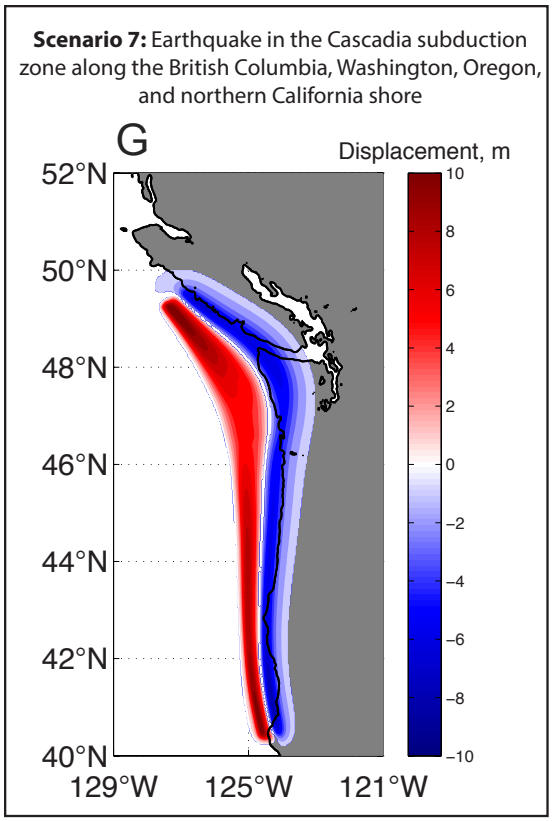

Figure 12, continued. (G) Ground-surface deformation for scenario 7. Blue shaded areas are associated with coseismic ground subsidence; areas of uplift are shown in red.

During the 1964 earthquake, submarine slides are known to have occurred in Seward, Valdez, and Whittier. For example, several failures initiated along the fjord walls at relatively shallow depths in Seward (Lemke, 1967; Haeussler and others, 2007), with a total volume of transported material estimated to be about 210 million m^3 (270 million yd^3) and a maximum slide thickness of about 60 m (200 ft). In Whittier, the maximum slide thickness along several transects in Passage Canal was similarly about 50–70 m (160–230 ft) (Kachadoorian, 1965, plate 3). Massive landslides also occurred in Valdez. Coulter and Migliaccio (1966, plate 2) estimated that approximately 75 million m^3 (98 million yd^3) of unconsolidated deposits were transferred from the Valdez waterfront into the bay, and the waterfront slide thickness was estimated at <100 m (<330 ft). Nicolsky and others (2013) revised the volume to be between 75 and 100 million m^3 (98 and 130 million yd^3). Therefore, we limit thickness of hypothetical slides next to creeks and rivers in Juneau to 50–70 m (160–230 ft), whereas the thickness of a hypothetical massive landslide in Taku Inlet could be as much as 100 m (330 ft).

From a tsunami modeling perspective, an initial landmass failure on a fjord wall has much greater potential to produce a tsunami than the fjord-bottom material disturbed by the slide. Therefore, we place landslides near the shore in shallow water to increase their wave generation potential. Because both slide volume and initial acceleration are important parameters for the tsunami generation potential, we consider a sensitivity study with respect to these values later in the report.

We identified six potential slide areas in the vicinity of Juneau—at the distal ends of deltas in Berners Bay, Eagle River, Mendenhall River (Fritz Cove), Sheep Creek, at the artificial fill site next to the Franklin Street Dock, and in Taku Inlet (fig. 3). Slide volume and maximum slide thickness for each landslide scenario are summarized in table 4.

Table 4. Hypothetical landslide scenarios used to model potential extent of inundation by landslide-generated tsunamis.

Scenario	Location of Underwater Slide	Maximum Slide Volume, Million m^3 (yd^3)	Maximum Slide Thickness, m (ft)
8	Head of Fritz Cove (FC slide; fig. 13a)	110 (144)	66 (220)
9	Offshore of Eagle River (ER slide; fig. 13b)	82 (107)	51 (170)
10	The head of Berners Bay (BB slide; fig. 13c)	79 (103)	40 (130)
11	Offshore of Sheep Creek (SC slide, fig. 13d)	9 (12)	31 (100)
12	South Franklin Street (SFS slide; fig. 13e)	0.8 (1.0)	16 (52)
13	Taku Inlet (TI slide, fig. 13f)	250 (330)	46 (150)

Scenario 8. An underwater slide at the head of Fritz Cove (FC slide; fig. 13A).

Fritz Cove is a bay between the mainland and Douglas Island, about 13 km (8.1 mi) from the city of Juneau. The Mendenhall River deposits glacial sediments at the northern shore of the cove. Industrial and residential areas, as well as the airport, are in close proximity to Fritz Cove. We estimate a maximum hypothetical slide volume of 110 million m^3 (144 million yd^3).

We perform a sensitivity study for this scenario by considering two additional cases. In the first case, the slide volume is decreased by about 50 percent, such that the volume is 51 million m^3 (68 million yd^3). In the second case, the slide density is increased by 50 percent in order to probe uncertainty in the potential inundation due to denser ground material.

Scenario 9. An underwater slide offshore of Eagle River (ER slide; fig. 13B).

The front of the Eagle River delta is another potential location for a submarine landslide. The river originates at Eagle Glacier in the Coast Mountains and flows into Favorite Channel 32 km (20 mi) north of the city. A state recreational area and two campgrounds are located at its mouth. We estimate a maximum hypothetical slide volume of 82 million m^3 (107 million yd^3).

Scenario 10. An underwater slide at the head of Berners Bay (BB slide; fig. 13C).

Berners Bay is 40 km (25 mi) north of Juneau and is an estuary fed by four glacial rivers including the Antler River, Berners River, and Lace River, as well as Cowee Creek. A submarine landslide could potentially occur along the delta front, and landslide-generated waves may threaten Echo Cove—a natural harbor with a boat ramp, parking lot, and several camping areas. We estimate a maximum hypothetical volume of 79 million m^3 (103 million yd^3).

Scenario 11. An underwater slide offshore of Sheep Creek (SC slide; fig. 13D).

Sheep Creek originates high in the Coast Mountains and empties into Gastineau Channel about 6 km (3.7 mi) south of Juneau. The mouth of Sheep Creek has a well-formed delta that represents another potential location for a submarine landslide. We estimate a maximum hypothetical slide volume of 9 million m^3 (12 million yd^3).

Scenario 12. An underwater slide at South Franklin Street (SFS slide; fig. 13E).

Discovery of gold in Juneau created mining opportunities around the community as well as mine tailings and an excess of artificial fill material. Some of the fill was used to level off areas along South Franklin Street and increase capacity of wharves on Gastineau Channel. In the event of significant ground shaking, it is possible that some of this material could slide into the channel. For example, during the 1994 event in Skagway, some of the dock area slid into the harbor (Cornforth and Lowell, 1996) and generated a tsunami. The 1994 Skagway slide was estimated to have a volume of 0.8 million m^3 (1 million yd^3), with the subaerial part accounting for 10 percent of the total slide volume (Rabinovich and others, 1999).

In this scenario, we consider a hypothetical failure along South Franklin Street. Similar to the Skagway slide, we assume the hypothetical slide has a volume of 0.8 million m^3 (1 million yd^3). As a part of the sensitivity study, we also consider a thinner slide at the same location with a total volume of 0.35 million m^3 (0.45 million yd^3).

Scenario 13. An underwater slide in Taku Inlet (TI slide; fig. 13F).

Strong ground shaking during the 1964 earthquake caused a massive submarine landslide at the head of Port Valdez (Coulter and Migliaccio, 1966). South of Juneau, the Taku River as well as other smaller glacier-fed streams drain to the ocean and carry unconsolidated sediment to the head of Taku Inlet. We hypothesize that sediments at the head of Taku Inlet, close to Taku Glacier, could fail and slide into the bottom of the inlet. Volume of the maximum hypothetical slide in Taku Inlet is assumed to be 250 million m^3 (327 million yd^3).

MODELING RESULTS

We performed numerical calculations for 13 scenarios that include both tectonically- and landslide-generated tsunamis. For tectonic tsunami scenarios, we modeled water dynamics in the grids listed in table 2 (grids marked with an asterisk[*] were used only in the sensitivity studies). For scenarios related to landslide-generated tsunamis, we simulated water dynamics and computed run-up only for the high-resolution grid. To visualize different effects of tectonic and landslide-generated waves in the vicinity of Juneau, we separately plot maximum wave heights for each tectonic scenario and the maximum composite wave heights for all landslide scenarios.

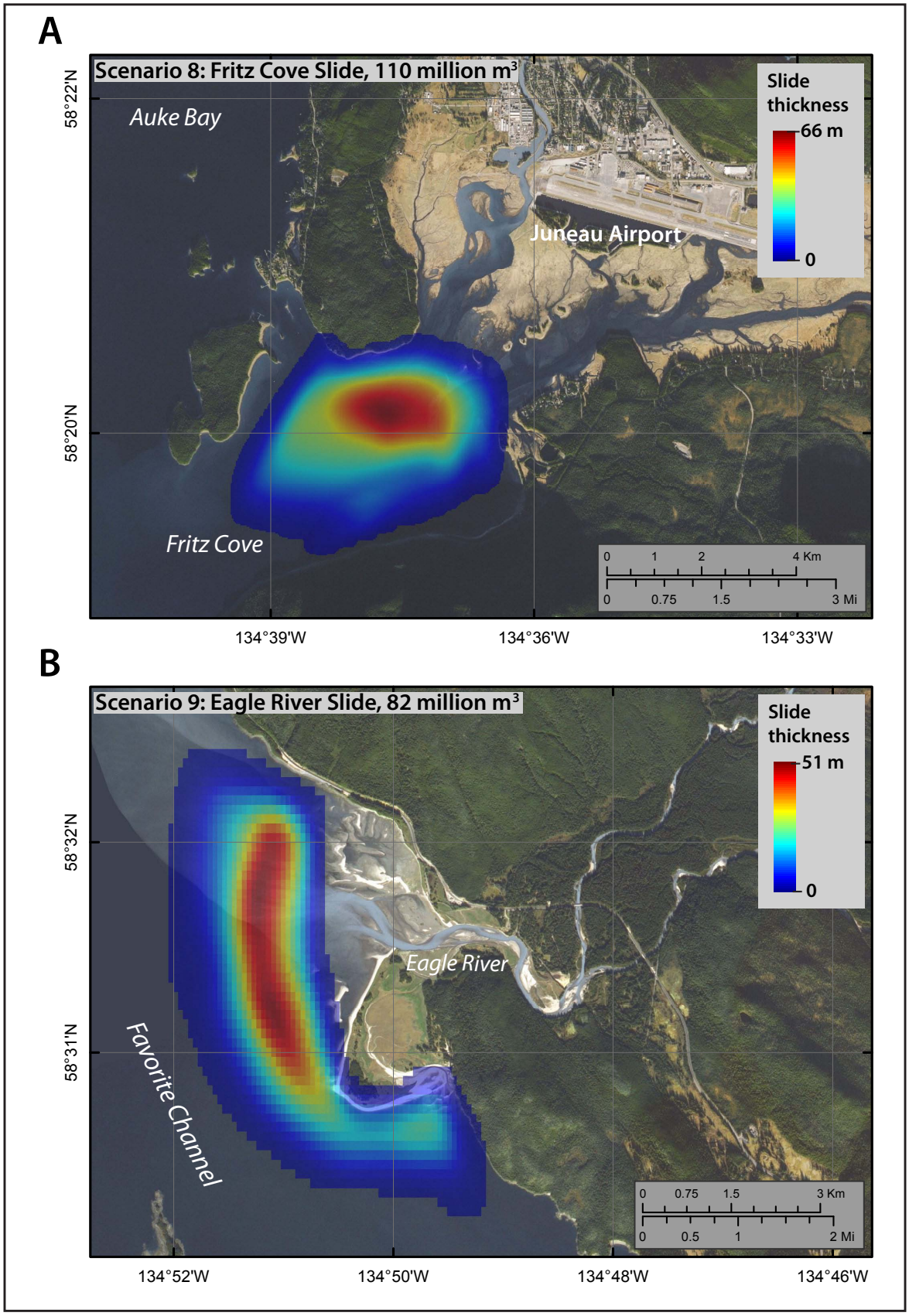

Figure 13. (A, B) Locations and initial landslide thicknesses for scenarios 8 and 9.

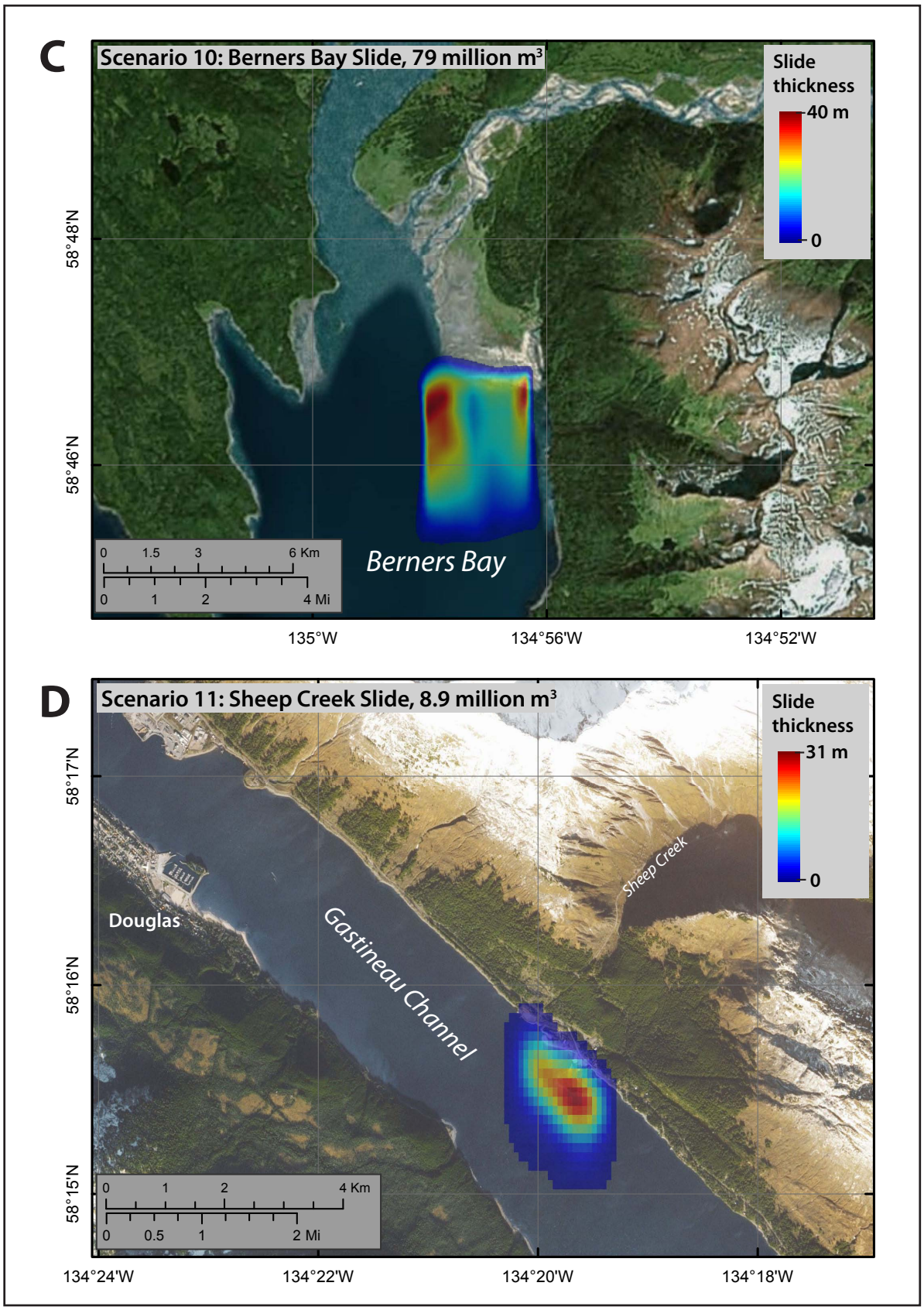

Figure 13, continued. (C, D) Locations and initial landslide thicknesses for scenarios 10 and 11.

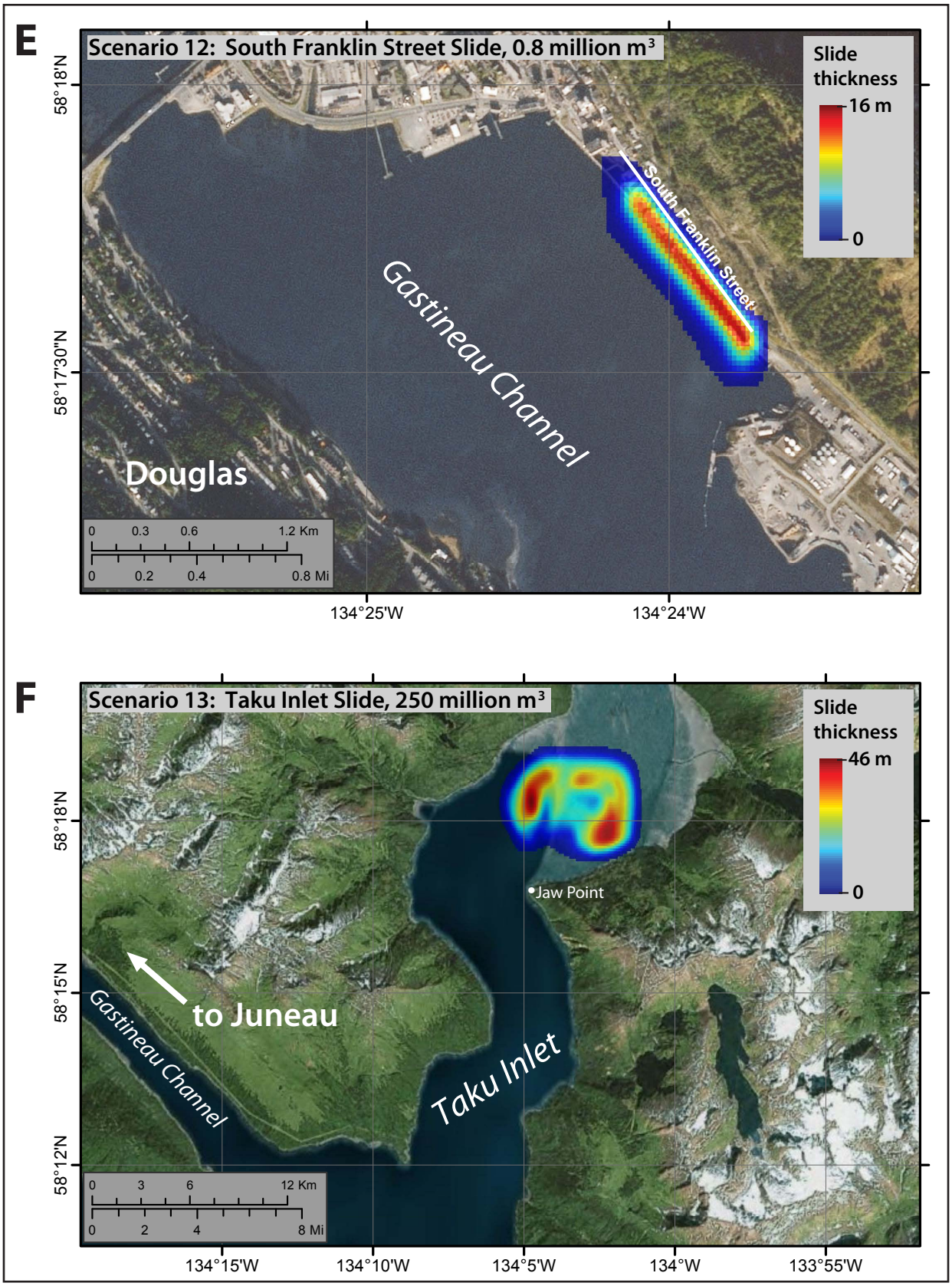

Figure 13, continued. (E, F) Locations and initial landslide thicknesses for scenarios 12 and 13.

Tectonic scenarios

Numerical experiments indicate that tsunamis generated by a potential earthquake rupture in the Gulf of Alaska region can reach Juneau in about 2.5 hours after the earthquake. However, the first wave might not be the highest wave, as observed during the 2011 Tohoku tsunami. To assess the potential impact of seven different tsunami scenarios, we simulate wave heights at several locations. Computer experiments reveal that scenarios 3, 4, and 7 produce the maximum wave heights near Juneau. These three scenarios describe Tohoku-type ruptures in the Gulf of Alaska region and a rupture of the Cascadia subduction zone, respectively. To illustrate the modeled tsunami dynamics according to these scenarios, we select three locations (shown in figures A1-A and A1-B): the tide gauge next to downtown Juneau (point 1); in Auke Bay—the major harbor area (point 8); and in Douglas Harbor (point 15). The associated computed water level dynamics are shown in figure 14. For all three locations, scenario 4—the multi-segment Tohoku-type earthquake in the Gulf of Alaska—results in the highest modeled wave.

Although scenario 4 is considered as a maximum geologically credible tsunami for the community, numerical modeling of the 2011 Tohoku tsunami demonstrated that the tsunami wave amplitude at Juneau could be underestimated by a factor of two even with good correlation between observed and modeled waveforms elsewhere in the same region (e.g., the first three waves at Elfin Cove and Skagway) (fig. 10C). As conjectured, the tsunami-tide interaction might be responsible for the underestimation of modeled tsunami height in Juneau. Thus, in order to produce a maximum potential estimate of inundation for the hypothetical tsunamis that compensates for the underestimation uncertainties, we generated two additional scenarios (scenarios 1D and 4D) as described below.

Because propagation of tsunamis in the open ocean and deep fjords is modeled as a linear process, we can double the modeled wave amplitude in Juneau simply by increasing the coseismic slip by a factor of two. We compensate for the underestimated maximum credible tsunami height in Juneau by doubling coseismic slip of scenario 4—the scenario which resulted in the highest wave in Juneau. We emphasize that this additional earthquake slip scenario is a numerical solution to the underestimation of tsunami height in Juneau (due to complex tsunami-tide interactions that are beyond the scope of current tsunami model capabilities). The effective (doubled) slip should not be considered from a geophysical point of view, but rather from a numerical modeling point of view. Thus, scenario 4D is a hypothetical tsunami that could be generated by a conjectural earthquake with double the coseismic slip of scenario 4 (the extension "D" stands for "doubled" to indicate the adjusted slip in the scenario).

The available geologic evidence suggests that repeated 1964-type events (scenario 1) may be a more realistic estimate of future earthquake displacements in the Gulf of Alaska. Thus, similar to scenario 4D, we generated scenario 1D to account for the potential underestimation of the modeling results due to tsunami-tide interactions. We first double the coseismic slip for all four models (fig. 12A) considered as part of scenario 1 and then model potential inundation in the community according to all of them. The modeling results indicate that the highest waves according to Johnson and others (1996) and Suleimani and others (2011) are almost the same and are the highest of the four models. The maximum modeled wave height in Juneau according to these two models is about 1.4 m (4.6 ft) at the tide gauge (fig. A1-A). This wave height correlates well with the observations of the 1964 tsunami in the city of about 1.2 m (3.9 ft) (Lander, 1996).

Figure 15 shows maximum tectonic tsunami heights above MHHW in the Juneau and Tongass Forest high-resolution grids for scenario 4D. The modeled inundation extents according to scenarios 1D and 4 are delineated as well. We note that scenario 4D is a numerical solution that accounts for large uncertainties as discussed earlier, and that

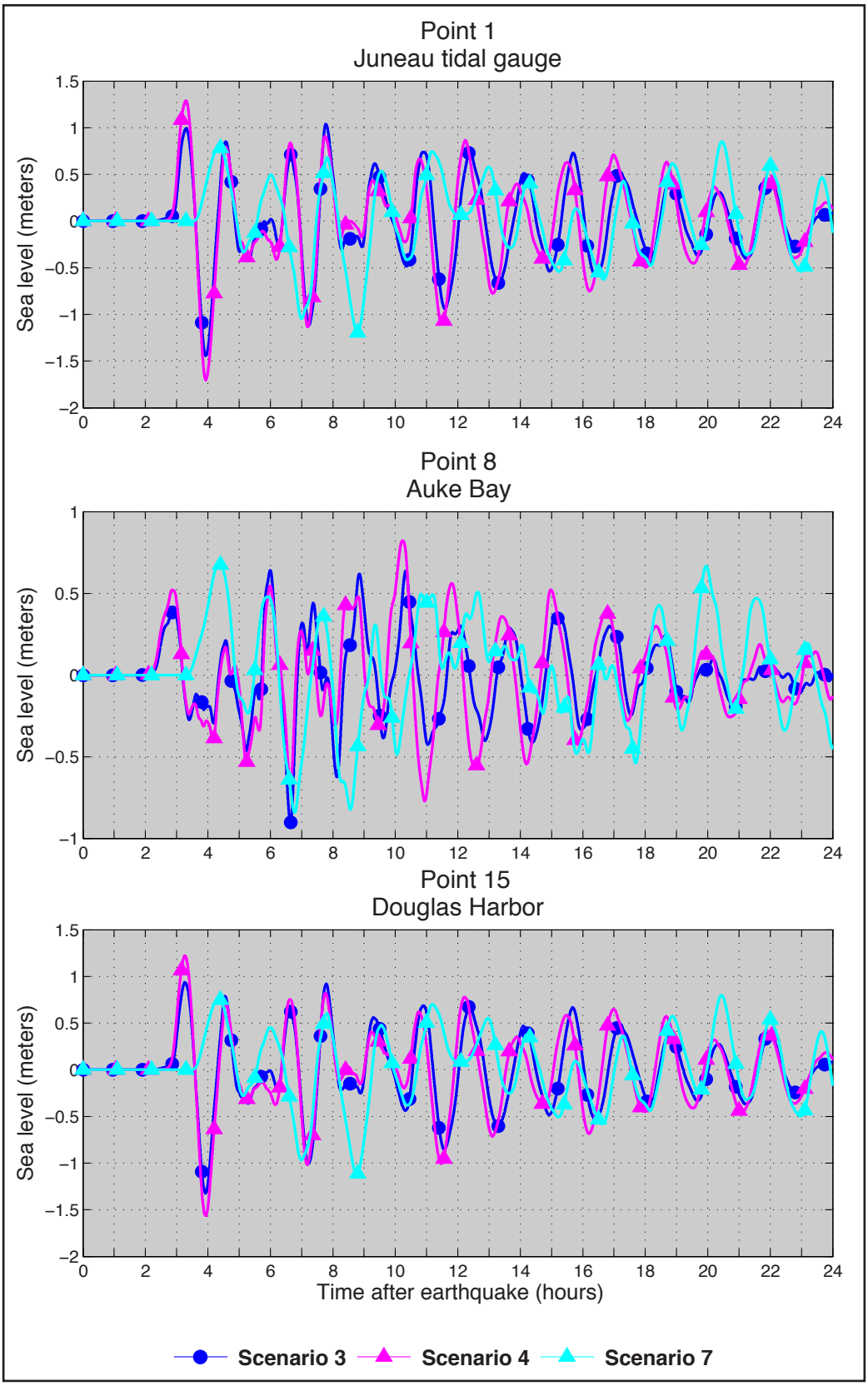

Figure 14. Simulated water-level dynamics at three locations in the vicinity of Juneau (locations on fig. A1) for selected scenarios that have the highest potential to produce the maximum wave near Juneau.

scenario 4 may be a more credible estimation of maximum inundation due to the tectonic tsunamis. Tsunami flow depth over dry land is another important indicator of potential damage. Maximum flow depth is calculated by subtracting the DEM elevations from maximum tsunami wave height over previously dry land. Thus, in addition to the computed maximum tsunami heights, figure 16 shows the flow depths in the area around Juneau airport above the mean shoreline (MSL) according to scenario 4D. Figure 16 also shows the calculated envelope of the inundation extents of the four models of a repeat of the 1964 event and the modeled extent of potential inundation according to scenario 4.

Modeling results suggest that scenario 4D produces waves with wavelengths of several kilometers (miles) that produce a relatively uniform distribution of maximum tsunami heights around the community. The highest waves, up to 3 m (10 ft), occur in the Gastineau Channel and around the Juneau airport (fig. 15A), while significantly smaller tsunami heights of 1.0–1.2 m (3.2–3.9 ft) are predicted in Favorite Channel and farther north in Lynn Canal (fig. 15B). There is a sharp change in tsunami heights in the middle of Gastineau Channel, where a bridge spans between downtown Juneau and Douglas Island. The flow here is constricted by the narrows and thus long waves that enter the channel from the southeast are partially reflected (fig. 15A). Only a part of the tsunami energy penetrates farther northwest through this narrows, resulting in decreased tsunami height in the upper Gastineau Channel. However, the waves are high enough to flood the area north of the airport. The low-lying areas south of the airport are flooded by smaller waves coming through Fritz Cove. North of Juneau, in the area of Favorite Channel and Lynn Canal (fig. 15B), maximum tsunami wave heights are on the order of 1.0 m (3.3 ft), except for the mouth of the Eagle River, where the waves amplify up to 1.5 m (4.9 ft).

Numerical results according to scenario 4 qualitatively resemble those according to scenario 4D, in that low-lying areas south of the airport are flooded, the highest waves occur in Gastineau Channel and around the Juneau airport, and there is a sharp change in the modeled tsunami heights in the middle of Gastineau Channel. Overall, the spatial distribution of the maximum tsunami wave heights according to scenario 4 has the same spatial pattern as that modeled according to scenario 4D (fig. 15). However, the maximum wave height for scenario 4 is about half the size in Gastineau Channel (1.2–1.5 m [3.9–4.9 ft]) and about 1.5 times smaller in Lynn Canal (0.6–0.9 m [2.0–3.0 ft]).

The hypothetical extent of inundation according to the 1964 event (scenario 1) is less than that for the Tohoku-type rupture in the Gulf of Alaska (scenario 4). However, a repeat of 1964 may be a more realistic future event. For scenario 1D, the maximum flow depth occurs at the eastern end of the airport, where it reaches 2.5 m (8.2 ft) above the MSL datum (fig. 16) and floods low-lying areas at the head of Gastineau Channel. The spatial extent of inundation and maximum wave heights according to scenario 1D are similar to those according to scenario 4. In all cases, the low-lying areas and tidal flats around the airport could be inundated.

Landslide scenarios

While tectonically-generated waves may not inundate the coast for hours after an earthquake, landslide-generated waves could hit low-lying areas while the ground is still shaking (Coulter and Migliaccio, 1966; Wilson and Tørum, 1968). Additionally, some landslide-generated waves can occur without an earthquake and therefore without any warning. In this section, we present our modeling approach to estimate the extent of inundation for the hypothetical landslide scenarios. We will discuss in detail scenario 8, which describes an underwater slide at the head of Fritz Cove. We model inundation for all other hypothetical landslide scenarios with the same approach but do not discuss these other scenarios in detail.

Hypothetical Fritz Cove slide

We assume that slide-prone unconsolidated deposits at the head of Fritz Cove (scenario 8) are

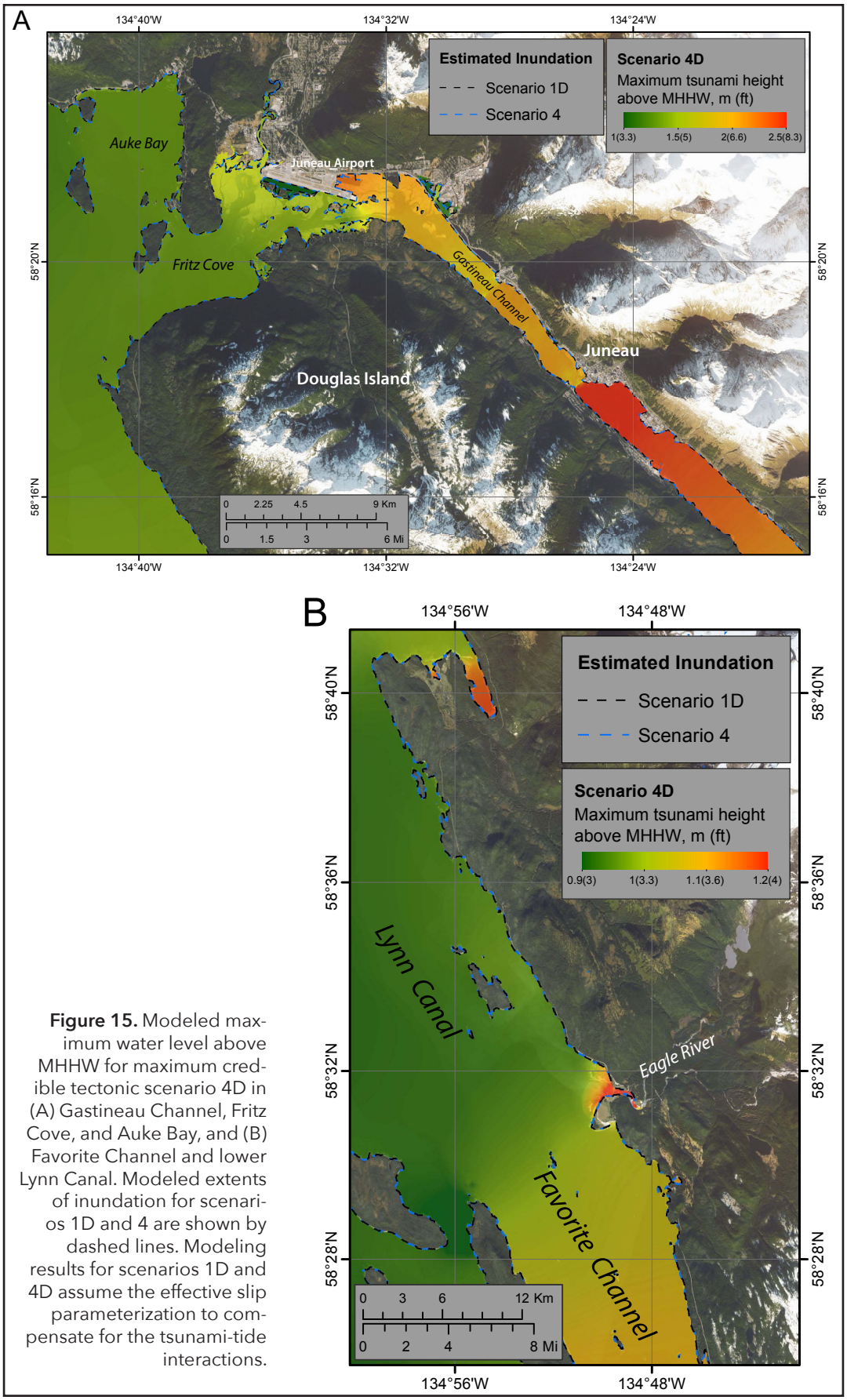

Figure 15. Modeled maximum water level above MHHW for maximum credible tectonic scenario 4D in (A) Gastineau Channel, Fritz Cove, and Auke Bay, and (B) Favorite Channel and lower Lynn Canal. Modeled extents of inundation for scenarios 1D and 4 are shown by dashed lines. Modeling results for scenarios 1D and 4D assume the effective slip parameterization to compensate for the tsunami-tide interactions.

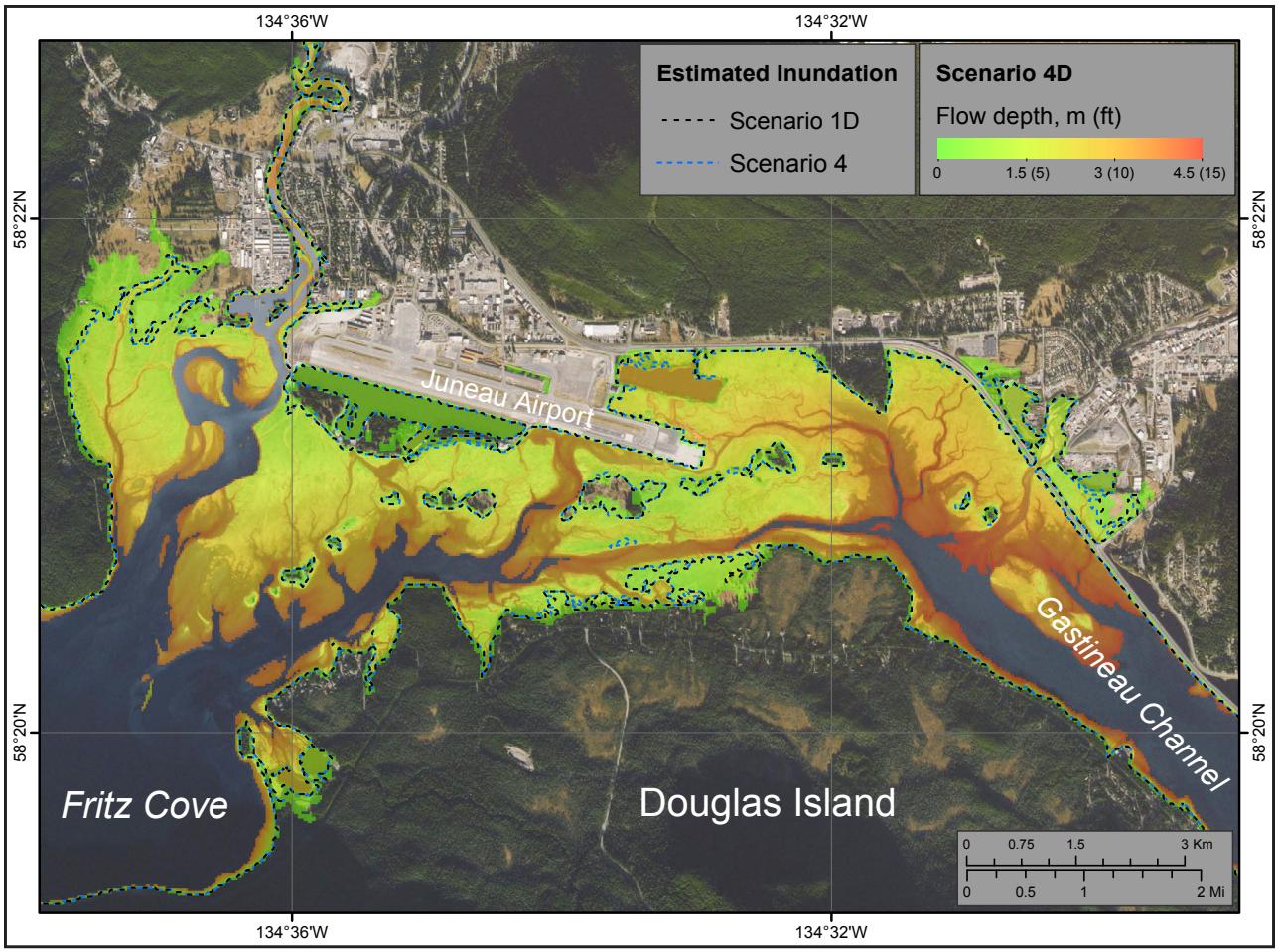

Figure 16. Modeled maximum water flow depth above MSL for maximum credible event (scenario 4D) and the modeled extent of the potential inundation for scenarios 1D and 4 near Juneau airport. The difference between MSL and MHHW datums in Juneau is 2.36 m (7.74 ft). Modeling results for scenarios 1D and 4D assume the effective slip parameterization to compensate for the tsunami-tide interactions.

initially at rest and ground shaking triggers the slide. The extent of the source area of the slide is shown in figure 17.

One of the parameters influencing slide dynamics is density of the slide mass. Unfortunately, there are no geotechnical data describing sediments in Fritz Cove. Shannon and Hilts (1973) conducted a subsurface geotechnical investigation of underwater slope materials that failed in a similar setting in Resurrection Bay near Seward, Alaska, during the 1964 earthquake, and found that the density of the slide material ranged from 2,000 to 2,110 kg/m^3 (125 to 132 lb/ft^3). Thus, as in the previous investigation of submarine slides in Port Valdez (Nicolsky and others, 2013), in this report we also assume a slide density of ρ = 2,000 kg/m^3 (125 lb/ft^3). Another parameter influencing slide dynamics is viscosity. Sensitivity studies by Rabinovich and others (2003) demonstrate that the influence of kinematic viscosity (μ_k) on tsunami heights is not significant. In this study we assume that the slide kinematic viscosity is such that μ_k/ρ = 0.1 m^2/s (1.1 ft^2/s) and the surface roughness coefficient n = 0.1 s/m$^{1/3}$ (0.15 s/ft$^{1/3}$) in the Manning formula for the bottom friction dissipation (Kirby and others, 2016). At the open (water) boundary of the numerical grid, we specify the radiation boundary condition for the water waves and then simulate the landslide-generated tsunamis using the NHWAVE model for 30 minutes. The modeled maximum tsunami flow depth over dry land (above the mean sea level [MSL] datum) is displayed in figure 17. Numerical simulations indicate that waves can reach the

northern coast of Auke Bay in 4–5 minutes and the western end of the airport runway in about 10 minutes. Also, during the numerical experiment, we recorded water-level dynamics in Fritz Cove at five locations (fig. 17). We later compare the water-level dynamics computed by the NHWAVE and FUNWAVE models at these five places.

Results of the numerical experiment with NHWAVE show that the hypothetical landslide-generated tsunami may produce 5 to 15 m-high (16 to 49 ft-high) waves along the southern shore of Fritz Cove and may cause significant inundation of wetlands in Gastineau Channel. As mentioned earlier, NHWAVE results are incorporated into the FUNWAVE model by specifying the initial conditions to be used in the FUNWAVE model. For scenario 8, we use the NHWAVE-computed water level and velocity at d = 3 and 4 minutes after the initial movement of the slide. The parameters calculated by NHWAVE at d = 3 and 4 minutes are then plugged into FUNWAVE and the model is run for the remainder of the 30 minute period.

The comparison between the NHWAVE- and FUNWAVE-computed water-level dynamics at the five locations is shown in figure 18. Despite some differences in the FUNWAVE results (for d=3 and 4 minutes), both modeling results—the amplitudes and periods of the waveforms—are in agreement. Moreover, the coupling is rather stable; changes in the NHWAVE water dynamics at two

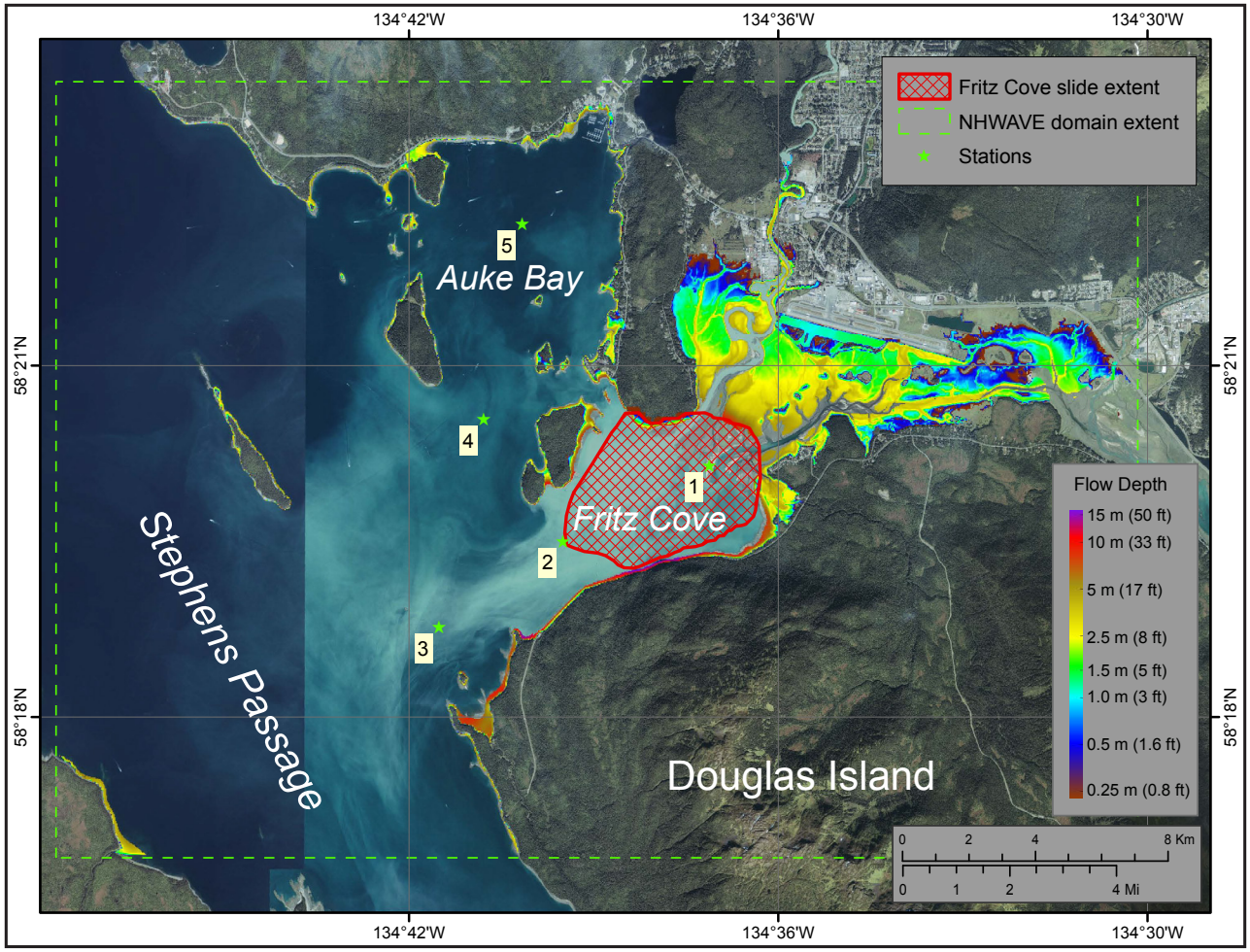

Figure 17. The NHWAVE-modeled maximum water flow depth above MSL according to scenario 8–the hypothetical Fritz Cove (FC) landslide. The extent of the FC slide source area is shown by the red cross-hatched polygon; the boundary of the computational grid used in the NHWAVE calculations is delineated by the dashed green line; locations of the five stations used to record the modeled water-level dynamics are marked by green stars.

close time moments do not result in large changes of the FUNWAVE dynamics. Therefore, we suggest that coupling the NHWAVE and FUNWAVE models is successful, both models simulate the tsunami after the transfer of data similarly, and most of the slide energy is adequately transferred to the water. The modeling results are only conjectures with respect to realistic landslide-generated tsunami dynamics. Recall that the initial landslide volume (fig. 13A) is defined by idealized failure surfaces and is modeled as viscous fluid; hence the difference between the FUNWAVE and NHWAVE modeling results could be accommodated by perturbations to the landslide geometry, the assumed slide rheology, or to other model parameters. Thus, from the physical point of view both FUNWAVE and NHWAVE results are equally plausible.

Figure 19A displays the modeled extent of inundation according to NHWAVE and two modeled extents of inundation according to FUNWAVE, related to d=3 and 4 minutes, respectively. All modeled run-up extents are generally in agreement with each other. However, FUNWAVE

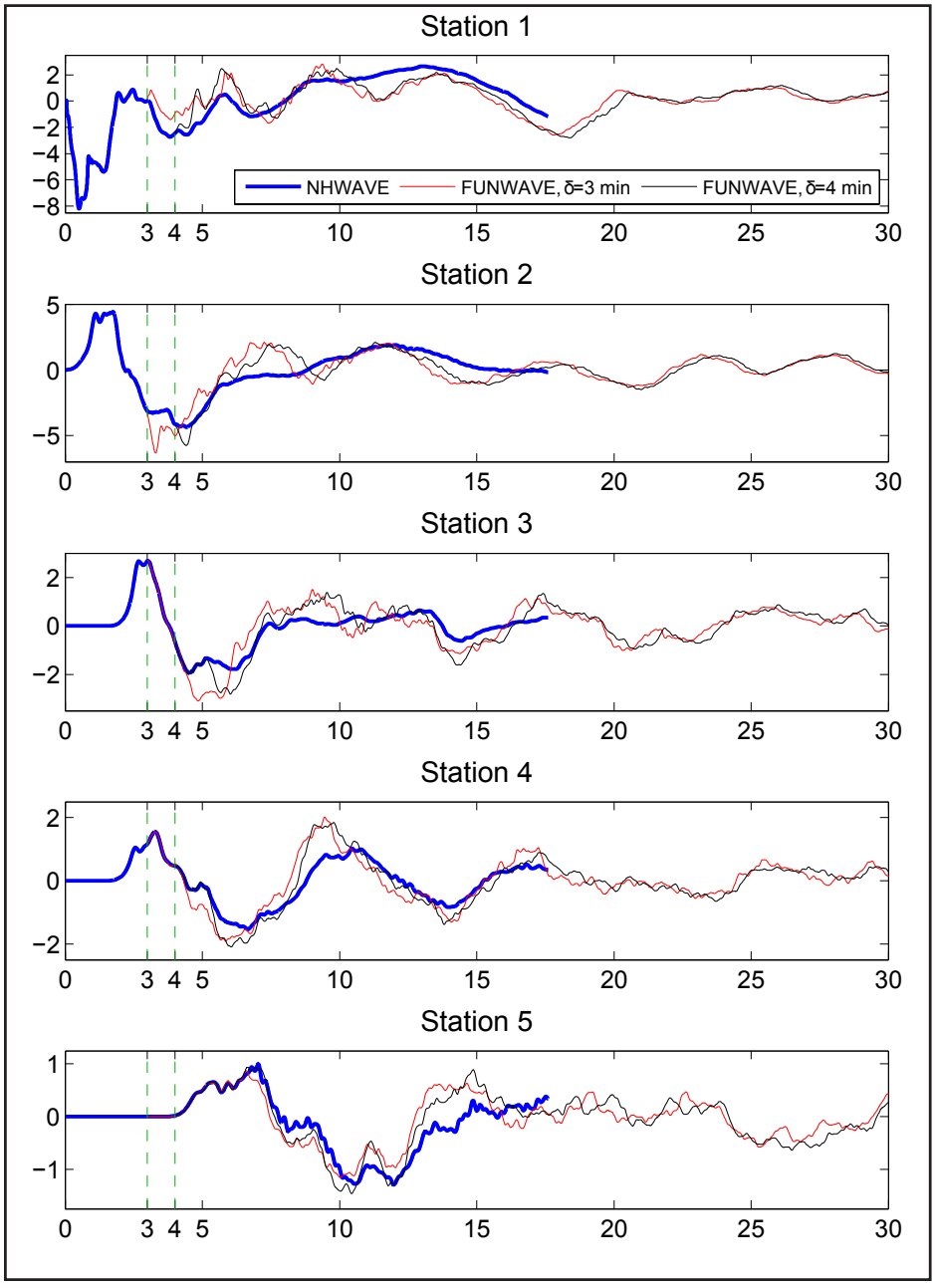

Figure 18. Comparison of scenario 8 NHWAVE- and FUNWAVE-computed water-level dynamics at five stations, shown by green stars in figure 17. The FUNWAVE model is initialized using NHWAVE outputs at δ=3 and 4 minutes after the landslide failure.

predicts large inundation at the west end of the airport runway and the other side of the Mendenhall River, along Crazy Horse Road. The observed differences in predicted inundation could be related to the coupling of NHWAVE and FUNWAVE models, distinctions in the physical formulation of the models, or to smaller wet/dry thresholds in the inundation modeling algorithm. The NHWAVE model was configured to use a 0.1 m (0.3 ft) threshold between wet and dry cells to optimize the computational time, while the same threshold for FUNWAVE was set to 0.01 m (0.03 ft). Despite some discrepancies, both models match the general pattern of inundation around Fritz Cove. Finally, by encompassing the maximum extent of flooding by NHWAVE and by two iterations of FUNWAVE, we develop an extent of the composite inundation (fig. 20A). The maximum flow depth over dry land (above the MSL datum) across all three models is also shown in figure 20A.

To probe sensitivity of inundation with respect to slide volume and density, we conduct two additional experiments. In one experiment the slide volume is reduced by about 50 percent to be 51 million m^3 (68 million yd^3); in the other experiment density is increased by 50 percent to be 3,000 kg/m^3 (187 lb/ft^3). All other model parameters are held constant. Recall that the density of the slide mass determines the initial acceleration of the slide, so a slide with higher density accelerates more quickly and can generate higher waves. The slide volume determines how much water is displaced by the sliding mass.

Using the same two-stage NHWAVE–FUNWAVE methodology, we model these additional two cases and plot the combined maximum extents of flooding in figure 19B. Results from the smaller slide volume are similar to the original scenario and show slightly subdued flooding of low lying areas and tidal flats between Douglas Island and the Juneau airport. The residential community on the northern side of Douglas Island is not inundated. Results from the higher density slide indicate significantly more flooding of the industrial and residential areas northwest of the airport. However, the slide density of 3,000 kg/m^3 (187 lb/ft^3) is high for the silt and sand carried by the Mendenhall River to Fritz Cove. Nevertheless, the results demonstrate sensitivity of run-up extent to adjustments in model parameters.

Other hypothetical slides

We use the same two-stage NHWAVE–FUNWAVE methodology to model the inundation extents for scenarios 9–13. Results for scenario 9 suggest the hypothetical Eagle River slide could generate 10–11 m (33–36 ft) waves at the mouth of the Eagle River and inundate the highway (fig. 20B), and the highway bridges across the Eagle River could be impacted by waves carrying debris. Also, waves propagating along the eastern shore of Favorite Channel could cause inundation of low-lying areas south and north of the Eagle River delta. The potential run-up on Shelter and Lincoln islands (not shown in fig. 20B) could reach 6–7 m (20–23 ft).

The Berners Bay slide (scenario 10) could generate a tsunami that floods low-lying areas in the estuary of Cowee Creek and the shores of Echo Cove, as shown in figure 20C. The maximum tsunami run-up is west of lower Cowee Creek and a landing strip on the northeastern side of the Cowee Creek mouth could also be inundated. Results suggest that the tsunami may propagate outside of Berners Bay into Lynn Canal and cause a local run-up in Bridget Cove and around Mab Island.

The Sheep Creek slide (scenario 11) could generate 6–7 m-high (20–23 ft) waves at the Sheep Creek delta. Results indicate that the tsunami reaches Thane Road (fig. 20D). On the opposite side of Gastineau Channel, the landslide-generated tsunami could cause 7–9 m (23–30 ft) waves. As in scenario 9, the modeled waves propagate along Gastineau Channel in both directions from the Sheep Creek delta and inundate low-lying areas along the channel. The wave can reach the Juneau downtown area in about 5 minutes.

The landslide-generated tsunami triggered along Franklin Street (scenario 12, fig. 21A) pro-

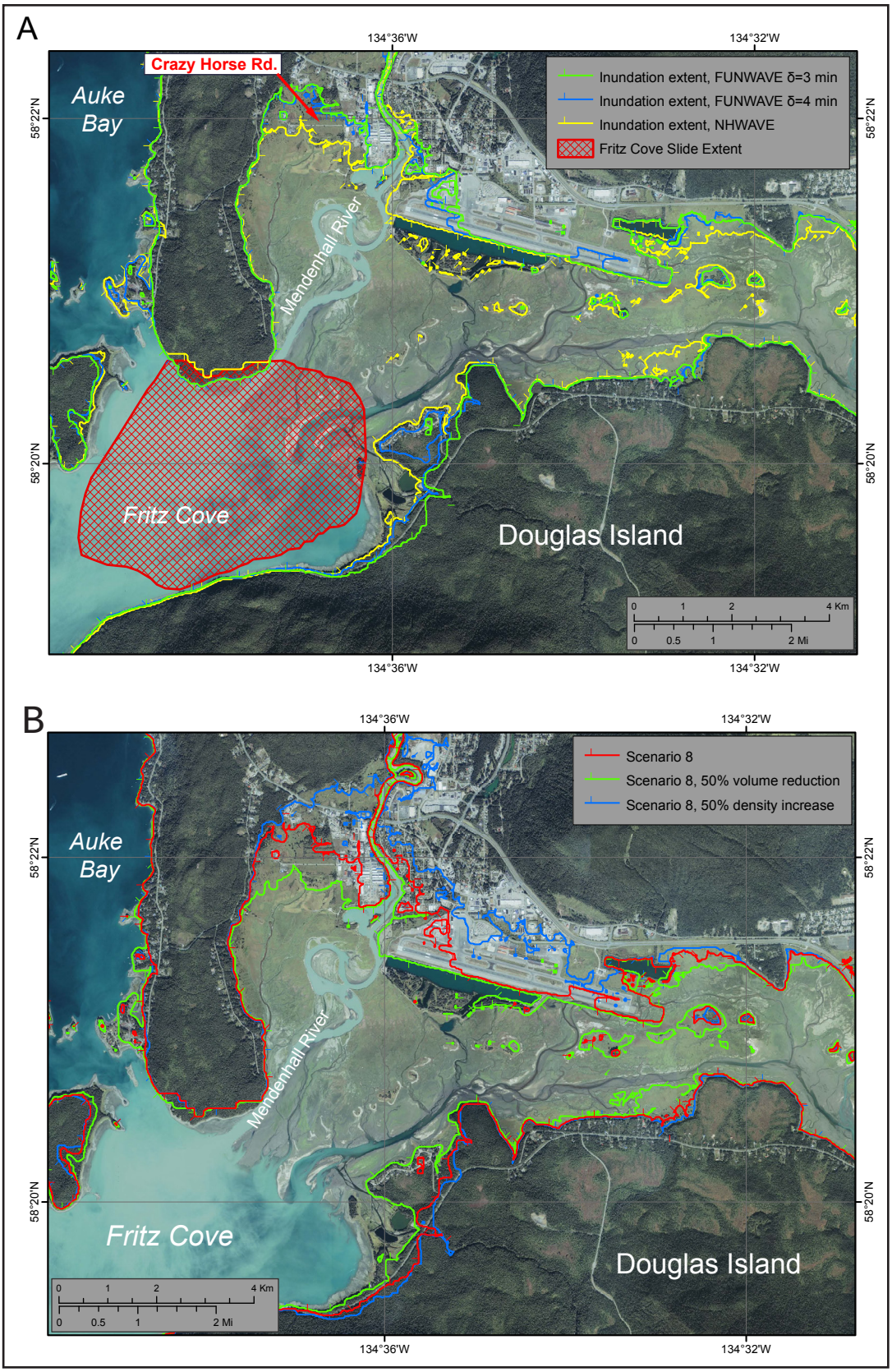

Figure 19. (A) Comparison of NHWAVE- and FUNWAVE-modeled inundation extents for scenario 8; extent of the FC slide source area is marked by the red cross-hatched polygon. (B) Sensitivity of the potential inundation with respect to volume and density of the FC slide.

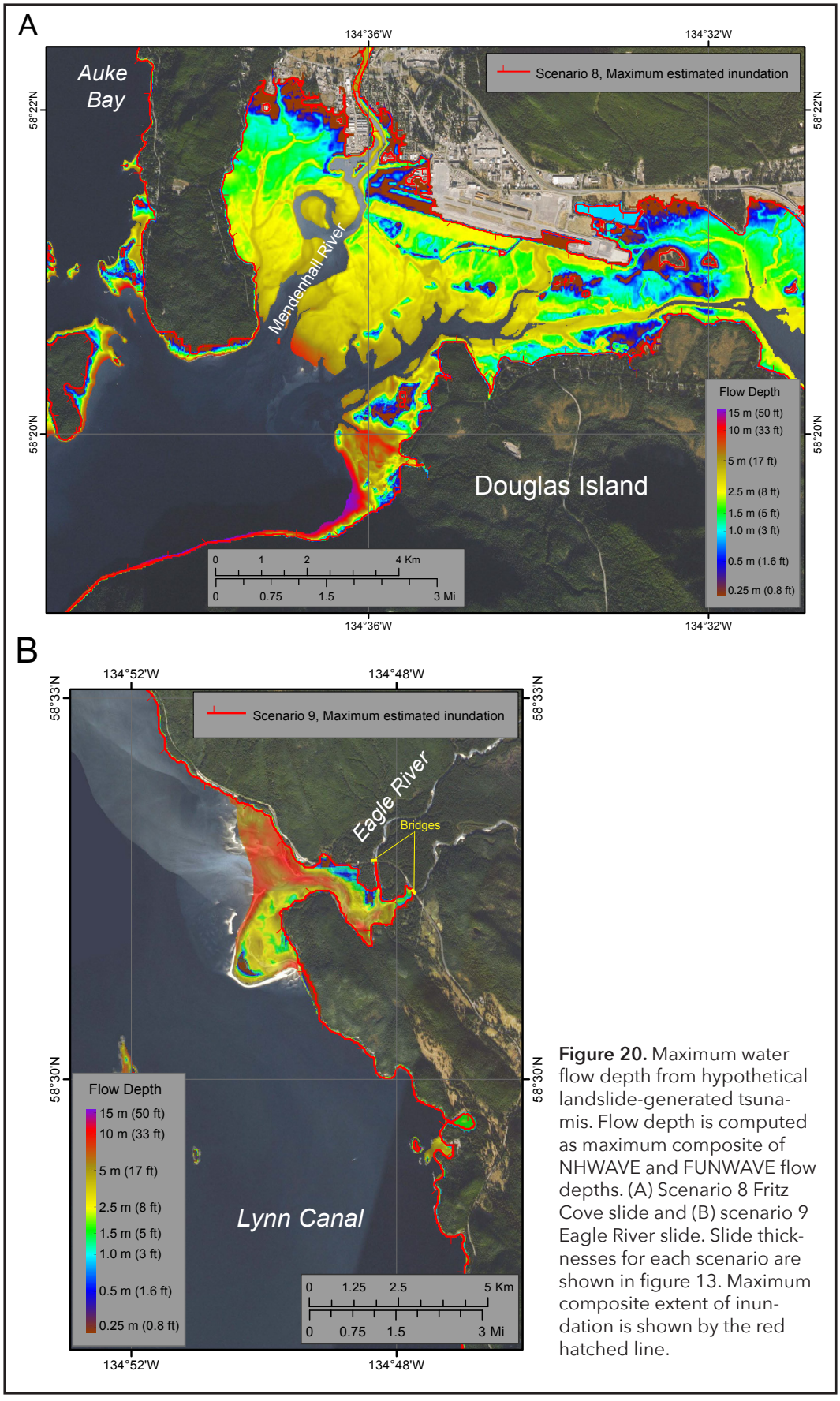

Figure 20. Maximum water flow depth from hypothetical landslide-generated tsunamis. Flow depth is computed as maximum composite of NHWAVE and FUNWAVE flow depths. (A) Scenario 8 Fritz Cove slide and (B) scenario 9 Eagle River slide. Slide thicknesses for each scenario are shown in figure 13. Maximum composite extent of inundation is shown by the red hatched line.

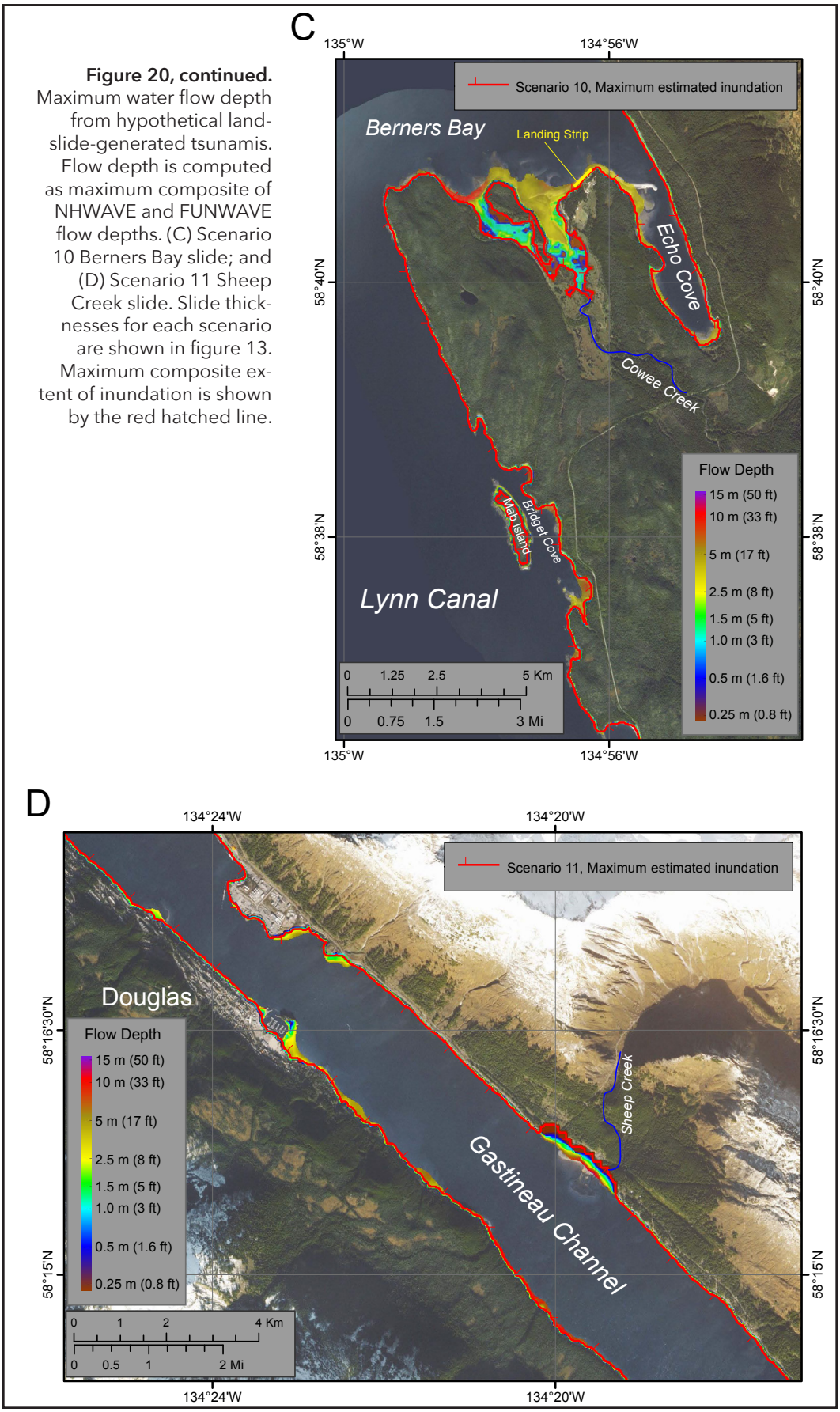

Figure 20, continued. Maximum water flow depth from hypothetical landslide-generated tsunamis. Flow depth is computed as maximum composite of NHWAVE and FUNWAVE flow depths. (C) Scenario 10 Berners Bay slide; and (D) Scenario 11 Sheep Creek slide. Slide thicknesses for each scenario are shown in figure 13. Maximum composite extent of inundation is shown by the red hatched line.

duces a 4–5 m (13–16 ft) run-up next to the dock facilities along the eastern coast of Gastineau Channel. On the opposite side of the channel, the waves can reach 3 m (10 ft) and inundate low-lying beach areas and the Lawson Creek delta. Waves reach the delta ~60 seconds after the landslide triggering. An experiment with a slide volume of 0.35 million m^3 (0.45 million yd^3)—i.e., decreased by 50 percent with respect to the original configuration—resulted in the same wave pattern and a reduction of wave height by 50 percent. This numerical experiment shows that wave height significantly depends on slide volume and that further research is necessary to constrain landslide sources in this region and hence to estimate the potential wave heights.

Finally, in scenario 13 (fig. 21B), we simulate a tsunami triggered by a landslide in Taku Inlet. The landslide generates waves up to 10–15 m (33–45 ft) near Jaw Point in Taku Inlet (fig. 13F). Waves emanating from the inlet mouth are significantly reduced in amplitude after multiple reflections inside the inlet. The tsunami within Gastineau Channel reaches a height of 2 m (6.6 ft) with local run-up reaching 3 m (10 ft) in some isolated areas. The first wave reaches downtown 6–7 minutes after the landslide.

Composite inundation

We use the predicted maximum flow depths from both hypothetical landslide-generated and tectonic tsunamis to develop a composite flow depth map for Juneau. Specifically, we superpose the maximum-credible tectonic tsunami (scenario 4D) with inundation from landslide-generated tsunamis (scenarios 8–13) by selecting the maximum computed flow depth values at each grid point. Map sheet 1 shows an overview of the maximum composite calculated extent of inundation and the maximum composite flow depths over dry land (above the MSL datum) around the city of Juneau, while map sheets 2–5 focus on specific areas to highlight details of the tsunami inundation zone for the community. We emphasize that scenario 4D is a numerical solution that accounts for large uncertainties by doubling the slip, as discussed earlier, and that scenario 4 may be a more credible estimation of maximum inundation due to tectonic tsunamis. Therefore, we also plot the potential inundation areas according to scenario 4 in map sheets 2–5.

We note that although the occurrence of the maximum credible event (scenario 4) is possible, the available geologic evidence suggests that repeated 1964-type events (scenario 1) may be a more realistic estimate of future earthquake displacements. Thus, on map sheets 2–5 we also plot the potential inundation areas according to scenario 1D. Recall that scenario 1D, similar to scenario 4D, accounts for the potential underestimation of the modeling results due to tsunami-tide interactions. We emphasize that the wave height according to scenario 1D correlates well with observations of the 1964 tsunami in Juneau. Thus scenario 1D may provide a more plausible estimate of future tsunami inundation.

Time series and other numerical results

We supplement the inundation maps with a time series of modeled water levels and velocity dynamics at certain locations around the town to provide emergency managers with the tools necessary to completely assess the tsunami hazard for Juneau. Emergency managers should consider the arrival time of the first wave, the maximum wave amplitude, and the duration of wave action during their evacuation planning. Appendix A contains time series plots of sea level and velocity at critical locations for scenarios 1D and 4D. Both of these scenarios were simulated with the doubled coseismic slip values as a part of the numerical modeling technique. We emphasize that although scenario 4D is thought to be the worst-case tectonic tsunami, scenario 1D might be a more realistic estimate of a future earthquake. Because there are four models considered as a repeat of the 1964 event, and because the Johnson and others (1996) model produces one of the highest waves across the four, we use modeling results according to Johnson and others (1996) to illustrate the impact of the repeat of the 1964 event on the community.

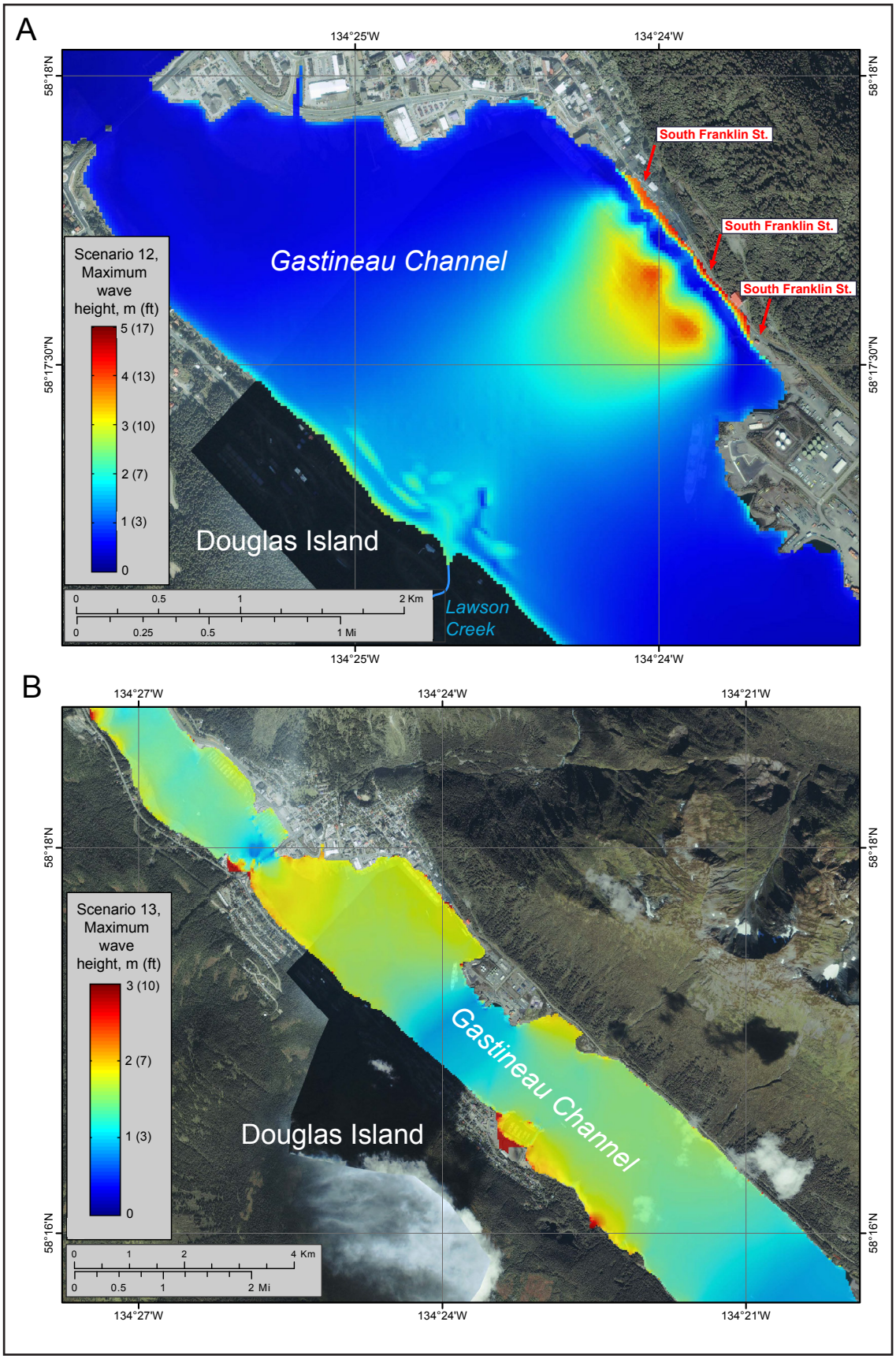

Figure 21. Maximum water level above MHHW for (A) scenario 12 slide along Franklin Street; and (B) scenario 13 slide in Taku Inlet.

For each location shown by a number in figures A-1A and A-1B, we plot the sea level and water velocity according to both scenarios in figure A-2. Zero time corresponds to the earthquake origin time. Elevations of onshore locations and values of ocean depth at offshore locations are based on the MHHW datum. Because velocity magnitude is calculated as water flux divided by water depth, the velocity value has large uncertainties in shallow water. In these plots, velocity is computed only where water depth is greater than 0.3 m (1 ft). For scenario 1D, the maximum water level is about 1.4 m (4.6 ft) and it occurs at the Juneau tide gauge (point 1; fig. A1-A) about 3 hours and 15 minutes after the earthquake (point 1; fig. A2). For scenario 4D, the highest wave is 2.5 m (8.2 ft), and it also occurs about 3 hours and 15 minutes after the earthquake. The strongest tsunami currents of 8 m/s (26 ft/s; 4 knots) occur under the bridge (point 2, fig. A1-A) about 4 hours after the earthquake. The tsunami activity continues for at least 24 hours, with 1.0 m (3.3 ft) waves arriving at the tide gauge, as seen in various plots in figure A2. For example, the highest wave in Auke Bay (point 8; fig. A1-1) occurs 10 hours after the earthquake (point 8; fig. A2). Maximum wave heights at the selected locations are listed in table A-1.

Because water-level oscillations can continue for more than a full day, even if the earthquake occurs during a low tide these oscillations will be affected by the subsequent rising tide. Low-lying areas that were not initially flooded may become inundated 24–48 hours after the earthquake. Another important factor in the tsunami hazard assessment for any coastal community is arrival time of the first wave. The time series plots demonstrate that the first wave arrives at Juneau about 3 hours after the earthquake. This means that the Juneau population would have up to 3 hours for evacuation if the tsunami is generated by a megathrust earthquake in the Gulf of Alaska. However, underwater landslides in the vicinity of Juneau are capable of producing waves that could reach onshore locations within minutes after slope failure. Plots of the modeled water level and velocity for these are shown in figure A-3. Because the landslide-generated tsunamis are simulated both with the NHWAVE and FUNWAVE models using the two-stage approach, we provide time series for both models. Recall that FUNWAVE was initialized at time d after the slide collapse, hence the FUNWAVE results are not available at the beginning of each scenario. Providing all modeling results permits an estimate of the uncertainty in wave height. Recognizing that arrival time is key to the vulnerability of a community to tsunami hazard has special significance for local emergency officials in evacuation planning.

SOURCES OF ERRORS AND UNCERTAINTIES

The hydrodynamic model used to calculate propagation and run-up of tectonic tsunamis is a nonlinear, flux-formulated, shallow-water model (Nicolsky and others, 2011b; Nicolsky, 2012) that passed the verification and validation tests required for numerical codes used to produce tsunami inundation maps (Synolakis and others, 2007; National Tsunami Hazard Mitigation Program [NTHMP], 2012). The NHWAVE and FUNWAVE models used to simulate inundation from landslide-generated tsunamis have also passed the same NHTMP verification and validation tests (Tehranirad and others, 2012). Most of the errors/uncertainties in the numerical predictions originate from the tsunami sources used in the numerical models. Due to insufficient data on locations and volumes of hypothetical subaerial landslides, we do not model tsunamis generated by this type of landslide even though they present a significant hazard to Alaska coastal communities.

The spatial resolution of the grid used to calculate tsunami inundation at Juneau is ~16 m (52.5 ft) and satisfies NOAA minimum recommended requirements for computation of tsunami inundation (National Tsunami Hazard Mitigation Program [NTHMP], 2010). We stress that this resolution is high enough to describe major relief features; however, small topographic features, buildings, and other facilities cannot be resolved

accurately by the existing model. We also note that uncertainty in grid cell elevation/depth propagates into the modeling results and eventually contributes to a horizontal uncertainty in the location of the inundation line. However, no established practices exist to directly propagate the DEM uncertainty into the uncertainty of the inundation line (Hare and others, 2011). In addition to the uncertainty related to the grid cell elevation/depth, uncertainties in the tsunami source (earthquake and landslide geometry) are the largest sources of error in tsunami modeling efforts. The direction of the incoming waves, their amplitudes, and times of arrival are primarily determined by displacements of the ocean surface in the source area. Therefore, the inundation modeling results for local landslide sources are especially sensitive to the slide volume, its initial position, and acceleration. The modeling process is highly sensitive to errors when the complexity of the source function is combined with its proximity to the coastal zone. Another important source of uncertainty related to the under-prediction of the tsunami observations near Juneau is attributed to the tsunami-tide interactions, but other physical mechanisms could also play a role. The current practice is to create some additional buffer area around the inundation line to use for hazard mitigation and decisions related to tsunami evacuation.

SUMMARY

We present the results of numerical modeling of tectonic and submarine landslide-generated tsunami waves for the town of Juneau in southeastern Alaska. Each of the scenarios considered is geologically reasonable and presents potential hazards to the community. The available geologic evidence indicates that repeated 1964-type events provide the most realistic estimate of future earthquake displacements and associated tsunami generation and inundation. However, a Tohoku-type event is possible. Scenario 4, based on a Tohoku-type source mechanism, is considered the worst-case tectonic tsunami scenario based on credible geophysical and geological information. Considering potential underestimation of modeled tsunami wave heights due to tsunami-tide interactions that are not well understood, scenario 4D is also possible, while a series of landslide-generated tsunamis could result in short arrival time and high tsunami wave amplitudes. A submarine landslide in Fritz Cove could present a local tsunami hazard for Juneau.

The maps that are part of this report have been completed using the best information available and are believed to be accurate; however, their preparation required many assumptions. We have considered several tsunami scenarios and have provided an estimate of maximum credible tsunami inundation. Actual conditions during a tsunami event may vary from those considered, so the report's accuracy cannot be guaranteed. The limits of inundation shown should only be used as a guideline for emergency planning and response action. Actual areas inundated will depend on specifics of earth deformations, on-land construction, and tide level, and may differ from areas shown on the maps. The information on these maps is intended to assist state and local agencies in planning for emergency evacuation and tsunami response actions in the event of a major tsunamigenic earthquake. These results are not intended for land-use regulation or building-code development.

ACKNOWLEDGMENTS

This report was funded by Award NA15NWS4670027 by a National Tsunami Hazard Mitigation Program grant to Alaska Division of Homeland Security and Emergency Management and University of Alaska Fairbanks from the Department of Commerce/National Oceanic and Atmospheric Administration. This does not constitute an endorsement by NOAA. Numerical calculations for this work were supported by High Performance Computing (HPC) resources at the Research Computing Systems unit at the Geophysical Institute, University of Alaska Fairbanks. We are grateful to Kenneth Macpherson for his help with the RTK GPS survey in Juneau. Thoughtful reviews by Finn Løvholt (Norwegian Geotechnical Institute, Oslo) and James Begét (University of Alaska Fairbanks) improved the report.

REFERENCES

Alaska Department of Commerce, Community, and Economic Development, Division of Community and Regional Affairs (DCCED/DCRA), 2013, Community Database Online, Yakutat Community Profile: State of Alaska DCCED/DCRA website, last viewed 1/6/2017. https://www.commerce.alaska.gov/dcra/DCRAExternal/community/Details/1a737990-4076-4de6-b8ef-4ca63da201dd

Alaska Department of Labor and Workforce Development, 2016, Alaska population overview: 2015 estimates: State of Alaska Department of Labor and Workforce Development, 140 p. http://live.laborstats.alaska.gov/pop/estimates/pub/popover.pdf

Ataie-Ashtiani, B., and Najafi-Jilani, A., 2008, Laboratory investigations on impulsive waves caused by underwater landslide: Coastal Engineering, v. 55, no. 12, p. 989–1004 http://doi.org/10.1016/j.coastaleng.2008.03.003

Caldwell, R.J., Taylor, L.A., Eakins, B.W., Carignan, K.S., and Collins, S.V., 2012, Digital elevation models of Juneau and Southeast Alaska—Procedures, data sources and analysis: National Geophysical Data Center, NOAA Technical Memorandum NESDIS NGDC, p. 53, 66.

City and Borough of Juneau, 2009, All-hazards mitigation plan: City and Borough of Juneau, 152 p. www.juneau.org/emergency/documents/All-Hazards%20Mitigation%20Plan.pdf

Cornforth, D. H., and Lowell, J. A., 1996, The 1994 submarine slope failure at Skagway, Alaska, *in* Senneset, K., eds., Landslides: Balkema, Rotterdam, p. 527–532.

Coulter, H.W., and Migliaccio, R.R., 1966, Effects of the earthquake of March 27, 1964 at Valdez, Alaska: U.S. Geological Survey Professional Paper, 542-C, 36 p. https://pubs.usgs.gov/pp/0542c/

Courant, R., Friedrichs, K., and Lewy, H., 1928, Über die partiellen Differenzengleichungen der mathematischen Physik: Mathematische Annalen (in German), v. 100, no. 1, p. 32–74. http://doi.org/10.1007/BF01448839

Doser, D.I., and Lomas, R., 2000, The transition from strikeslip to oblique subduction in southeastern Alaska from seismological studies: Tectonophysics, v. 316, p. 45–65.

Dunbar, P.K., and Weaver, C.S., 2008, U.S. states and territories national tsunami hazard assessment—Historical record and sources for waves: National Oceanic and Atmospheric Administration and U.S. Geological Survey, Technical Report, 59 p. http://nthmp.tsunami.gov/documents/Tsunami_Assessment_Final.pdf

Enet, François, and Grilli, S. T., 2007, Experimental study of tsunami generation by three-dimensional rigid underwater landslides: Journal of Waterway, Port, Coastal and Ocean Engineering, v. 133, no. 6, p. 442–454. http://doi.org/10.1061/(ASCE)0733-950X(2007)133:6(442)#sthash.ORABCSar.dpuf

Fine, I.V., Rabinovich, A.B., Kulikov, E.A., Thomson, R.E.,and Bornhold, B.D., 1998, Numerical modeling of landslide-generated tsunamis with application to the Skagway Harbor tsunami of November 3, 1994, *in* Proceedings of International Conference on Tsunamis: Paris, p. 211–223.

Geist, E.L., Jakob, Matthias, Wieczorek, G.F., and Dartnell, Peter, 2003, Preliminary hydrodynamic analysis of landslide-generated waves in Tidal Inlet, Glacier Bay National Park, Alaska: U.S. Geological Survey Open-File Report 2003–411, 20 p.

Geist, E., and Lynett, P., 2014, Source processes for the probabilistic assessment of tsunami hazards: Oceanography, v. 27, no. 2, p. 86–93. http://doi.org/10.5670/oceanog.2014.43

Geist, E.L., and Parsons, T., 2006, Probabilistic analysis of tsunami hazards: Natural Hazards. v. 37, no. 3, p. 277–314. http://dx.doi.org/10.1007/s11069-005-4646-z

George, D.L., and Iverson, R.M., 2014, A depth-averaged debris-flow model that includes the effects of evolving dilatancy. II. Numerical predictions and experimental tests: Proceedings of the Royal Society A, v. 470, no. 2170. p. 20,130,820–20,130,820. http://dx.doi.org/10.1098/rspa.2013.0820

Grilli, S.T., and Watts, P., 1999, Modeling of waves generated by a moving submerged body. Applications to underwater landslides: Engineering analysis with bound elements, v. 23, p. 645–656.

Grilli, S.T., O'Reilly, C., and Tajalli Bakhsh, T., 2013, Modeling of SMF tsunami generation and regional impact along the upper U.S. East Coast: Center for Applied Coastal Research, University of Delaware, Research Report No. CACR-13-05. http://www1.udel.edu/kirby/nthmp/reports/grilli-etal-cacr-13-05.pdf

Grilli, S.T., Shelby, Mike, Kimmoun, Olivier, Dupont, G., Nicolsky, D.J., Ma, Gangfeng, Kirby, J.T., and Shi, Fengyan, 2016, Modeling coastal tsunami hazard from submarine mass failures: Effect of slide rheology, experimental validation, and case studies off the U.S. East coast: Natural Hazards, p. 1–39. http://doi.org/10.1007/s11069-016-2692-3

Haeussler, P.J., Lee, H.J., Ryan, H.F., Labay, K.A., Kayen, R.E., Hampton, M.A., and Suleimani, E.N., 2007, Submarine slope failures near Seward, Alaska, during the M9.2 1964 earthquake, *in* Lykousis, Vasilios, Sakellariou, Dimitris, and Locat, Jacques, eds., Submarine mass movements and their consequences: Springer, p. 269–278.

Hamilton, Sarah, and Shennan, Ian, 2005, Late Holocene great earthquakes and relative sea-level change at Kenai, southern Alaska: Journal of Quaternary Science, v. 20, no. 2, p. 95–111.

Hampton, M.A., Lemke, R.W., and Coulter, H.W., 2002, Submarine landslides that had a significant impact on man and his activities, Seward and Valdez, Alaska, *in* Schwab, W.C., Lee, H.J., and Twichell, D.C., eds., Submarine Landslides—Selected Studies in the U.S. Exclusive Economic Zone: U.S. Geological Survey Bulletin 2002, p. 123–134. https://pubs.er.usgs.gov/publication/b2002

Harbitz, C.B., 1992, Model simulations of tsunamis generated by the Storegga Slides: Marine Geology, v. 105, p. 1–21.

Hare, Rob, Eakins, Barry, Amante, Chris, and Taylor, L.A., 2011, Modeling bathymetric uncertainty: US HYDRO 2011 conference, Tampa, FL, April 25–28, 2011, Proceedings. http://ushydro.thsoa.org/us11papers.htm

Hayes, G.P., Wald, D.J., and Johnson, R.L., 2012, Slab1.0: A three-dimensional model of global subduction zone geometries: Journal of Geophysical Research, v. 117, no. B01, p. 302. http://doi.org/10.1029/2011JB008524

Horrillo, J., Wood, A., Kim, G.B., Parambath, A., 2013, A simplified 3-D Navier–Stokes numerical model for landslide-tsunami: Application to the Gulf of Mexico: Journal of Geophysical Research, v. 118, no. 12, p. 6,934–6,950. http://doi.org/10.1002/2012JC008689

Ichinose, Gene, Somerville, Paul, Thio, H.K., Graves, Robert, and O'Connell, Dan, 2007, Rupture process of the 1964 Prince William Sound, Alaska, earthquake from the combined inversion of seismic, tsunami, and geodetic data: Journal of Geophysical Research, v. 112, no. B07, p. 2,156–2,202. http://doi.org/10.1029/2006JB004728

Ito, Yoshihiro, Tsuji, Takeshi, Osada, Yukihito, Kido, Moyoyuki, Inazu, Daisuke, Hayashi, Yutaka, Tsushima, Hiroaki, Hino, Ryota, and Fujimoto, Hiromi, 2011, Frontal wedge deformation near the source region of the 2011 Tohoku-Oki earthquake: Geophysical Research Letters, v. 38, no. 7. http://doi.org/10.1029/2011GL048355

Iverson, R.M., Denlinger, R.P., 2001, Flow of variably fluidized granular masses across three-dimensional terrain 1. Coulomb mixture theory: Journal of Geophysical Research, v. 106, p. 537–552.

Jiang, Lin, and LeBlond, P.H., 1992, The coupling of a submarine slide and the surface waves which it generates: Journal of Geophysical Research, v. 97, no. C8, p. 12,731–12,744. http://doi.org/10.1029/92JC00912

Jiang, Lin, and Leblond, P.H., 1993, Numerical modeling of an underwater Bingham plastic mudslide and the waves which it generates: Journal of Geophysical Research, v. 98, no. C6, p. 10,303–10,317. http://doi.org/10.1029/93JC00393

Johnson, J.M., Satake, Kenji, Holdahl, S.R., and Sauber, Jeanne, 1996, The 1964 Prince William Sound earthquake—Joint inversion of tsunami waveforms and geodetic data: Journal of Geophysical Research, v. 101, no. B1, p. 523–532. http://doi.org/10.1029/95JB02806

Kachadoorian, Reuben, 1965, Effects of the earthquake of March 27, 1964, at Whittier, Alaska: U.S. Geological Survey Professional Paper 542-B, p. B1–B21, 3 sheets, scale 1:4,800.

Kanamori, Hiroo, 1970, The Alaska earthquake of 1964—Radiation of long-period surface waves and source mechanism: Journal of Geophysical Research, v. 75, no. 26, p. 5,029–5,040. http://doi.org/10.1029/JB075i026p05029

Kirby, J.T., Shi, Fengyan, Nicolsky, D.J., and Misra, Shubhra, 2016, The 27 April 1975 Kitimat, British Columbia submarine landslide tsunami—A comparison of modeling approaches: Landslides, v. 13, no. 6, p. 1,421–1,434. http://doi.org/10.1007/s10346-016-0682-x

Kirby, J.T., Wei, Ge, Chen, Qin, Kennedy, A.B., and Dalrymple, R.A., 1998, FUNWAVE 1.0, Fully nonlinear Boussinesq wave model documentation and user's manual: Center for Applied Coastal Research, Department of Civil and Environmental Engineering, University of Delaware, Research Report CACR-98-06, 80 p. https://www1.udel.edu/kirby/programs/nearcom/documents/funwave2d.pdf

Kirby, Stephen, Scholl, David, von Huene, Roland, and Wells, Ray, 2013, Alaska earthquake source for the SAFRR tsunami scenario, chapter B, *in* Ross, S.L., and Jones, L.M., eds., The SAFRR (Science Application for Risk Reduction) Tsunami Scenario: U.S. Geological Survey Open-File Report 2013–1170, 40 p. http://pubs.usgs.gov/of/2013/1170/b/

Kowalik, Zygmunt, and Proshutinsky, Andrey, 2010, Tsunami–tide interactions—A Cook Inlet case study: Continental Shelf Research, v. 30, no. 6, p. 633–642.

Kowalik, Zygmunt, Proshutinsky, Tatiana, and Proshutinsky, Andrey, 2006, Tide–Tsunami Interactions: Science of Tsunami Hazards, v. 24, no. 4, p. 242–256.

Kulikov, E.A., Rabinovich, A.B., Fine, I.V., Bornhold, B.D., and Thomson, R.E., 1998, Tsunami generation by landslides at the Pacific coast of North America and the role of tides: Oceanology, v. 38, no. 3, p. 323–328.

Lander, J.F., 1996, Tsunamis affecting Alaska, 1737–1996: Boulder, CO, NOAA National Geophysical Data Center (NGDC), Key to Geophysical Research Documentation, v. 31, 195 p.

Lee, Homa, Ryan, Holly, Kayen, R.E., Haeussler, P.J., Dartnell, Peter, and Hampton, M.A., 2006, Varieties of submarine failure morphologies of seismically-induced landslides in Alaskan fjords: Norwegian Journal of Geology (Norsk Geologisk Tidsskrift), v. 86, no. 3, p. 221–230.

Leica Geosystems AG, 2002, GPS User Manual, Version 4, Leica Geosystems AG, Heerbrugg, Switzerland, 62 p.

Lemke, R.W., 1967, Effects of the earthquake of March 27, 1964, at Seward, Alaska: U.S. Geological Survey Professional Paper 542-E, 43 p., 2 sheets, scale 1:63,360.

López-Venegas, A.M., Horrillo, Juan, Pampell-Manis, Alyssa, Huérfano, Victor, and Mercado, Aurelio, 2014, Advanced tsunami numerical simulations of the Puerto Rico October 11, 1918, Mona Passage tsunami: Pure and Applied Geophysics, v. 172, no. 6, p. 1,679–1,698. http://doi.org/10.1007/s00024-014-0988-3

Love, M.R., Eakins, B.W., Taylor, L.A., Carignan, K.S., Friday, D., and Grothe, P.R., 2012, Digital Elevation Model of Port Alexander, Alaska: Procedures, Data Sources and Analysis, NOAA Technical Memorandum NESDIS NGDC-63, U.S. Dept. of Commerce, Boulder, CO, 35 p.

Løvholt Finn, Pedersen, G., Harbitz, C.B., Glimsdal, S., and Kim, J., 2015, On the characteristics of landslide tsunamis: Philosophical Transactions of the Royal Society A, v. 373, no. 2053. http://doi.org/10.1098/rsta.2014.0376

Løvholt, Finn, Pedersen, G., Gisler, G., 2008, Oceanic propagation of a potential tsunami from the La Palma Island: Journal of Geophysical Research, v. 113, no. C9., p. 2,156–2,202. http://doi.org/10.1029/2007JC004603

Lynett, Patrick, and Liu, P.L-F., 2002, A numerical study of submarine landslide generated waves and run-up: Proceedings of the Royal Society A, v. 458, no. 2028, p. 2,885–2,910. http://doi.org/10.1098/rspa.2002.0973

Ma, Gangfeng, Kirby, J.T., and Shi, Fengyan, 2013, Numerical simulation of tsunami waves generated by deformable submarine landslides: Ocean Modelling, v. 69, p.146–165. http://doi.org/10.1016/j.ocemod.2013.07.001

Ma, Gangfeng, Shi, Fengyan, and Kirby, J.T., 2012, Shock-capturing non-hydrostatic model for fully dispersive surface wave processes: Ocean Modelling, v. 43–44, p. 22–35. http://doi.org/10.1016/j.ocemod.2011.12.002

Macpherson, A.E., Nicolsky, D.J., and Suleimani, E.N., 2014, Digital elevation models of Skagway and Haines, Alaska: Procedures, data sources, and quality assessment: Alaska Division of Geological & Geophysical Surveys Miscellaneous Publication 155, 15 p. http://doi.org/10.14509/29143

Miller, D.J., 1960, The Alaska earthquake of July 10, 1958: Giant wave in Lituya Bay: Bulletin of the Seismological Society of America, v. 50, no. 2, p. 253–266.

Najafi-Jilani, A., Ataie-Ashtiani, B., 2008, Estimation of near-field characteristics of tsunami generation by submarine landslide: Ocean Engineering, v. 35, no. 5–6, p.545–557. http://doi.org/10.1016/j.oceaneng.2007.11.006

National Centers for Environmental Information (NCEI), 2006, 2-minute gridded global relief data (ETOPO2v2): National Oceanic and Atmospheric Administration (NOAA) digital data set. https://www.ngdc.noaa.gov/mgg/global/etopo2.html

National Geophysical Data Center / World Data Service (NGDC/WDS), in progress, Global Historical Tsunami Database: National Geophysical Data Center, NOAA. http://doi.org/10.7289/V5PN93H7

National Oceanic and Atmospheric Administration (NOAA), National Center for Environmental Information (NCEI), Bathymetry and Global Relief: World Data Service for Geophysics. https://www.ngdc.noaa.gov/mgg/bathymetry/relief.html

National Oceanic and Atmospheric Administration/National Ocean Service (NOAA/NOS), in progress, Observed water levels at 9452210, Juneau AK (interactive web page): NOAA/NOS Tides and Currents, Water Levels.

National Tsunami Hazard Mitigation Program (NTHMP), 2010, Guidelines and best practices for tsunami inundation modeling for evacuation planning: NTHMP Mapping & Modeling Subcommittee, NOAA.

———2012, Proceedings and results of the 2011 NTHMP model benchmarking workshop: Boulder, U.S. Department of Commerce/NOAA/NTHMP, NOAA Special Report, 436 p. http://nthmp.tsunami.gov

Nicolsky, D.J., 2012, Alaska tsunami model, in Proceedings and results of the 2011 NTHMP model benchmarking workshop: Boulder, U.S. Department of Commerce/NOAA/NTHMP, NOAA Special Report, p. 55–87. http://nthmp.tsunami.gov

Nicolsky, D.J., Suleimani, E.N., Combellick, R.A., and Hansen, R.A., 2011, Tsunami inundation maps of Whittier and western Passage Canal, Alaska: Alaska Division of Geological & Geophysical Surveys Report of Investigation 2011-7, 65 p., 4 sheets. http://doi.org/10.14509/23244

Nicolsky, D.J., Suleimani, E.N., Freymueller, J.T., and Koehler, R.D., 2015, Tsunami inundation maps of Fox Islands communities, including Dutch Harbor and Akutan, Alaska: Alaska Division of Geological & Geophysical Surveys Report of Investigation 2015-5, 67 p., 2 sheets, scale 1:12,500. http://doi.org/10.14509/29414

Nicolsky D.J., Suleimani, E.N., Haeussler, P.J., Ryan, H.F., Combellick, R.A., Koehler, R.D., and Hansen, R.A., 2013, Tsunami inundation maps of Port Valdez, Alaska: Alaska Division of Geological & Geophysical Surveys Report of Investigations 2013-1, 79 p., 1 sheet, scale 1:12,500. http://doi.org/10.14509/25055

Nicolsky, D.J., Suleimani, E.N., and Hansen, R.A., 2011, Validation and verification of a numerical model for tsunami propagation and run-up: Pure and Applied Geophysics, v. 168, p. 1,199–1,222. https://doi.org/10.1007/s00024-010-0231-9

Nicolsky, D.J., Suleimani, E.N., and Koehler, R.D., 2014a, Tsunami inundation maps of the villages of Chenega Bay and northern Sawmill Bay, Alaska: Alaska Division of Geological & Geophysical Surveys Report of Investigation 2014-3, 50 p., 7 sheets. http://doi.org/10.14509/29126

———2014b, Tsunami inundation maps of Cordova and Tatitlek, Alaska: Alaska Division of Geological & Geophysical Surveys Report of Investigation 2014-1, 49 p., 2 sheets. http://doi.org/10.14509/27241

Nicolsky, D.J., Suleimani, E.N., and Koehler, R.D., 2016, Tsunami inundation map for the village of Nikolski, Alaska: Alaska Division of Geological & Geophysical Surveys Report of Investigation 2016-7, 34 p., 1 sheet, scale 1:12,500. http://doi.org/10.14509/29674

Nishenko, S.P., and Jacob, K.H., 1990, Seismic potential of the Queen Charlotte–Alaska–Aleutian seismic zone: Journal of Geophysical Research, v. 95, no. B3, p. 2,511–2,532. http://doi.org/10.1029/JB095iB03p02511

Okada, Yoshimitsu, 1985, Surface deformation due to shear and tensile faults in a half-space: Bulletin of the Seismological Society of America, v. 75, no. 4, p. 1,135–1,154.

Page, R.A., 1973, The Sitka, Alaska earthquake of 1972: U.S. Geological SurveyEarthquake Information Bulletin, v. 5, no. 5, p. 4–9.

Plafker, George, Kachadoorian, Reuben, Eckel, E.B., and Mayo, L.R., 1969, Effects of the earthquake of March 27, 1964, on various communities: U.S. Geological Survey Professional Paper 542-G, 50 p. https://pubs.usgs.gov/pp/0542/

Rabinovich, A.B., Thomson, R.E., Bornhold, B.D., Fine, I.V., and Kulikov, E.A., 2003, Numerical modeling of tsunamis generated by hypothetical landslides in the Strait of Georgia, British Columbia: Pure and Applied Geophysics, v. 160, no. 7, p. 1,273–1,313. http://doi.org/10.1007/s000240300006

Rabinovich, A. B., Thomson, R. E., Kulikov, E. A., Bornhold, B. D., and Fine, I. V., 1999, The landslide-generated tsunami of November 3, 1994 in Skagway Harbor, Alaska: A case study: Geophysical Research Letters, v. 26, no. 19, p. 3009–3012. http://doi.org/10.1029/1999GL002334

Ross, S.L., Jones, L.M., Miller, Kevin, Porter, K.A., Wein, A., Wilson, R.I., Bahng, B., Barberopoulou, A., Borrero, J.C., Brosnan, D.M., Bwarie, J.T., Geist, E.L., Johnson, L.A., Kirby, S.H., Knight, W.R., Long, K., Lynett, P., Mortensen, C.E., Nicolsky, D.J., Perry, S.C., Plumlee, G.S., Real, C.R., Ryan, K., Suleimani, E.N., Thio, H.K., Titov, V.V., Whitmore, P.M. and Wood, N.J., 2013, SAFRR (Science Application for Risk Reduction) Tsunami Scenario—Chapter A, Executive Summary and Introduction, *in* Ross, S.L., and Jones, L.M., eds., The SAFRR Tsunami Scenario: U.S. Geological Survey Open-File Report 2013–1170, p. 1–17. http://pubs.usgs.gov/of/2013/1170/

Rozell, Ned, 2016, The giant wave of Icy Bay: University of Alaska Fairbanks Alaska Science Forum, no. 2303. http://http://www.gi.alaska.edu/alaska-science-forum/giant-wave-icy-bay

Ryan, Holly, von Huene, Roland, Scholl, Dave, and Kirby, Steve, 2012, Tsunami hazards to US coasts from giant earthquakes in Alaska: Eos Transactions, American Geophysical Union, v. 93, no. 19, 185 p. http://doi.org/10.1029/2012EO190001

Schwab, W.C., Lee, H.J., and Twichell, D.C., eds., 1993, Submarine landslides; Selected studies in the U.S. Exclusive Economic Zone: U.S. Geological Survey Bulletin 2002, 204 p. https://pubs.er.usgs.gov/publication/b2002

Shannon, W.L., and Hilts, D.E., 1973, Earthquake-caused submarine landslide at Seward, Alaska, *in* The Great Alaska Earthquake of 1964: National Academy of Sciences, Engineering, Publication 1606, p. 144-156.

Shao, Guangfu, Li, Xiangyu, Ji, Chen, and Maeda, Takahiro, 2011, Focal mechanism and slip history of 2011 M_w 9.1 off the Pacific coast of Tohoku earthquake, constrained with teleseismic body and surface waves: Earth, Planets and Space, v. 63, no. 7, p. 559–564. http://doi.org/10.5047/eps.2011.06.028

Shennan, Ian, Barlow, Natasha, and Combellick, R.A., 2008, Paleoseismological records of multiple great earthquakes in southcentral Alaska—A 4,000-year record at Girdwood, *in* Freymueller, J.T., Haeussler, P.J., Wesson, R.L, and Ekström, Goran, eds., Active Tectonics and Seismic Potential of Alaska: American Geophysical Union Geophysical Monograph 179, p. 185–199.

Shennan, Ian, Bruhn, Ronald, and Plafker, George, 2009, Multi-segment earthquakes and tsunami potential of the Aleutian megathrust: Quaternary Science Reviews, v. 28, no. 1–2, p. 7–13.

Shi, Fengyan, Kirby, J.T., Harris, J.C., Geiman, J.D., and Grilli, S.T., 2012, A high-order adaptive time-stepping TVD solver for Boussinesq modeling of breaking waves and coastal inundation: Ocean Modelling, v. 43-44, p. 36–51. http://doi.org/10.1016/j.ocemod.2011.12.004

Skvortsov, A., and Bornhold, B., 2007, Numerical simulation of the landslide-generated tsunami in Kitimat Arm, British Columbia, Canada, 27 April 1975: Journal of Geophysical Research, v. 112, no. F2. http://doi.org/10.1029/2006JF000499

Suito, Hisashi, and Freymueller, J.T., 2009, A viscoelastic and afterslip postseismic deformation model for the 1964 Alaska earthquake: Journal of Geophysical Research, v. 114, no. B11, p. 404–426. http://doi.org/10.1029/2008JB005954

Suleimani, E.N., 2011, Numerical studies of tectonic and landslide-generated tsunamis caused by the 1964 Great Alaska Earthquake: Fairbanks, Alaska, University of Alaska Fairbanks, Ph.D. dissertation, 181 p.

Suleimani, E.N., Nicolsky, D.J., and Koehler, R.D., 2013, Tsunami inundation maps of Sitka, Alaska: Alaska Division of Geological & Geophysical Surveys Report of Investigation 2013-3, 76 p., 1 sheet, scale 1:12,500. http://doi.org/10.14509/26671

Suleimani, E.N., Nicolsky, D.J., and Koehler, R.D., 2015, Tsunami inundation maps of Elfin Cove, Gustavus, and Hoonah, Alaska: Alaska Division of Geological & Geophysical Surveys Report of Investigation 2015-1, 79 p., 3 sheets. http://doi.org/10.14509/29404

Suleimani, E.N., Nicolsky, D.J., and Koehler, R.D., 2016, Tsunami inundation maps for Yakutat, Alaska: Alaska Division of Geological & Geophysical Surveys Report of Investigation 2016-2, 47 p., 1 sheet, scale 1:10,000. http://doi.org/10.14509/29577

Suleimani, E.N., Nicolsky, D.J., West, D.A., Combellick, R.A., and Hansen, R.A., 2010, Tsunami inundation maps of Seward and northern Resurrection Bay, Alaska: Alaska Division of Geological & Geophysical Surveys Report of Investigation 2010-1, 47 p., 3 sheets, scale 1:12,500. http://doi.org/10.14509/21001

Swanston, D.N., 1972, A report on the mass wasting (landslide) hazards in the urban and urbanizing areas of the City and Borough of Juneau, Alaska, in Geophysical Hazard Investigation for the City and Borough of Juneau, Alaska, Technical Supplement, Appendix II, p. 18-41. http://www.juneau.org/cddftp/avalanche/GHI-Tech_Appendix_2.PDF

Sykes, L.R., 1971, Aftershock zones of great earthquakes, seismicity gaps, and earthquake prediction for Alaska and the Aleutians: Journal of Geophysical Research, v. 75, p. 8,021–8,041.

Synolakis, C.E., Bernard, E.N., Titov, V.V., Kânoğlu, U., and González, F.I., 2007, Standards, criteria, and procedures for NOAA evaluation of tsunami numerical models: Seattle, Washington, NOAA/Pacific Marine Environmental Laboratory, Technical Memorandum OAR PMEL-135, 55 p.

Tang, Liujuan, Titov, V.V., Bernard, E.N., Wei, Yong, Chamberlin, C.D., Newman, J.C., Mofjeld, H.O., Arcas, Diego, Eble, M.C., Moore, Christopher, Uslu, Burak, Pells, Clint, Spillane, Michael, Wright, Lindsey, and Gica, Edison, 2012, Direct energy estimation of the 2011 Japan tsunami using deep-ocean pressure measurements: Journal of Geophysical Research, v. 117, no. C8. http://doi.org/10.1029/2011JC007635

Tappin, D.R., Watts, P., and Grilli, S.T., 2008, The Papua New Guinea tsunami of 1998: Anatomy of a catastrophic event: National Hazards and Earth System Sciences, v. 8, no. 2, p. 243–266. http://doi.org/10.5194/nhess-8-243-2008

Tappin, D.R., Watts, P., McMurtry, G.M., Lafoy, Y., and Matsumoto, T., 2001, The Sissano, Papua New Guinea tsunami of July 1998-offshore evidence on the source mechanism: Marine Geology, v. 175, no. 1–4, p. 1–23. http://doi.org/10.1016/S0025-3227(01)00131-1

Tehranirad, Babak, Kirby, J.T., Ma, Gangfeng. and Shi, Fengyan, 2012, Tsunami benchmark results for non-hydrostatic wave model NHWAVE, Version 1.1: Newark, NJ, University of Delaware Center for Applied Coastal Research, Research Report No. CACR-12-03, 43 p.

Tocher, D., 1960, The Alaska earthquake of July 10, 1958: Movement on the Fairweather fault and field investigation of southern epicentral region: Bulletin of the Seismological Society of America, v. 50, no. 2, p. 267–292.

Watada, S., Kusumoto, S., and Satake, K., 2014, Traveltime delay and initial phase reversal of distant tsunamis coupled with the self-gravitating elastic Earth: Journal of Geophysical Research: Solid Earth, v. 119, no. 5, p. 4287–4310. http://doi.org/10.1002/2013JB010841

Watts, P., Grilli, S.T., Kirby, J.T., Fryer, G.J., and Tappin, D.R., 2003, Landslide tsunami case studies using a Boussinesq model and a fully nonlinear tsunami generation model: Natural Hazards Earth System Sciences v. 3, no. 5, p. 391–402. http://doi.org/10.5194/nhess-3-391-2003

Weiss, Robert, Fritz, H.M., and, Wünnemann, Kai, 2009, Hybrid modeling of the mega-tsunami run-up in Lituya Bay after half a century: Geophysical Research Letters, v. 36, no. 9. http://doi.org/10.1029/2009GL037814

Wieczorek, G.F., Geist, E.L., Motyka, R.J., and Jakob, Matthias, 2007, Hazard assessment of the Tidal Inlet landslide and potential subsequent tsunami, Glacier Bay National Park, Alaska: Landslides, v. 4, no. 3, p. 205–215.

Wilson, B.W., and Tørum, A., 1968, The tsunami of the Alaskan earthquake, 1964—Engineering evaluation: Vicksburg, MI, U.S. Army Corps of Engineers Technical Memorandum No. 25, 401 p.

Yavari-Ramshe, S., and Ataie-Ashtiani, B., 2016, Numerical simulation of subaerial and submarine landslide generated tsunami waves—recent advances and future challenges: Landslides, v. 13, no. 6, p. 1,325–1,368. http://doi.org/10.1007/s10346-016-0734-2

APPENDIX

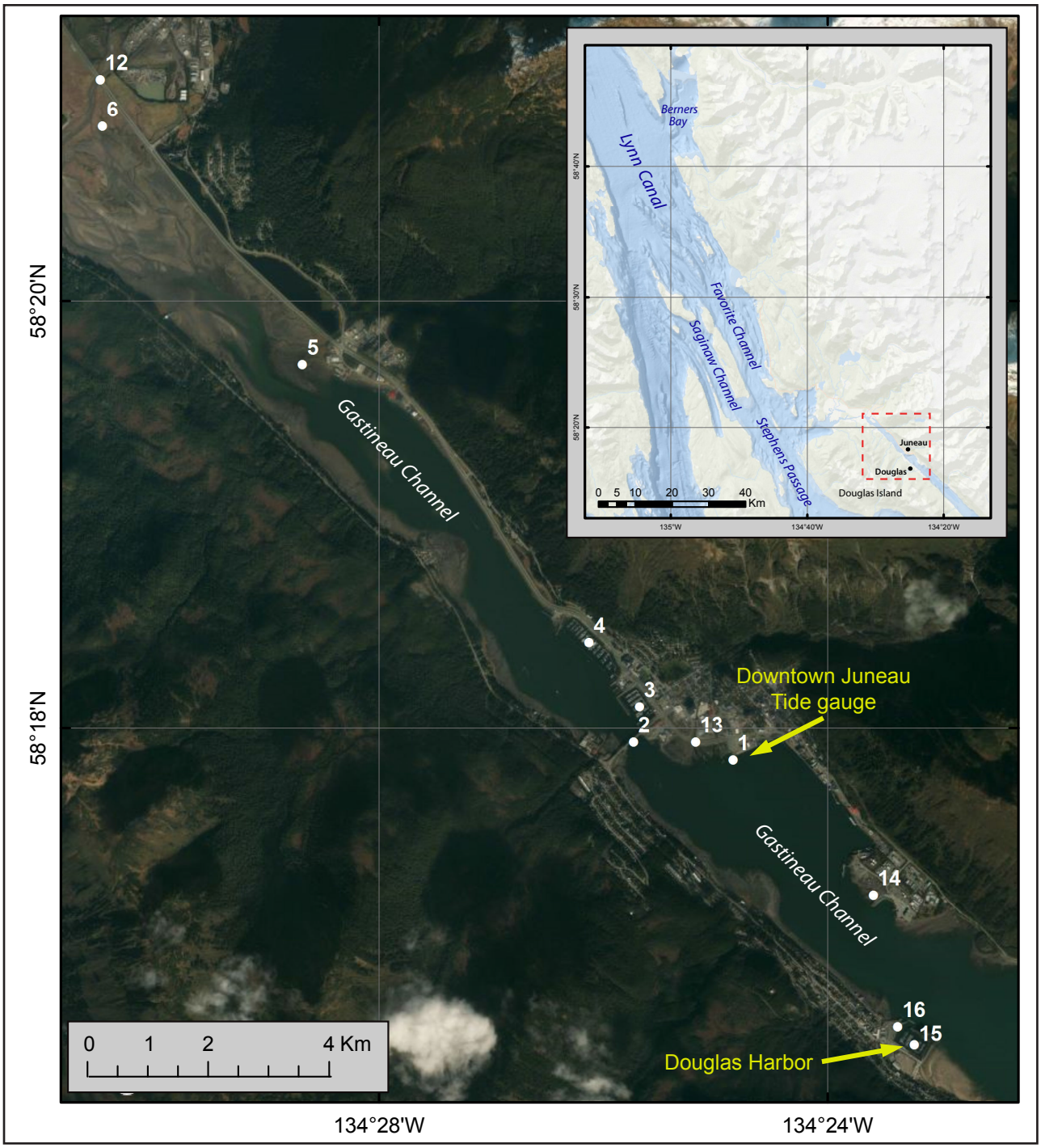

Figure A-1. Locations of time series points near Juneau in Gastineau Channel. The coordinate locations of the time series points are listed in table A-1.

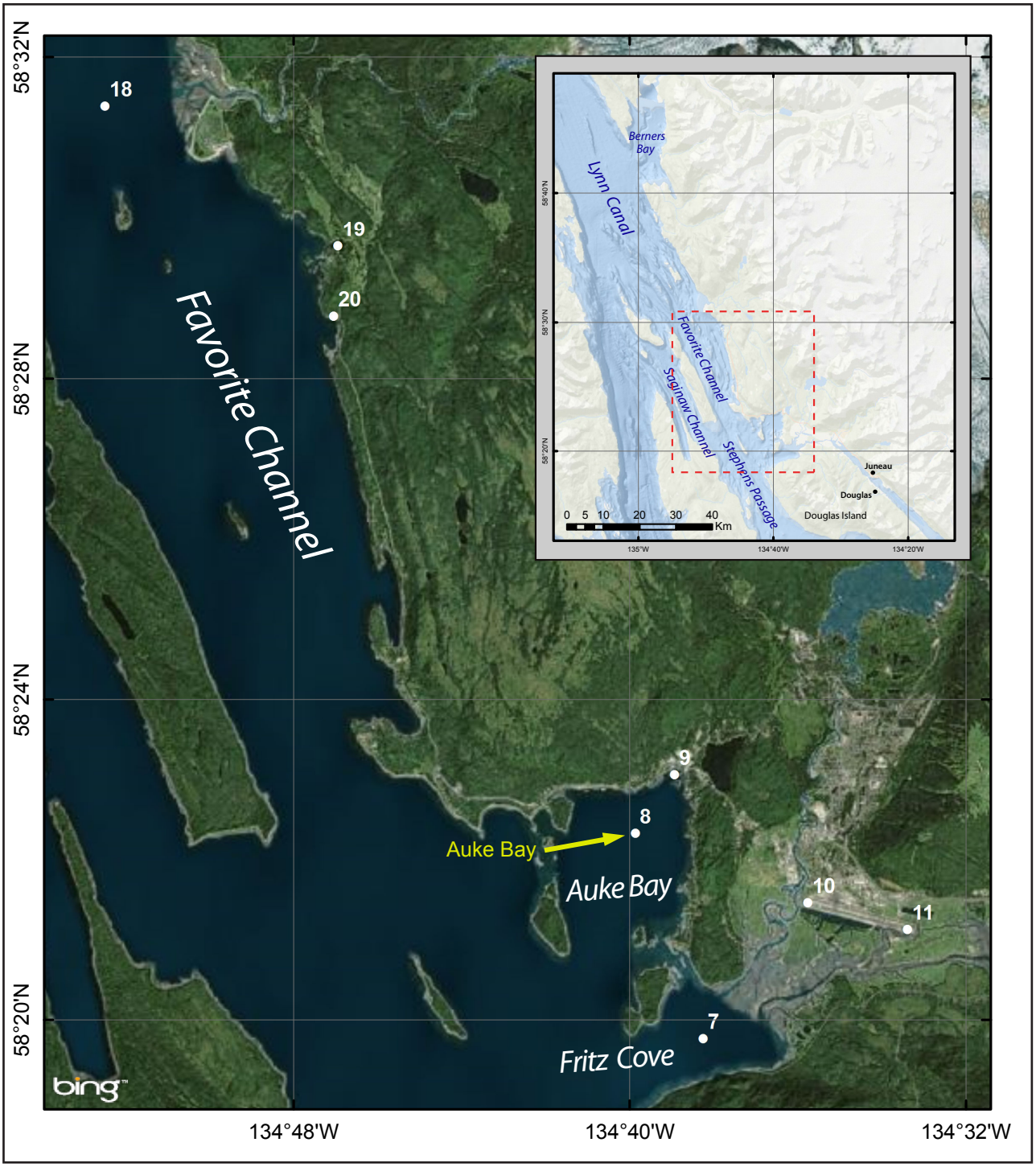

Figure A-1, continued. Locations of time series points near Juneau in Lynn Canal. The coordinate locations of the time series points are listed in table A-1.

Table A-1. Maximum water levels and water velocity at time series points near Juneau. The maximum water depth above ground is provided for pre-earthquake onshore (S) locations, whereas the maximum water level above the pre-earthquake MHHW is provided for offshore (O) locations. The minimum elevation (sixth column) above the post-earthquake MHHW datum is provided for onshore locations, while the minimum post-earthquake depth is provided for offshore locations. Blank cells indicate that the water dynamics for the particular landslide-generated tsunami scenario was not modeled at these locations because of the slide was located far away. The horizontal datum used is World Geodetic System of 1984.

#	Label	S/O	Longitude (°W)	Latitude (°N)	Minimum elevation/ depth (meters)	Maximum water depth above ground/sea level (meters)								Maximum water velocity (meters/second)							
						Tectonic scenario (with doubled slip)		Landslide scenario						Tectonic scenario (with doubled slip)		Landslide scenario					
						1D	4D	8	9	10	11	12	13	1D	4D	8	9	10	11	12	13
1	Juneau tidal gauge	O	134.414167	58.297500	17.6	1.4	2.5				0.3	0.5	1.6	0.3	0.7				0.6	0.3	0.7
2	Bridge	O	134.428889	58.298889	18.7	1.2	2.0				0.3	0.3	1.0	4.5	7.8				0.6	0.4	9.5
3	Harbor	O	134.428056	58.301667	9.1	1.2	2.0				0.5	0.2	1.4	0.3	0.7				0.4	0.2	1.4
4	Aurora Harbor	O	134.435556	58.306667	9.6	1.2	2.1				0.2		1.6	0.3	0.4				0.3		1.0
5	Salmon Creek	O	134.478056	58.328333	3.0	1.1	1.9	0.3			0.1		0.8	2.7	3.2	0.7			0.2		3.5
6	Level Creek	O	134.507778	58.346944	1.2	1.3	2.0	0.7			0.1		0.7	1.1	1.5	0.7			0.3		1.7
7	Fritz Cove	O	134.637500	58.329444	72.5	0.8	1.3	7.4	0.3	0.2			0.2	0.1	0.1	5.1	0.1	0.1			0.1
8	Auke Bay	O	134.664444	58.372222	54.2	0.8	1.3	1.2	0.2	0.1				0.0	0.1	0.8	0.3	0.1			
9	UAS Harbor	O	134.648889	58.384444	30.8	0.8	1.3	2.7	1.2	0.6				0.0	0.0	0.9	0.4	0.1			
10	Airport West	S	134.596111	58.357778	3.8	0.0	0.0	0.2						0.0	0.0	5.9					
11	Airport East	S	134.556667	58.352222	3.5	0.0	0.0	0.0						0.0	0.0	0.0					
12	Eagan Dr. at Lemon Creek	O	134.508056	58.350556	0.9	1.2	1.6	0.5			0.2		0.9	1.3	2.3	2.8			1.4		4.1
13	Eagan Dr. at Gold Creek	S	134.419722	58.298889	0.1	1.3	2.5				0.5	0.6	2.0	0.1	0.3				4.6	0.8	5.8
14	JNU AML Yard	S	134.393333	58.286944	2.6	0.0	0.0				0.0	0.6		0.0	0.0				0.0	1.6	
15	Douglas Harbor	O	134.387222	58.275278	8.2	1.3	2.4				1.1		1.8	0.1	0.1				0.9		0.6
16	Douglas Harbor parking	S	134.389722	58.276667	1.0	0.3	1.4				0.7		2.0	0.3	1.4				3.6		5.6
17	Little Bay	O	134.914444	58.665556	23.9	0.8	1.2		0.0	1.5				0.1	0.1		0.0	0.9			
18	Eagle River Delta	O	134.874444	58.523056	56.5	0.6	1.0	0.3	7.3	0.4				0.1	0.3	0.2	2.8	0.2			
19	Salt Lake	O	134.782222	58.494167	0.5	0.6	1.1		0.9	0.5				0.2	0.4		3.2	1.1			
20	Pearl Harbor beach	S	134.783889	58.479722	3.5	0.0	0.0		1.8					0.0	0.0		13.2				

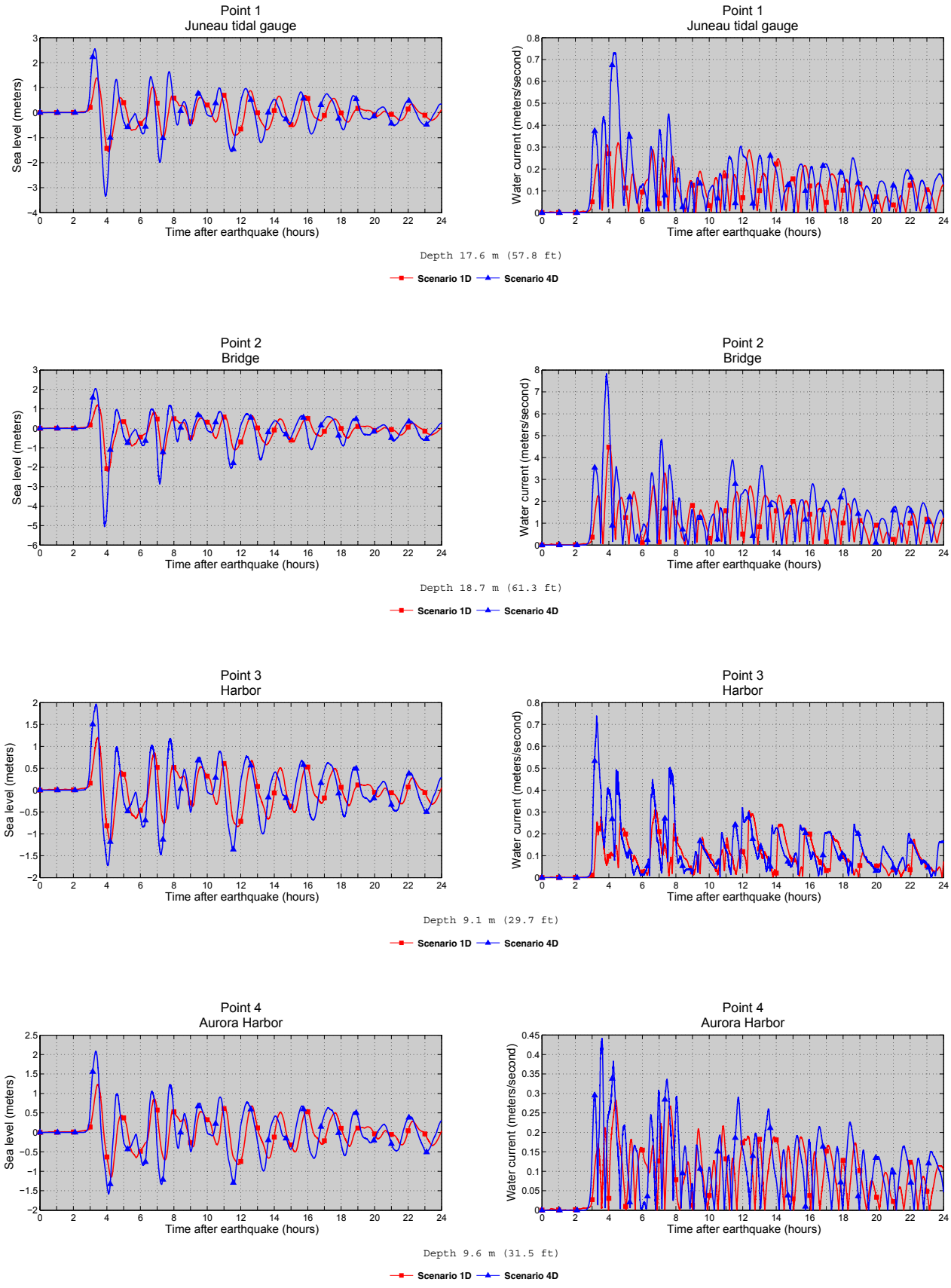

Figure A-2. Time series of the water level (left column) and velocity (right column) for scenarios 1D and 4D (with doubled slip to account for the tsunami-tide interactions) at locations shown in figure A-1.

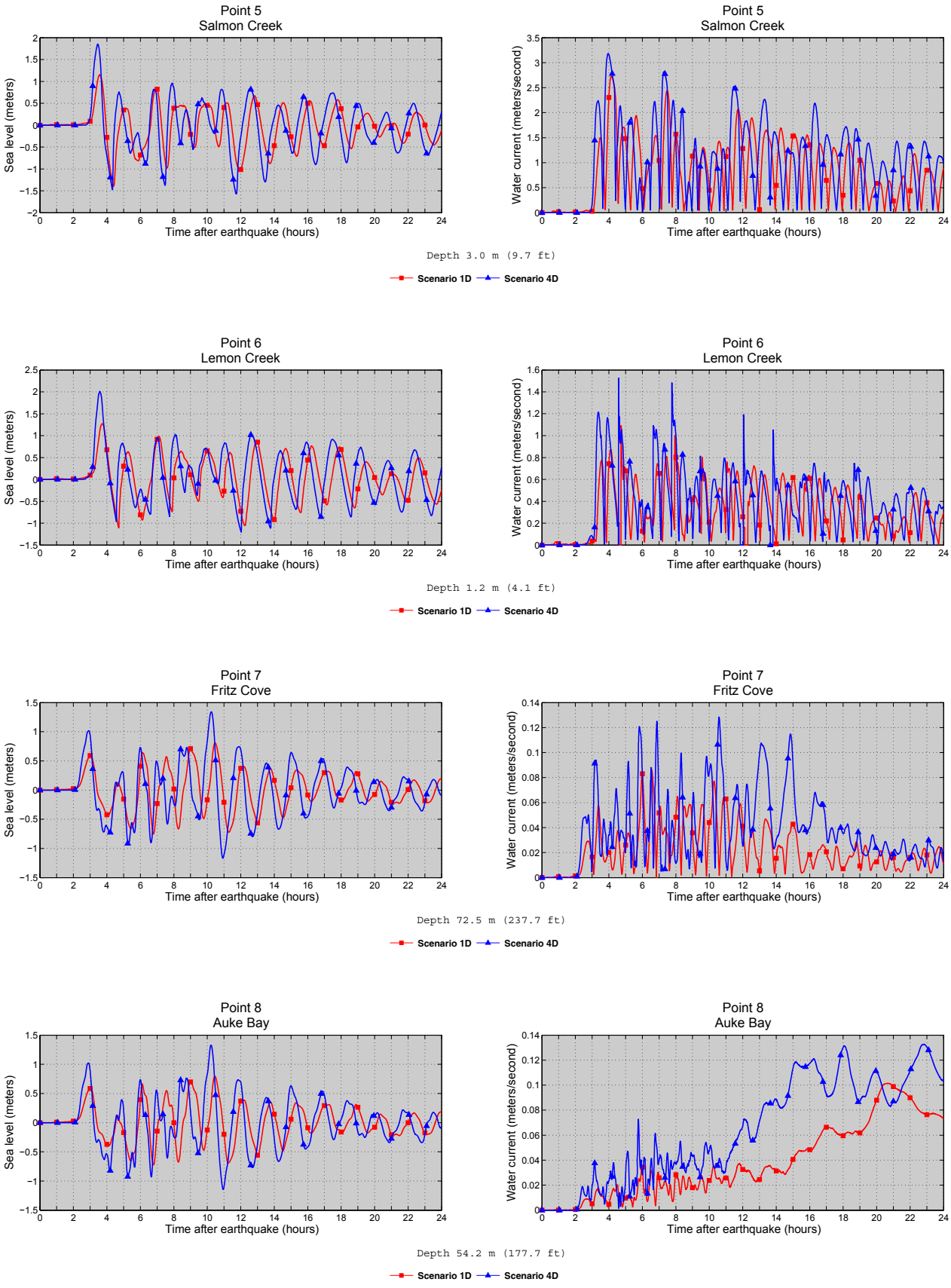

Figure A-2, continued. Time series of the water level (left column) and velocity (right column) for scenarios 1D and 4D (with doubled slip to account for the tsunami-tide interactions) at locations shown in figure A-1.

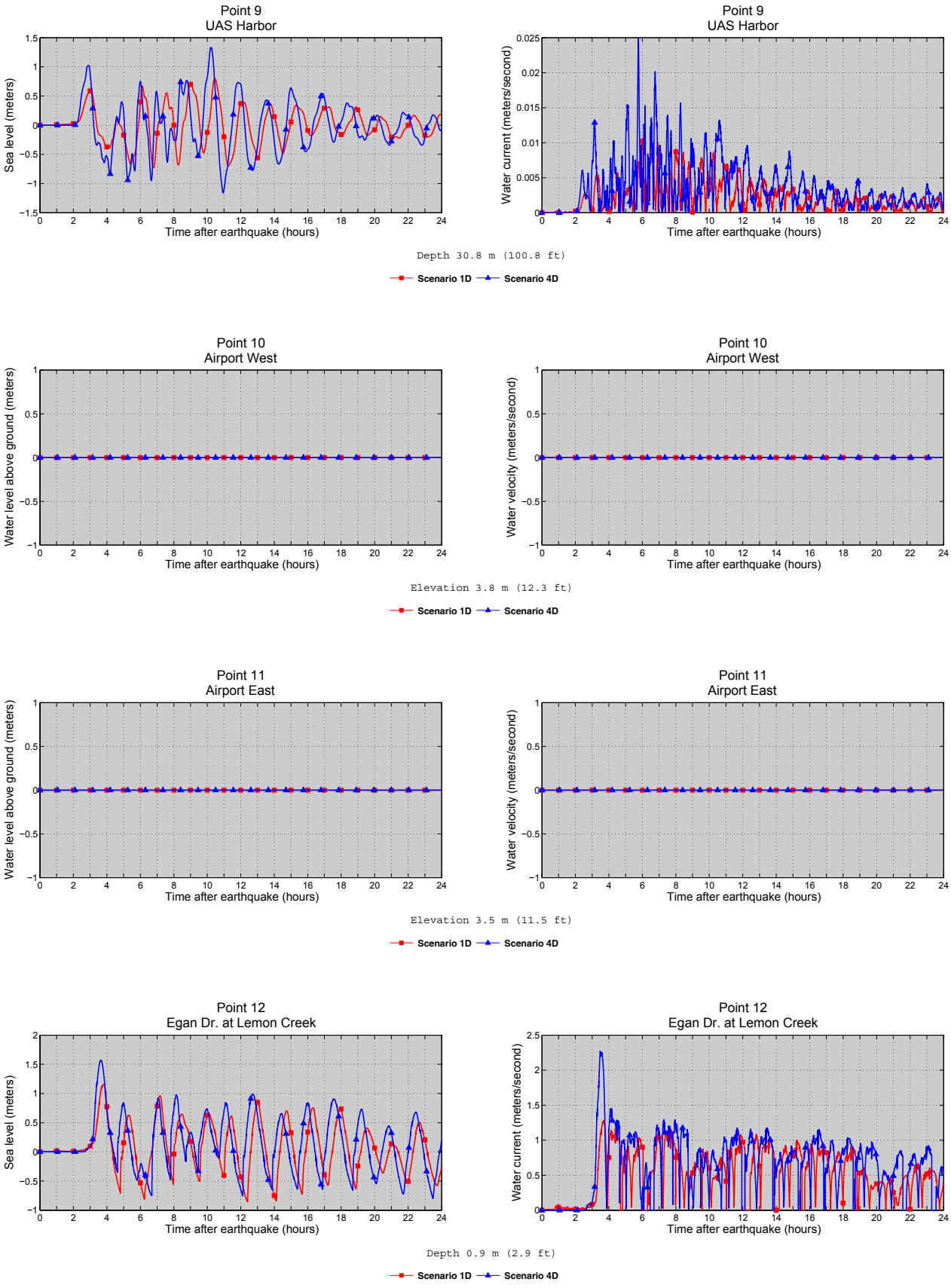

Figure A-2, continued. Time series of the water level (left column) and velocity (right column) for scenarios 1D and 4D (with doubled slip to account for the tsunami-tide interactions) at locations shown in figure A-1.

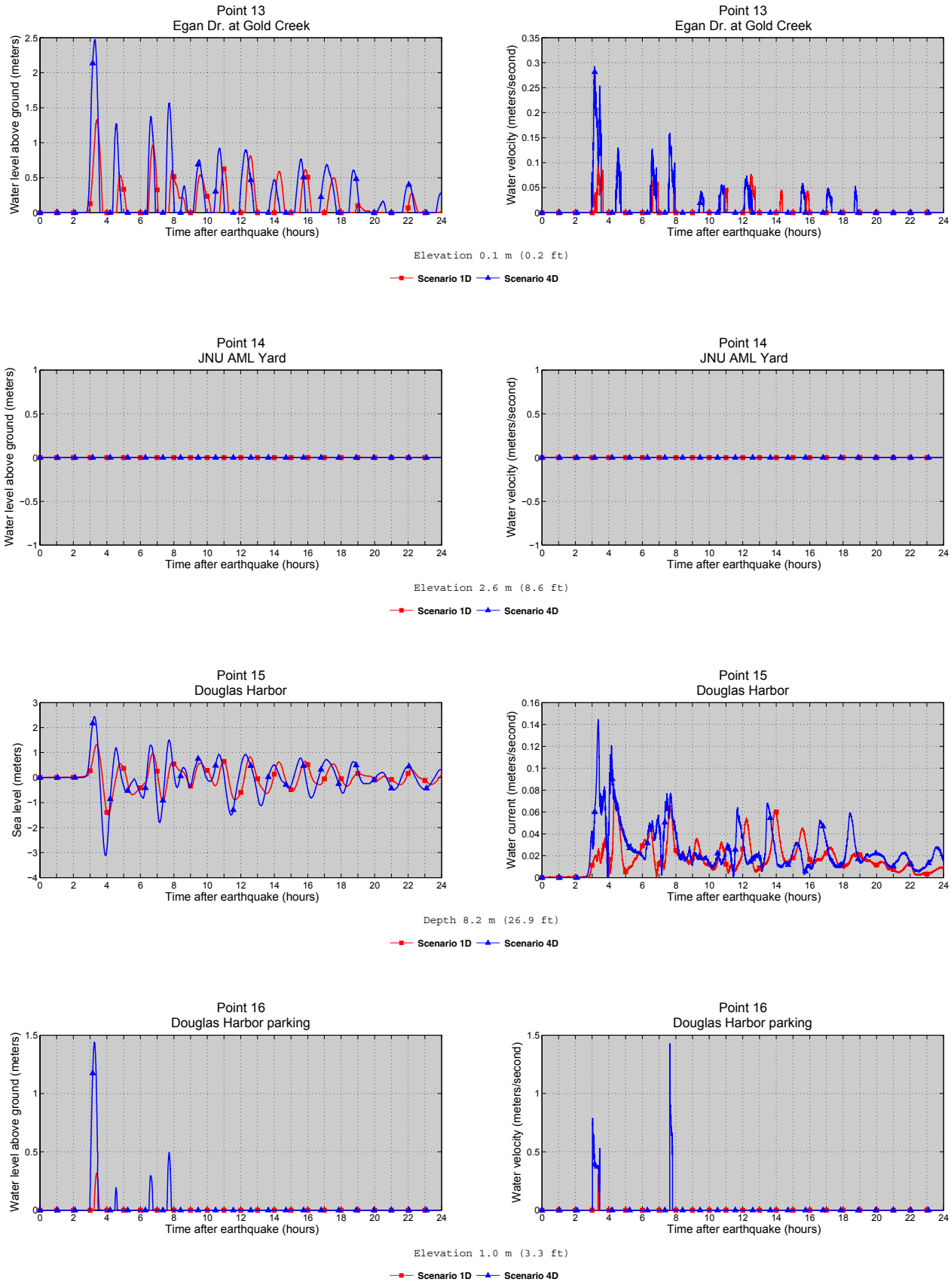

Figure A-2, continued. Time series of the water level (left column) and velocity (right column) for scenarios 1D and 4D (with doubled slip to account for the tsunami-tide interactions) at locations shown in figure A-1.

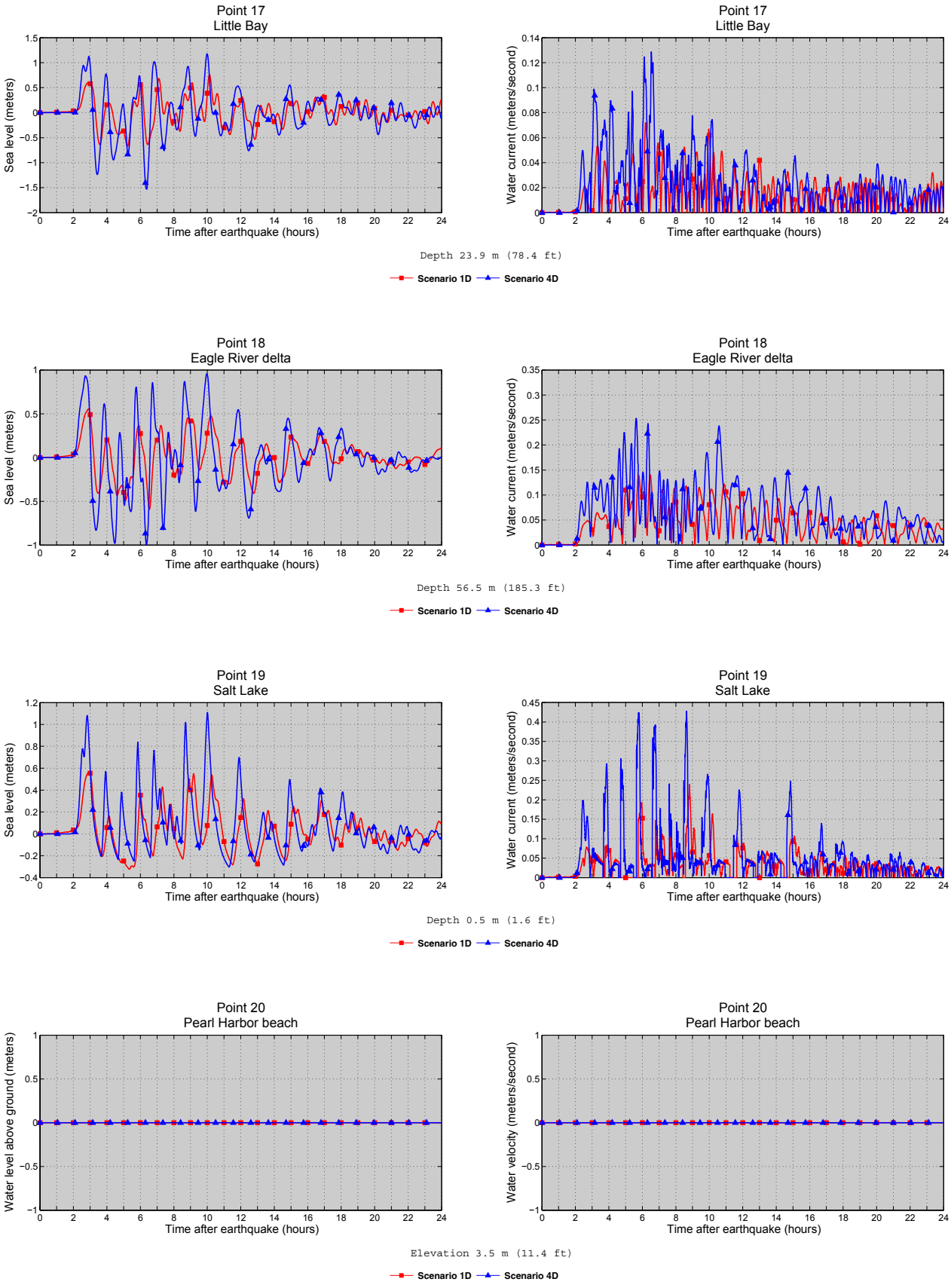

Figure A-2, continued. Time series of the water level (left column) and velocity (right column) for scenarios 1D and 4D (with doubled slip to account for the tsunami-tide interactions) at locations shown in figure A-1.

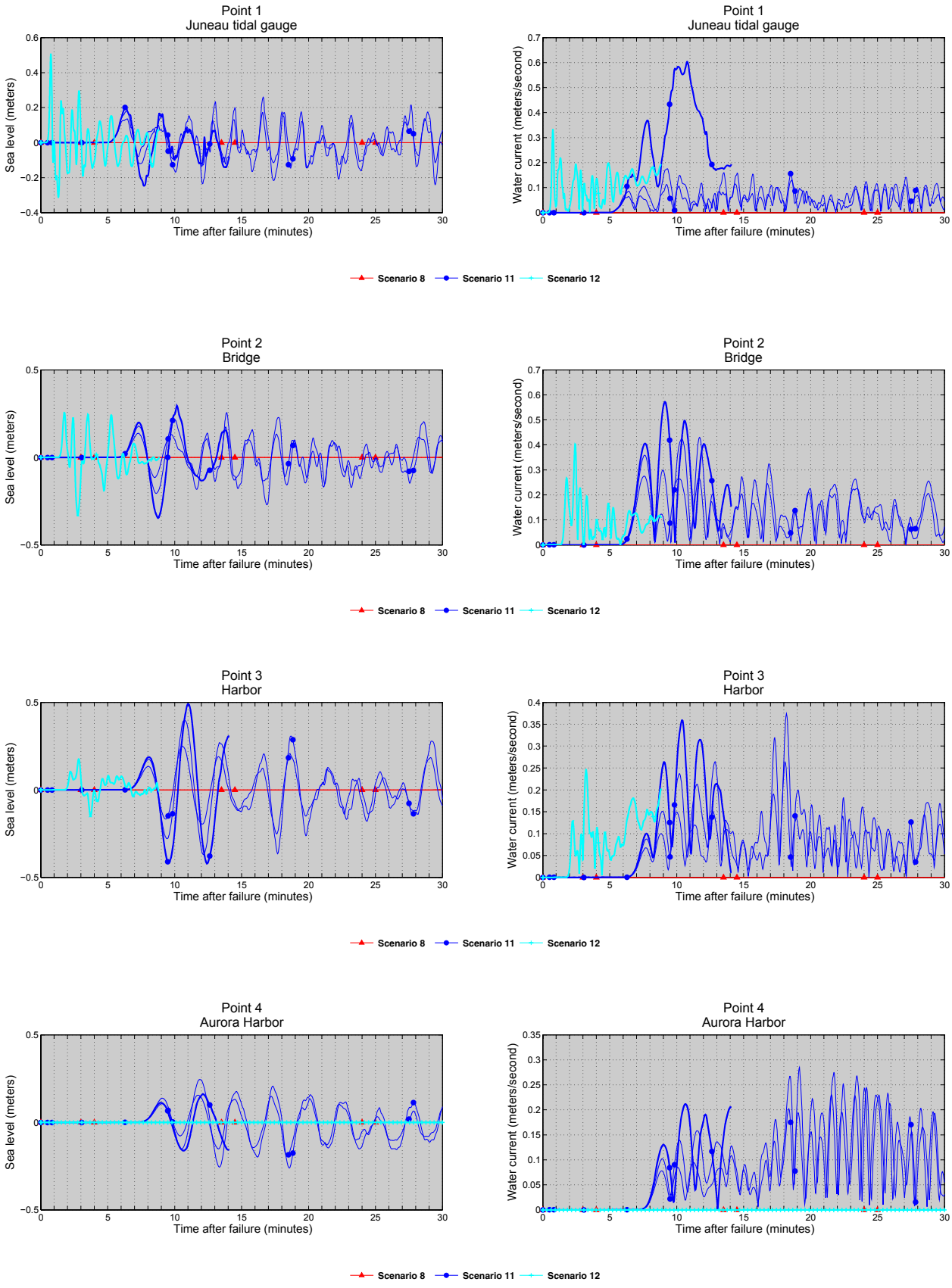

Figure A-3. Time series of the water level (left column) and velocity (right column) for scenarios 8–12 at locations shown in figure A-1.

Figure A-3, continued. Time series of the water level (left column) and velocity (right column) for scenarios 8–12 at locations shown in figure A-1.

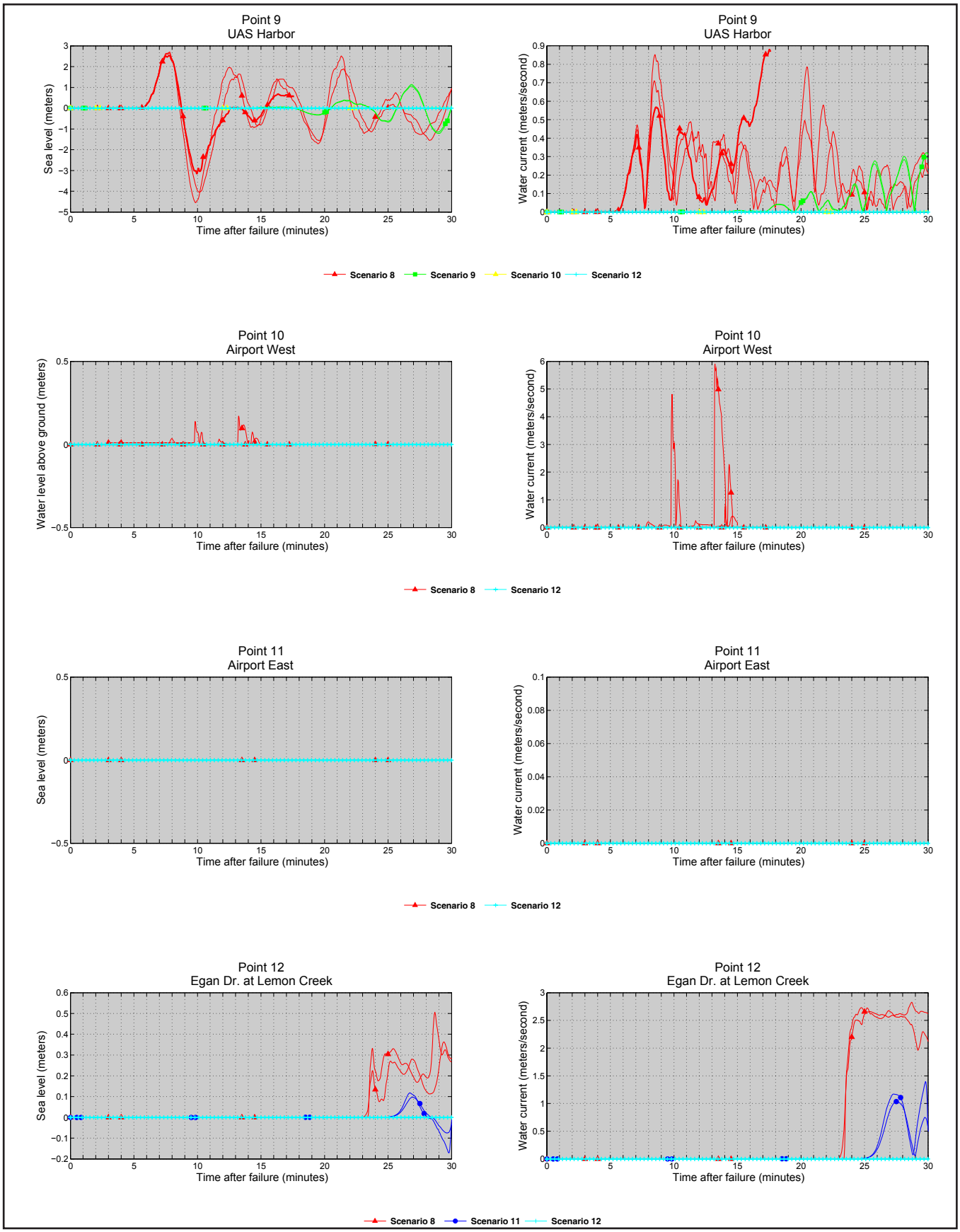

Figure A-3, continued. Time series of the water level (left column) and velocity (right column) for scenarios 8–12 at locations shown in figure A-1.

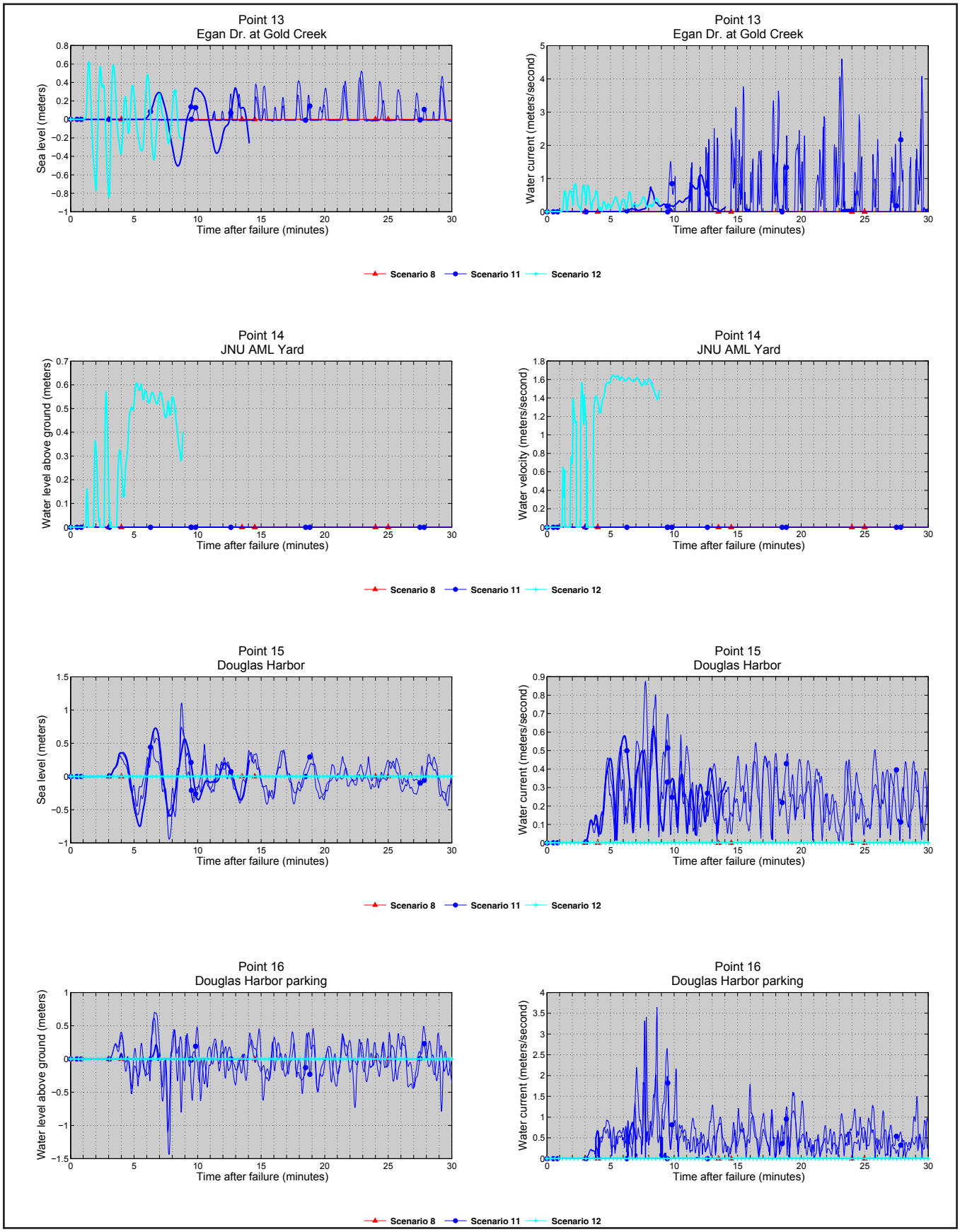

Figure A-3, continued. Time series of the water level (left column) and velocity (right column) for scenarios 8–12 at locations shown in figure A-1.

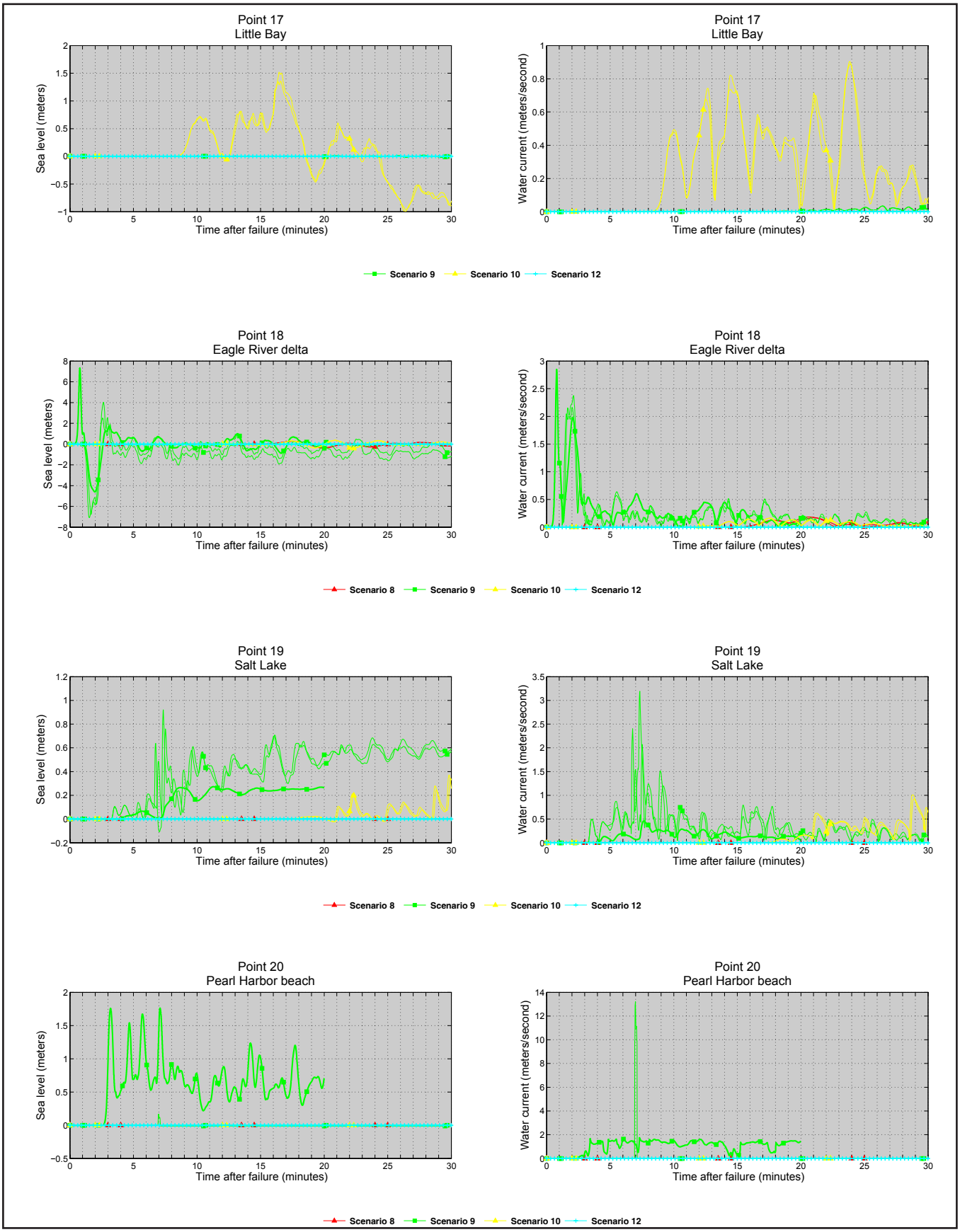

Figure A-3, continued. Time series of the water level (left column) and velocity (right column) for scenarios 8–12 at locations shown in figure A-1.

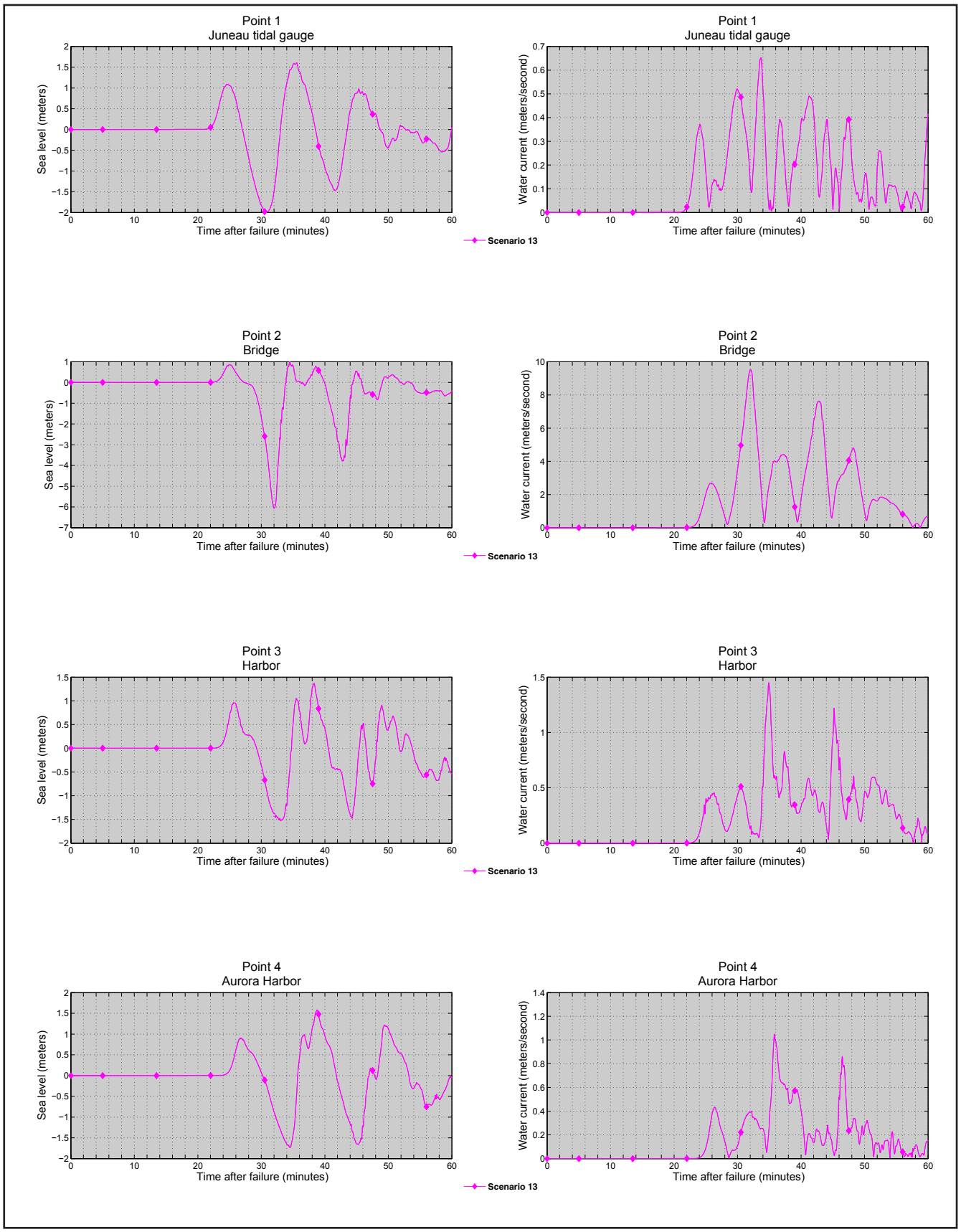

Figure A-4. Time series of the water level (left column) and velocity (right column) for scenario 13 at locations shown in figure A-1.

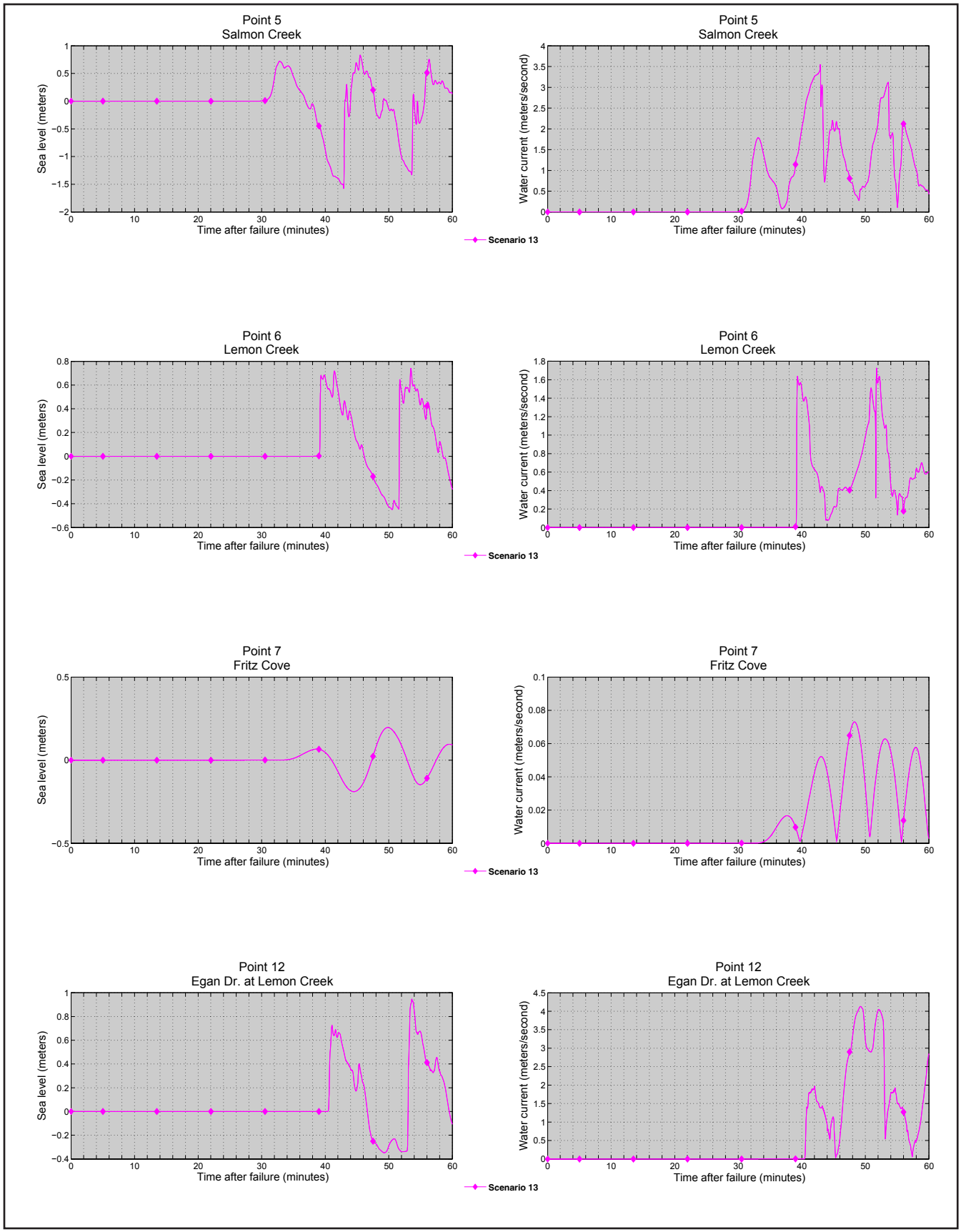

Figure A-4, continued. Time series of the water level (left column) and velocity (right column) for scenario 13 at locations shown in figure A-1.

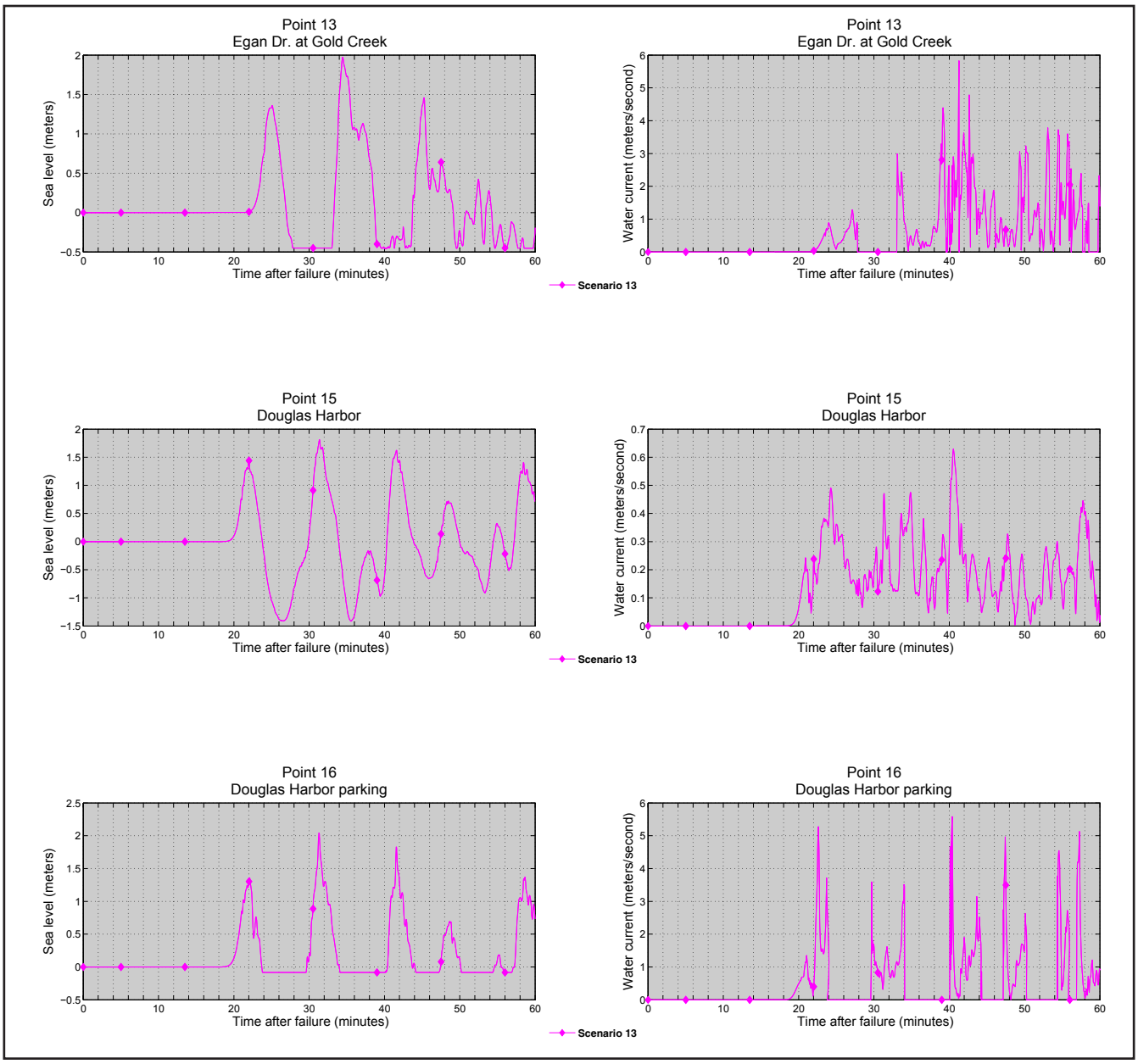

Figure A-4, continued. Time series of the water level (left column) and velocity (right column) for scenario 13 at locations shown in figure A-1.